Active Damping Techniques for the LCL Filter Resonance in the Digitally Controlled Grid-Connected Converters

マハモド, アブデルワハブ ガーファル モハメド

https://doi.org/10.15017/1807052

出版情報：九州大学, 2016, 博士（学術）, 課程博士
バージョン：

Active Damping Techniques for the LCL Filter Resonance in the Digitally Controlled Grid-Connected Converters

2016

Mahmoud Abdelwahab Gaafar Mohamed

Kyushu University, Fukuoka, JAPAN

Active Damping Techniques for the LCL Filter Resonance in the Digitally Controlled Grid-Connected Converters

Presented by

Mahmoud Abdelwahab Gaafar Mohamed

A Thesis submitted to

Department of Electrical and Electronic Engineering

in partial fulfillment of the requirements for the degree of

Doctor of Philosophy

in

Electrical Engineering

Graduate School of Information Science and Electrical Engineering

Kyushu University, Fukuoka, JAPAN

December, 2016

Abstract

Because of their higher attenuation for switching harmonics with lower weight and size, LCL filters are widely used to connect the pulse width modulated converters into the utility grid in order to limit the harmonic contents of the injected grid current to be complied with the grid codes; i.e. IEEE 519-1992. However, the resonance introduced by the LCL filters represents a challenge for control system designers.

For the digitally controlled converters, which have an inherent delay due to computations and sample and hold effect, the stability of single control loop can be maintained only for resonant frequencies higher than one-sixth of the sampling frequency. However, the stability violates if the resonant frequency decreases less than this critical value. Such decreasing in the resonant frequency can occur with the frequent increase in the grid inductance. Damping techniques have to be adopted to cope with this challenge. Compared to passive damping which causes power losses, active damping by modifying the control algorithm is more efficient.

Number of active damping methods have been presented in the literature. Capacitor-current-based active damping method is the simplest method among these methods. However more number of sensors is needed. This, in turn, increase the overall system cost. Moreover, excitation of unstable open loop poles is mandatory for resonant frequencies more than one-sixth of the sampling frequency; this non-minimum phase behavior declines the system robustness. A differentiation of the capacitor voltage can be used to produce the damping effect; however, this method causes noise amplification. To reduce the number of sensors, grid-current-based active damping by using high-pass filter (HPF) can be employed. However, the co-design steps of this HPF along with the fundamental current regulator are very complicated.

In order to overcome the limitations of the existing active damping methods, some novel algorithms and analysis are proposed. The thesis consists of five chapters. These chapters can be summarized as follows:

In chapter one, a theoretical background about LCL filters, resonance problem and digitally controlled grid-connected converters are introduced. A literature review about the existing damping techniques along with their limitations are presented as well.

In chapter two, an observer in the control system is employed to estimate the capacitor current without the need for additional sensors. A systematic design of the observer loop is presented. The control algorithm is implemented in stationary reference frame to reduce the overall computation burden on control hardware. The results show that the observer-based system offers a good damping behavior without the need for additional sensors. This, in turn, reduces the overall cost.

In chapter three, a novel active damping method using two feedback loops of the capacitor voltage and the grid current is proposed. The proposed method is derived in the continuous time domain with a discussion for its discrete implementation. To show the superiority of the proposed method, a comparative study is presented. Compared to capacitor-current-based method, the cost is reduced by omitting the high cost current sensor. Moreover, the non-minimum phase behavior is avoided over wide range of resonant frequencies. Compared to capacitor-voltage-based method, the proposed method behaves effectively over wide range of resonant frequencies without stability violation or the need to a differentiator which amplifies the noise. Compared to grid-current-based method, straightforward co-design steps for the active damping loops along with the fundamental current regulator are proposed. The superiority of the proposed method is verified over wide range of resonant frequencies.

In chapter four, active damping using high-pass filter (HPF) of the grid current is investigated. A detailed study for the actively damped filter in discrete time domain is introduced. Limits for the HPF parameters are derived in order to avoid the non-minimum phase behavior. Based on this investigation, the performance of this method is highly improved where the ability to avoid the non-minimum phase behavior is extended up to resonant frequencies about 0.39 of the sampling frequency. In addition, straightforward co-design steps for the HPF along with the fundamental current regulator are proposed. Numerical example and experimental work are carried out to confirm the obtained results.

In chapter five, the last chapter in the thesis, both the final summary and the conclusion outlines for the thesis are introduced. The expected future work is introduced as well.

Acknowledgment

All thanks are due to **ALLAH**, who facilitates the reasons for me to achieve this work.

I would like to express my sincere gratitude to my academic advisor **Prof. Masahito Shoyama**. His kind guidance through comments and constant support have made it possible for me to make my thesis complete.

I am very grateful for the excellent working atmosphere in the green electronics laboratory. Special thanks to **Dr. Gamal Dousoky**, **Dr. Emad M. Ahmed, Dr. Husam Ramadan, Dr. Imaoka**, **Mr. Kawano**, and **Mr. Hashimoto.** Also, I would like to thank my friends in the laboratory. Special thanks to **Mr. Mokhtar** and **Mr. Donny** for being good friends, helping out in the laboratory and engaging in numerous technical discussions.

I would like to express my deep appreciation to my beloved country (**Egypt**) for supporting me during my graduate study at Kyushu University.

During their life and even after they passed away, my beloved **Parents** were my constant source of inspiration in my life. May **ALLAH** grant them as the reward of this work.

I would like to show my great appreciation to my brothers, my sisters, and all my friends for their encouragement, prayers, and support. Special thanks to my lovely wife for her support, patience, and care of our kids (**Habiba** and **Mariem**), that enabled me to concentrate on my research work.

Mahmoud Abdelwahab Gaafar

December 2016

Table of Contents

Chapter 1:

Introduction

The penetration of renewable energy sources (wind and PV power plants) into the grid system worldwide is increasing exponentially [1]. A typical structure of such grid-connected systems is shown in Fig. 1.1 where a power converter is used to transfer the harvested energy from the renewable energy sources into the utility grid.

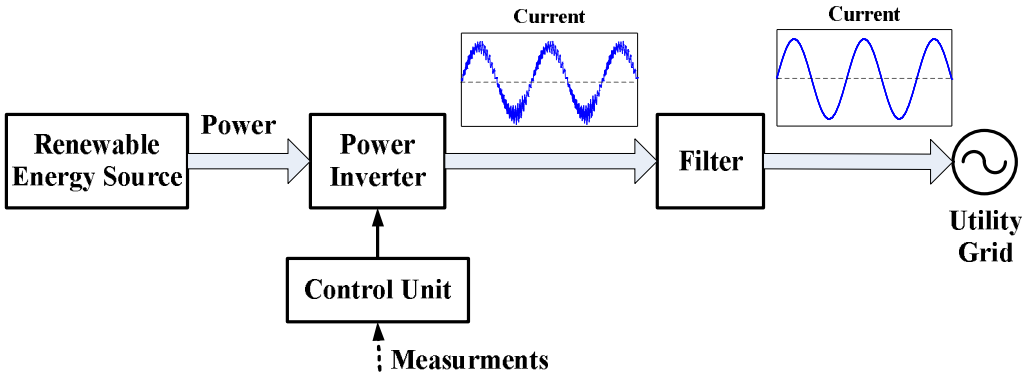

Fig. 1.1 Typical structure of grid-connected renewable energy source

In addition to transfer the generated DC power to the AC grid, the power converters should be carefully controlled to exhibit advanced and sophisticated functions such as dynamic control of active and reactive power, voltage ride-through, reactive current injection during faults, participation in a grid balancing, etc [1]. This in turn increases the need to more powerful computational device and more distributed intelligence. These requirements make the application of digital control techniques very interesting. This is mainly because of the several advantages a digital controller offers when compared to an analog one; these advantages include [2]:

- ✓ The possibility it offers for implementing sophisticated control laws, taking care of nonlinearities, parameter variations or construction tolerances by means of self-analysis and auto-tuning strategies, very difficult or impossible to implement analogically.
- ✓ The flexibility inherent in any digital controller, which allows the designer to modify the control strategy, or even to totally reprogram it, without the need for significant hardware modifications.
- ✓ The complete absence of ageing effects or thermal drifts.

1.1 Power Filters

Beside the power converter and the control unit, the power filter is a key component for grid-connected converters to attenuate the harmonics of the injected grid current to comply with the standard grid codes; i.e. IEEE 519-1992 [3]. Two types of filters, *L* or *LCL* filters, are mainly used for this purpose as shown in Fig. 1.2. Compared to *L* type filters, *LCL* type filters offer the following advantages [4]–[11]:

1. Attenuation of -60 dB/decade for frequencies in excess of the resonance frequency.
2. Low grid current distortion and reactive power production,
3. Reduced filter size and weight for the same switching frequency.
4. Possibility of using a relatively low switching frequency for a given harmonic attenuation.

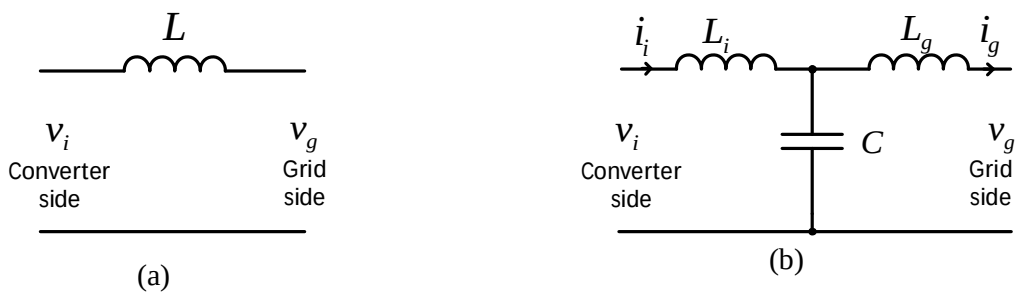

Fig. 1.2 Power filter types: (a) *L* type filter, (b) *LCL* type filter

1.2 LCL Filter Resonance

Fig. 1.3(a) shows the block diagram of the *LCL* filter. The transfer function relating the modulated converter voltage (v_i) to the grid side current (i_g) is expressed as $G_{ig}(s)$ in (1.1) where ω_{res}, expressed in (1.2), is the filter resonant frequency. Fig. 1.3(b) plots a conceptual Bode diagram for $G_{ig}(s)$.

$$G_{ig}(s) = \frac{i_g(s)}{v_i(s)} = \frac{1}{L_i L_g C s(s^2+\omega_{res}^2)} \tag{1.1}$$

$$\omega_{res} = 2\pi f_{res} = \sqrt{(L_i + L_g)/(CL_iL_g)} \tag{1.2}$$

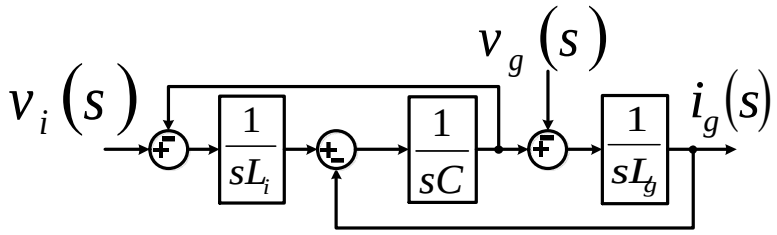

(a)

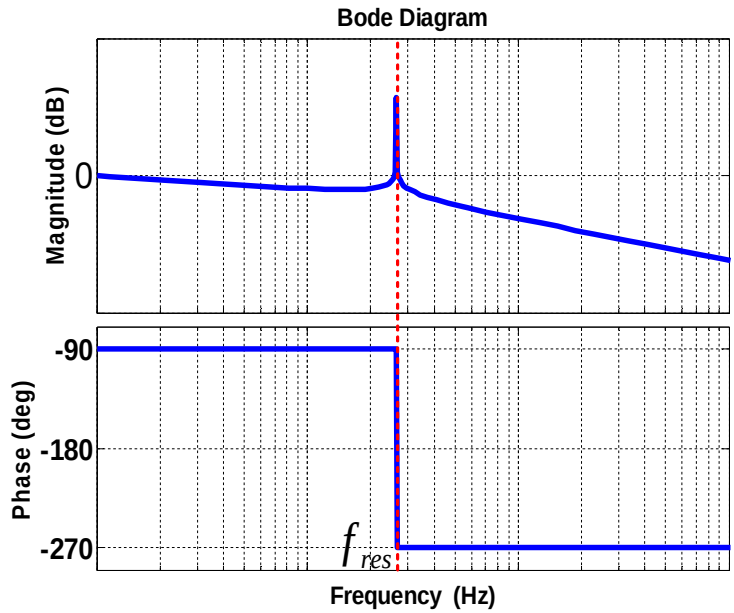

(b)

Fig. 1.3 Characteristics of LCL filter (a) block diagram, (b) Bode plot related the converter voltage to the grid current

The resonance of the *LCL* filter can cause instability of the current control loop and, in turn, represents a challenge for the controller designer. Moreover, resonance excitation, due to disturbances from other sources connected to the grid, can cause failure for other system components.

For digitally controlled converters, the instability effect of the *LCL* filter resonance is highly related to the inherent delay of the digital controller due to digital pulse width modulation process and computational time [12]–[16]. The origin of this delay along with some concepts related to the digitally controlled converters are explained in the next section. After that, the resonance damping methods are presented.

1.3 Digitally Controlled Converters

A single phase inverter connected to the grid through an *LCL* filter with the typical organization of its digital control system is shown in Fig. 1.4. Typically, the control system consists of two loops, the outer loop is responsible for regulation the input DC voltage; this is usually performed with proportional-integral (PI) regulator. The output of this loop is the reference current waveform to the inner current control loop which is responsible for regulating the grid current and response to grid disturbances. The outer loop is usually tuned to have a much lower bandwidth than the inner loop. Therefore, the two loops can be considered decoupled and independent analysis for each loop can be performed [16].

Considering the current control loop, the sensed grid current is sampled by an analog to digital converter (ADC) and the control calculations are performed by the DSP. The resultant modulation command is fed to digital pulse width modulator (PWM) where it is compared against a triangular carrier to generate the switch commands [2].

It should be noted here that the sampling process is synchronized to occur at the peak or the valley of the carrier waveform to avoid aliasing effect, [2], [17], [18].

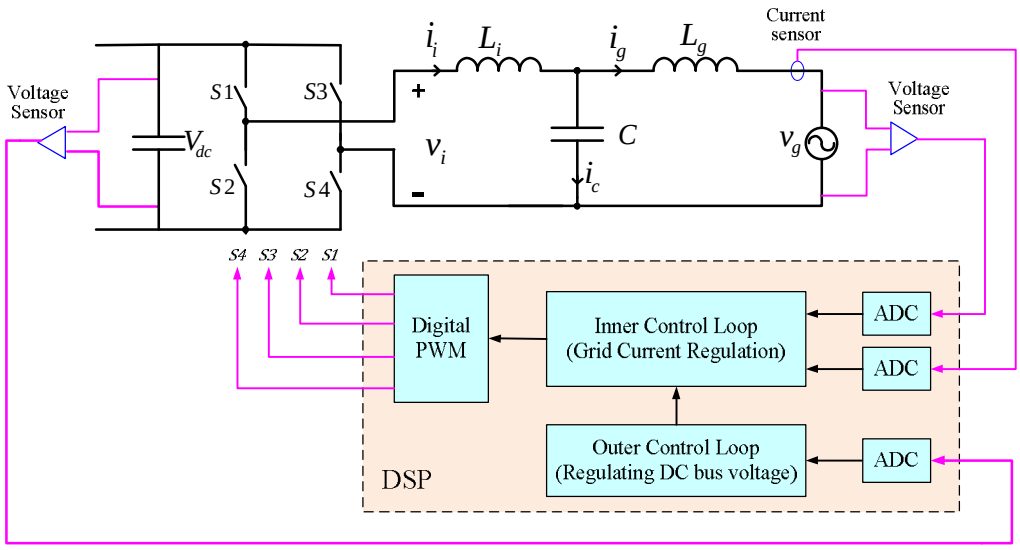

Fig. 1.4 Single phase grid-connected converter with typical organization of a digital control system.

1.3.1 Current Regulator

The current regulator is responsible for regulating the injected grid current, such that a high quality sinusoidal current is injected into the utility grid. To achieve this objective, the current controller should be able to reject the disturbance produced by the utility grid with ensuring a quick recover from transients.

Several current control techniques have been discussed in the literature such as linear proportional-integral (PI) and proportional-resonant controllers (PR) [16], [19]–[29], deadbeat controllers [30]–[36], model predictive current controllers [37]–[45], state feedback controllers [46]–[53], sliding mode controllers [54]–[57], and Hysteresis controllers [58]–[60].

Among these techniques, linear PR controllers are widely used as it has the following advantages [19], [61]:

- It offers fast dynamic response and zero steady state tracking error for sinusoidal signals.
- Avoiding the need to convert the system variables into the synchronous reference frame (*dq*-frame) and the associated need for a phase-locked loop (PLL). This significantly reduces the overall computation burden on control hardware and driving down system cost.
- Better suited for single phase systems, where the *dq*–transformation is difficult to apply.

Throughout this thesis, the PR controller is employed. The transfer function for PR controller is expressed as $G_c(s)$ in (1.3).

$$G_c(s) = K_p + \frac{K_r S}{S^2+\omega_o^2} \tag{1.3}$$

with $\omega_o = 2\pi f_o$ where ω_o and f_o are the fundamental grid frequency in rad/sec and Hz, respectively.

The proportional term (K_p) determines the bandwidth and stability phase margin. On the other hand, the resonant term $(K_r S/(S^2 + \omega_o^2))$ acts to eliminate the steady-state error [28], [61], [62].

The controller parameters are usually tuned so that the resonant term has negligible effect at the crossover frequency, so the system stability is mainly determined by the proportional term (*Kp*) [28], [61], [62].

Either the grid side current (i_g) or the inverter side current (i_i) can be controlled; both techniques are denoted as GCF (grid current feedback) and ICF (inverter current feedback), respectively. Feeding back the inverter side currents is reasonable if the current sensors are already built into the converter for protection purpose. In this case,

the filter phase shift must be compensated in order to set the power factor on the grid side. On the other hand, feeding back the grid current feedback is reasonable since one of the main objectives is the control of power factor at the point of the grid connection. In this case, the line current phase angle can be directly controlled [16]. Throughout this thesis, the grid current is adopted as the main controlled variable.

1.3.2 Digital Pulse Width Modulator (DPWM)

1.3.2.1 Basic Operation

A single leg inverter, shown in Fig.1.5, is used to explain the basic operation of DPWM. An equivalent model for the uniformly sampled digital pulse width modulator is shown in Fig. 1.6. A sinusoidal control signal $v_m(t)$, with frequency of ω_o ($=2\pi f_o$), is uniformly sampled with a sampling frequency of f_s ($= 1/T_s$, where T_s is the sampling period).

$$v_m(t) = V_{m-peak} \sin(\omega_o t) \tag{1.4}$$

The sampled signal is sent to an Zero-Order-Hold circuit (ZOH). The output of the ZOH, $v_{ms}(t)$, is compared with a triangular carrier waveform $v_{tri}(t)$. This comparison is shown in Fig. 1.7.

Both the switches S1 and S2 are operated as fo1low:

If $v_{ms}(t) > v_{tri}(t)$ then S1 is ON & S2 is OFF

If $v_{ms}(t) < v_{tri}(t)$ then S1 is OFF & S2 is ON

Based on this realization, the output voltage (v_{Ao}) is not a perfect sine wave and it contains voltage components at harmonic frequencies of the carrier frequency [63]. The frequency of the control signal (f_o) identifies the desired fundamental frequency of the output voltage. On the other hand, the frequency of the carrier waveform (f_{sw}) identifies the switching frequency.

Two indices, amplitude modulation index (m) and frequency modulation index (m_f), are identified as follow:

$$m = \frac{V_{m-peak}}{V_{tri-peak}} \tag{1.5}$$

$$m_f = \frac{f_{sw}}{f_o} \tag{1.6}$$

where $V_{m\text{-}peak}$ and $V_{tri\text{-}peak}$ are the amplitudes of the control signal (v_m) and carrier waveform (v_{tri}), respectively.

For large values of m_f, the averaged output leg voltage $(v_{AO})_1$ can be determined as in (1.7). Actually, this averaged value is equal to the fundamental component of the output voltage [63].

$$(v_{AO})_1 = \frac{V_{m-peak}}{V_{tri-peak}} \frac{V_{dc}}{2} \sin(\omega_o t) = m \frac{V_{dc}}{2} \sin(\omega_o t) \tag{1.7}$$

The waveforms of both the instantaneous leg voltage (v_{Ao}) and its fundamental component $(v_{Ao})_1$ are plotted in Fig. 1.7.

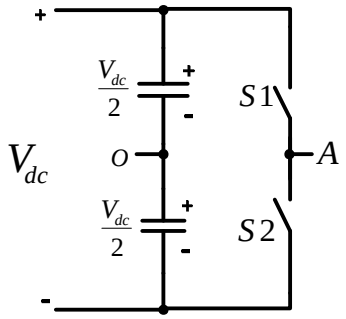

Fig. 1.5 One leg inverter

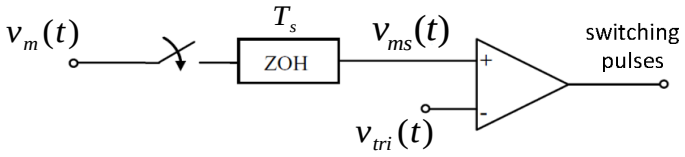

Fig. 1.6 Equivalent model of uniformly sampled DPWM

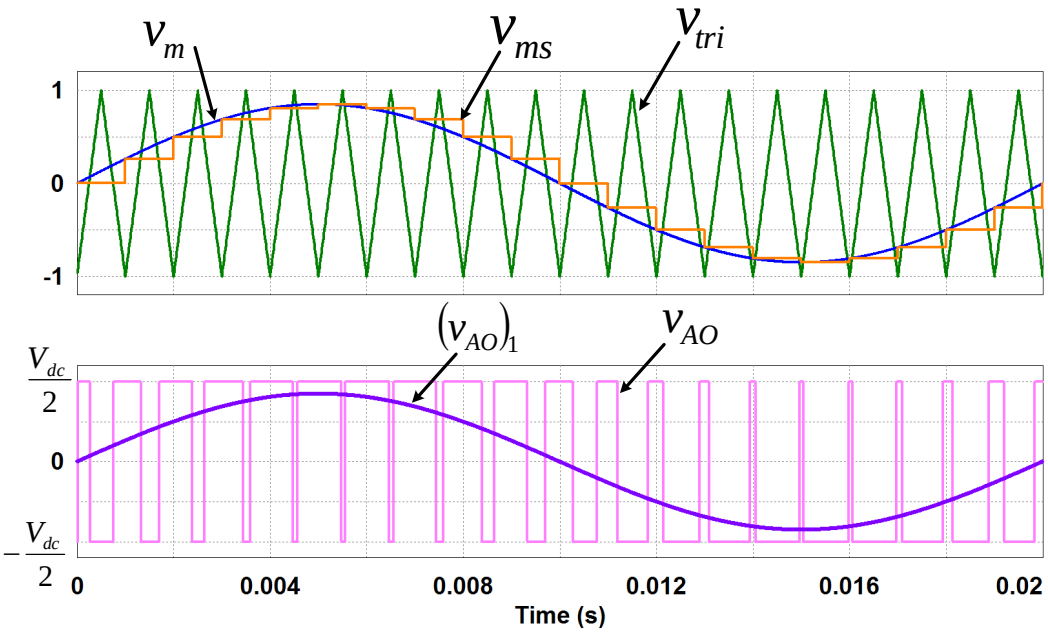

Fig. 1.7 Basic operation of DPWM, upper waveforms explain the ZOH and comparison process of the uniformly sampled DPWM, and lower waveforms are the instantaneous output leg voltage (v_{Ao}) and its fundamental component $(v_{Ao})_1$.

1.3.2.2 Delay in Digitally Controlled Converters

Two sources of delay can be identified as follow:

1. Because of the sample and hold operation, the sampled control signal will be constant over the whole sampling period. On the average, this effect can be modelled by a delay of half of the sampling period [2], [64].
2. An additional source of delay is the control algorithm computation delay (the time required by the processor to compute a new modulation signal value which is the input of DPWM). This time always represents a significant fraction of the modulation period. Then, the input to the modulator cannot be computed during the same modulation period when it has to be applied, it must be computed during the previous control algorithm iteration [2].

The above-introduced delays can be modelled in two ways:

1. In discrete time domain, Zero-Order-Hold (ZOH) discretization for the plant (*LCL* filter) along with a unit step delay (z^{-1}) is used to represent the above delays. The ZOH discrete representation for $G_{ig}(s)$ is expressed as $G_{ig}(z)$ in (1.8) with T_s denotes the sampling period [64].

$$G_{ig}(z) = \frac{T_s}{(L_i+L_g)}\left(\frac{(1-\alpha)z^2-2(cos(\delta)-\alpha)z+(1-\alpha)}{(z-1)(z^2-2z\,cos(\delta)+1)}\right) \tag{1.8}$$

where $\delta = \omega_{res}T_s$ and $\alpha = \frac{sin(\omega_{res}T_s)}{\omega_{res}T_s}$

2. In continuous time domain, the delays can be emulated using an exponential delay function of $G_d(s)$. In this case, the ZOH delay is approximated by half sampling period delay, and the computation delay is modelled by one sampling period [2], [64]. Then, a total time delay (T_d) of one and half sampling period ($T_d = 1.5T_s$) can be used to represent the total delay as follow.

$$G_d(s) = e^{-1.5sT_s} \tag{1.9}$$

The control system representations using the above two methods are respectively shown in Figs 1.8(a) and 1.8(b) where G_c is the fundamental current regulator and i_{ref} is the desired value for the grid current.

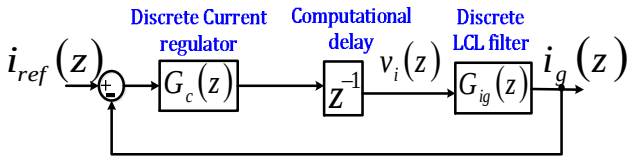

(a)

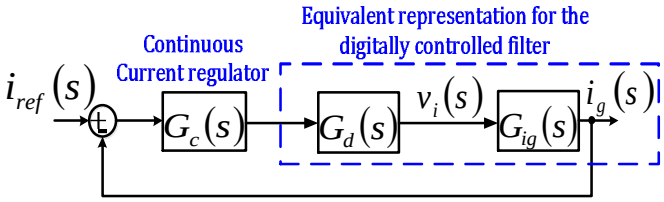

(b)

Fig. 1.8 Delay representation in digital control systems (a) using discrete representation, (b) using continuous time domain approximation.

1.3.2.3 Inherent Damping of Single Control Loop

The stability of single control loop systems based on grid current feedback has been investigated [12], [14]–[16], [62], [65]–[68]. It was indicated in [16] the stability is closely related to the ratio of sampling frequency to the *LCL* filter resonance frequency, however this relationship was not identified. Using Nyquist stability criterion, it was shown in [69] that the system stability of can be maintained only for high resonant frequencies. In [13] and [70], it was found that the single control loop systems can be stable only if the resonant frequency is lower than one-six of the sampling frequency (necessary condition).

This stability range has been confirmed in [71] using a virtual impedance model for the single control loop. Figs. 1.9 show the derivation of this virtual impedance model.

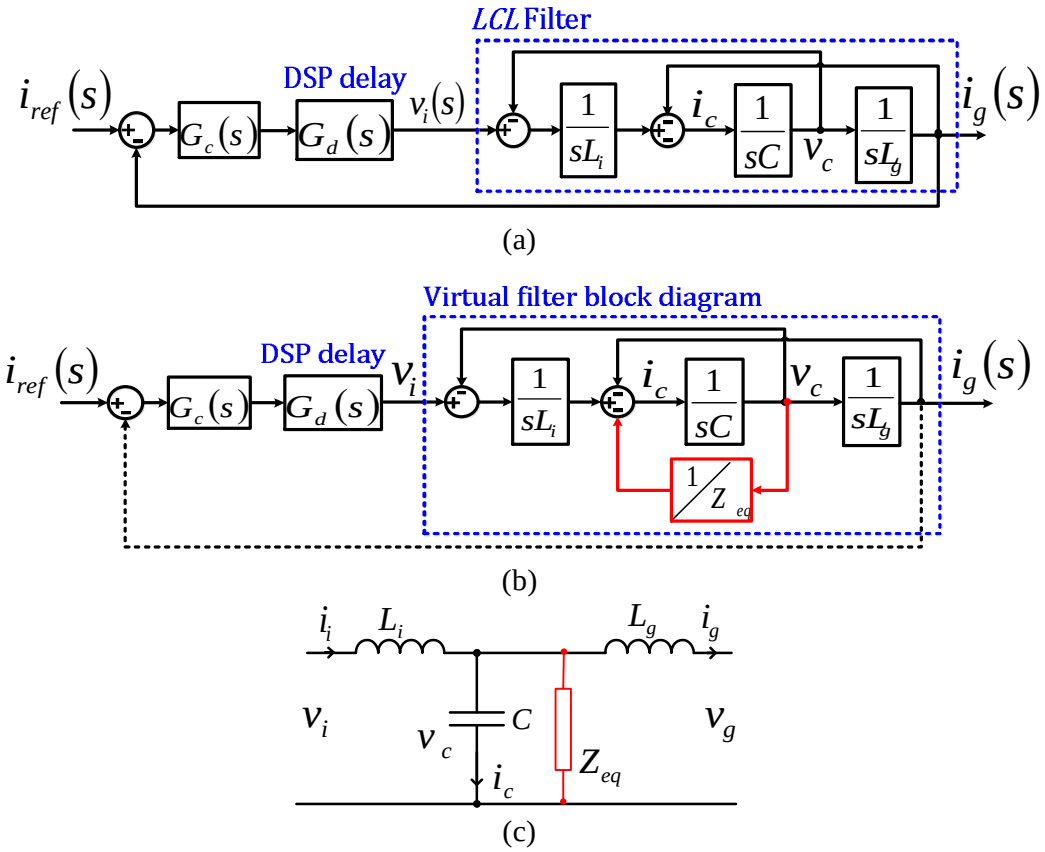

Fig. 1.9 Single loop control using grid current feedback (a) Original system, (b) Equivalent block diagram. (b) Virtual equivalent circuit.

It is obvious that equivalently a virtual impedance Z_{eq} is connected in parallel with the capacitor C. With expressing the fundamental current regulator $G_c(s)$ by its proportional gain of K_p this impedance is expressed as follow:

$$Z_{eq} = \frac{-L_i L_g}{K_p}\omega^2(\cos 1.5\omega T_s + j\sin 1.5\omega T_s) = R_{eq}(\omega) \| \frac{1}{j\omega C_{eq}(\omega)} \quad (1.10)$$

where $R_{eq}(\omega) = \frac{-L_i L_g \omega^2}{K_p \cos(1.5\omega T_s)}$, $C_{eq}(\omega) = \frac{K_p \sin(1.5\omega T_s)}{L_i L_g \omega^3}$

Therefore, a resistor R_{eq} and a capacitor C_{eq} are in parallel with the filter capacitor *C*. R_{eq} is frequency dependent, which provides a frequency dependent damping. It can be shown that R_{eq} is positive for frequencies above $f_s/6$. Therefore, f_{res} is required to be more than this critical value for stability (necessary condition).

1.4 Resonance Damping Methods:

There are mainly two methods to damp the *LCL* filter resonance; passive and active damping.

- **Passive damping:** by adding a resistor to introduce the damping effect [72]–[78]. Many passive damping configurations have been presented for this purpose as shown in Fig. 1.10. However, passive damping produces power losses which decrease the overall system efficiency and increases the filter size and weight [79]–[81].
- **Active damping:** by modifying the control algorithm to introduce the damping effect without the need for additional passive elements. Number of active damping methods have been presented in the literature.

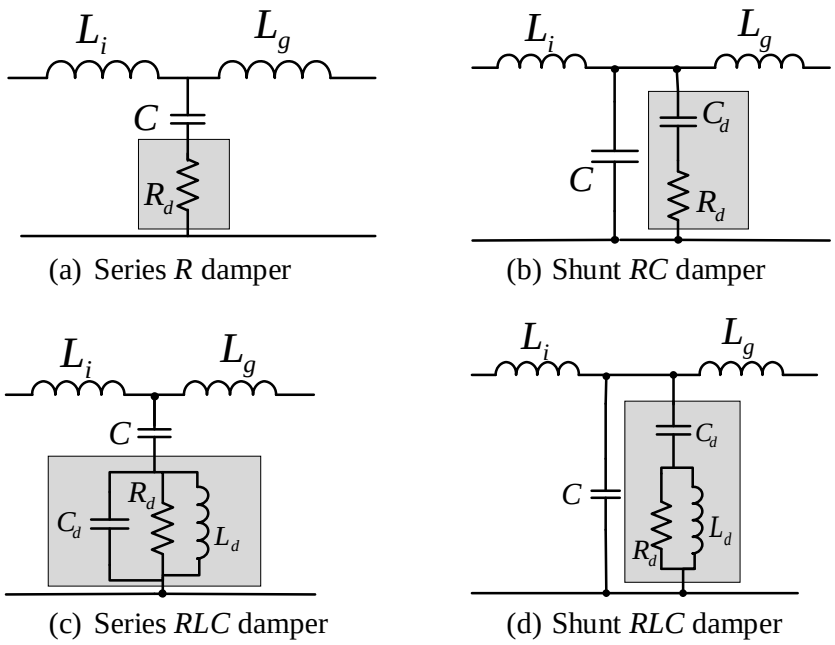

(a) Series *R* damper (b) Shunt *RC* damper

(c) Series *RLC* damper (d) Shunt *RLC* damper

Fig. 1.10 Passive damping configurations

1.5 Problem Definition

From the above discussion, it is shown that the stability of single control loop can be maintained only for resonant frequencies higher than one-sixth of the sampling frequency. However, the stability violates if the resonant frequency decreases to values less than this critical value. Such decreasing in the resonant frequency can occur with the frequent increase in the grid inductance [82]–[86]. For that reason, damping techniques have to be adopted to suppress the resonance of the LCL filters. Passive damping, by using a resistor, can be used to cope with this challenge. However, it causes power losses. Thus active damping by modifying the control algorithm is preferred. Number of active damping methods have been discussed in the literature. These methods along with their limitations are presented in the next section.

1.6 Literature Review on Active Damping Methods

1.6.1 Filter-Based Active Damping:

A digital filter is plugged in, in cascade to the main controller, to damp the unstable dynamics [69], [87]–[92]. A general discrete transfer function for such filter is expressed in (1.11) as $D(z)$. The system block diagram is shown in Fig. 1.11 and a conceptual bode plot for $D(z)$ is shown in Fig. 1.12. The main idea is compensating the *LCL* resonant peak by inserting an anti-resonance peak at certain notch frequency denote as f_{noth}.

$$D(z) = \frac{a_2 z^2 + a_1 z + a_0}{b_2 z^2 + b_1 z + b_0} \tag{1.11}$$

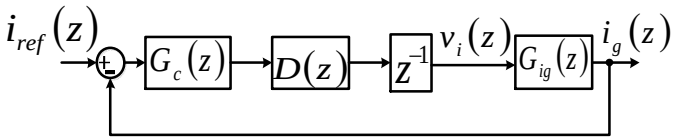

Fig. 1.11 Closed loop system with using a digital notch filter.

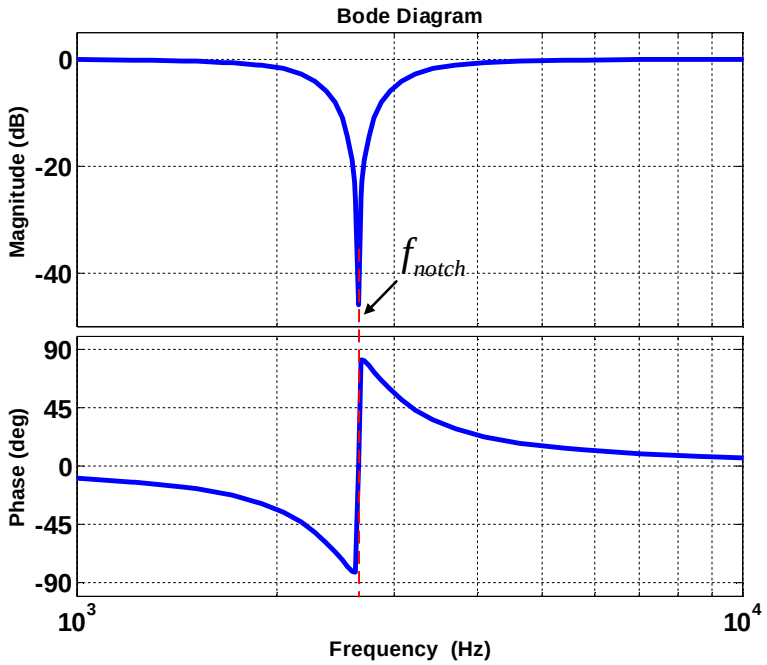

Fig. 1.12 Conceptual characteristics of digital notch filter

In [69], the performance of three digital filters (low-pass filter, lead-lag filter and notch filter) has been studied for grid and converter current based control at low, medium and high resonant frequencies. The performance of each type has been evaluated in terms of bandwidth, complexity, robustness and stability margins. Among these types, the notch-filter offered the most flexible and effective damping behavior.

In [89], multiple notch filters in series are proposed to attenuate multiple resonance peaks. The order of the cascaded notch filter is determined by the number of peaks, of which the magnitude is above 0 dB. In order to make the notch filter insensitive to the variation of the resonances due to the fluctuation of the filter parameters, the bandwidth of the notch filter has been expanded. However, such expanding would potentially reduce the system phase margin, and hence, a tradeoff during the design of the notch filter has to be considered.

In [90], optimum filter parameters are determined using genetic algorithm to have the desired stability of the system and to preserve dynamics performance. Over wide range of resonant frequencies, both the grid current and the converter current feedback are considered. Compared to using other non-linear techniques, using the genetic algorithm does not need a priori knowledge for the range in which the active damping parameters should lie. This makes using the genetic algorithm more suitable as the aim is to have a tuning method that should work with different resonant frequencies and for different system configurations.

In [91], a straightforward tuning procedure for a notch filter self-commissioning has been proposed. In order to account for the grid inductance variations, the resonance frequency is estimated firstly using the Goertzel algorithm and later used for tuning the notch filter. However, this requires an extra computational resources in the existing control processor. Another technique to increase the system robustness against grid

inductance variation, has been adopted in [92] where it is suggested to design the frequency of the notch filter to be less than the resonant frequency.

Recently, the notch filter is employed along with a passive RC damper and harmonic selective compensator to increase both the system robustness and the system capability to reject the low-order grid voltage harmonics [93].

The easy plug-in feature and the physical meaning are the two main advantages of this approach. However, using such cascade network decreases the closed loop system bandwidth. Moreover, it is very sensitive to filter parameter variations which can likely occur with different number of grid-tied inverters in parallel [82]–[86].

1.6.2 Multi-Loop Active Damping Methods:

In this method, the damping is achieved through an inner loop from one of the filter states (capacitor current, capacitor voltage, grid current or converter current).

1.6.2.1 Capacitor-Current-Based Active Damping:

The block diagram for this method is shown in Fig. 1.13 where the capacitor current is fed back through a proportional feedback of H_d.

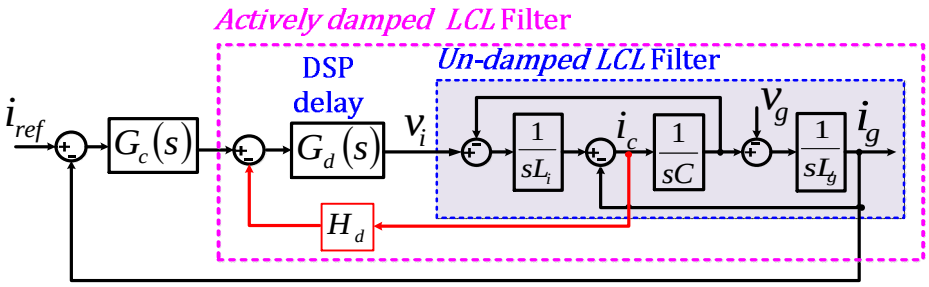

Fig. 1.13 Active damping using capacitor current feedback.

This method was firstly proposed in [94] where it was shown that a proportional feedback from the capacitor current results in the same damping effect as a series

resistor connected to the filter capacitor. Further studies have been introduced in the literature to investigate the damping behavior for this method [24], [28], [95]–[104].

In [24], with the converter side current controlled, capacitor-current-based active damping has been investigated considering different ratios of the resonant frequency with respect to the sampling frequency. It was shown that resonance poles can be damped into the unity circle with the proper tuning of the proportional feedback at high and medium resonant frequencies. However, if the resonant frequency gets lower, resonance damping suffers from interactions with the fundamental controller. For this reason, resonance damping and stability get worse**.** However, the specific boundaries for these regions - low, medium and high resonant frequencies- are not given to design system parameters.

In [28], co-design steps for the capacitor current feedback along with the fundamental current regulator have been presented. Two types of controllers have been considered, PI and PR regulators. By dealing with the interaction between the current regulator and active damping coefficient, satisfactory regions of the controller parameters have been obtained for given specifications of steady state errors and stability margins. However, the design steps did not consider the transpose delay due to discrete implementation.

In [95], a differentiation of the capacitor current has been adopted to produce the damping effect with the converter side current controlled. It was clarified that this method can damp resonance effectively only for high resonant frequencies. However, for low resonant frequencies, the system stability can only be achieved by lowering the proportional gain of the current controller which reduces the system bandwidth, or by using more complex control algorithms like state space control.

In [96], [97], a virtual impedance model for the discrete active damping loop has been presented. Fig. 1.14 show the derivation of this virtual impedance model using the equivalent *s*-domain system.

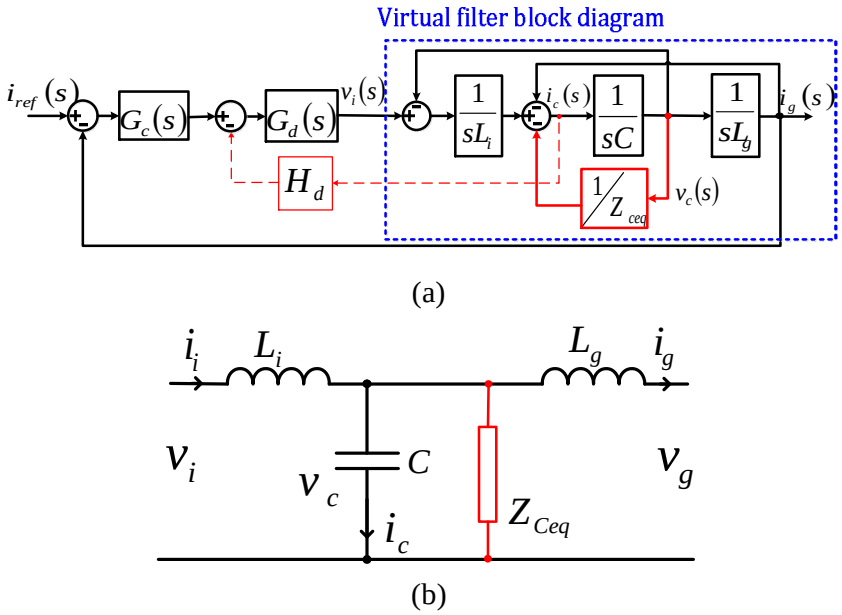

Fig. 1.14 Equivalent representation of capacitor–current active damping. (a) Block diagram representation. (b) Equivalent circuit.

It is obvious that equivalently a virtual impedance Z_{Ceq} is connected in parallel with the capacitor *C*. This impedance is expressed as follow:

$$Z_{Ceq} = \frac{L_i}{H_d C}(\cos 1.5\omega T_s + j \sin 1.5\omega T_s) \tag{1.15}$$

Using the above expression, it can be shown that the real part of this impedance becomes negative for resonant frequencies greater than a critical value of one-sixth of the sampling frequency. This implies a non-minimum phase behavior, owing to the presence of open loop unstable poles.

Although the closed loop system can be stable for resonant frequencies more than the critical value of one-sixth of the sampling frequency, It was shown in [96], [97] that this non-minimum phase behavior declines the system robustness against grid inductance variation which can occur particularly in weak grids. This, in turn, worse

the system stability. In addition, this behavior declines the damping effect as a resonant peak more than 0 dB has to be allowed to stabilize the closed loop system [97].

Modified feedback loops of the capacitor current have recently been proposed to avoid the non-minimum phase behavior over a wider range of resonant frequencies [96]–[99]. In [98], this critical resonant frequency has been extended to 0.25 of the sampling frequency using an improved capacitor-current-feedback active damping method. On the other hand, in [97], this limit has been further extended to one-third of the sampling frequency using a virtual RC damper instead of the conventional virtual *R* damper. Finally, in [96] and [99], it was shown that using a high sampling rate in the active damping loop contributes to extend the non-minimum phase behavior.

However, feeding back the capacitor current needs a high precision current sensor; this in turn increases the overall cost. To avoid the need for more sensors, model-based estimation methods have been proposed in the literature. In [105], a virtual flux model has been derived for the *LCL* filter. Based on the derived model, the capacitor current has been estimated using a second derivative of the capacitor virtual flux. In [106], [107], an observer has been designed using the pole placement technique. However, the performance of these methods is highly dependent on the *LCL* filter parameters which can likely changed in the real operation. Moreover, these methods increase the system complexity.

1.6.2.2 Capacitor-Voltage-Based Active Damping

The block diagram for this method is shown in Fig. 1.14 where the capacitor voltage is fed back through a general transfer function of $H_v(s)$ [108]–[116]. Ideally, this needs a differentiation of the capacitor current. However, for practical implementation, such differentiation can amplify the noise and decline the overall controller performance. In [108], a lead–lag network in the synchronous reference

frame applied to the feedback from the capacitor voltage. The analysis was carried out in s-domain with approximating the PWM transport delay as a first order pole. It was shown that the damping effectiveness depends on the bandwidth of the inner active damping loop compared to the outer current control loop. However, an increasing in the response overshoot was observed due to the active damping loop.

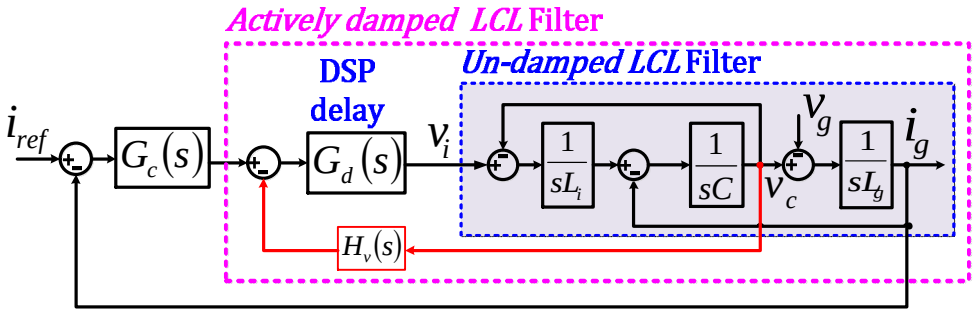

Fig. 1.14 Active damping using capacitor voltage feedback.

In [109], the lead-lag network has been designed to act sharply in a little range around the resonant frequency without influence at low frequencies and switching frequencies. Using the pole-map plot, it was shown that both the system stability and the damping behavior are highly dependent on the network gain; optimum value for this gain is determined using the system pole-map with sweeping the network gain.

In [110], high-pass filter HPF is employed in *dq* axis for active damping purpose. In this work, the d and q axis components of the capacitor voltage are low pass filtered. To decrease the high harmonic delay, the HPF is realized by subtracting the low pass filtered capacitor voltage components from their corresponding *dq* axis components. The capacitor voltage has been estimated by subtracting the modulated converter voltage and the voltage across the inverter side inductor which, in turn, has been determined by differentiation the converter side current. To avoid the switching noise multiplication problem due to the current differentiation, the ac currents have been sampled during the middle of the zero-vector states in the conventional SVM. The same

strategy for estimating the capacitor voltage has been adopted in [111]; however, a lead-lag compensator feedback has been used. This lead lag compensator has been tuned to a maximum lead angle at the resonant frequency.

In [112], a systematic tuning steps for the lead-lag network to behave as a differentiator as possible around the resonant frequency has been presented; the effect of the PWM and computation delays of the DSP was considered. Stability is studied by means of the root locus analysis in -plane. The robustness against the grid inductance variation is also analyzed. In consistent with the obtained results from [109], it was shown that there an optimum network gain for stability and damping. This gain was determined using the pole-map plot for the closed loop system. It was indicated also that this lead-lag network can be used effectively over the limited range of resonant frequencies between 1/3.2 and 1/3.4 of the sampling frequency [112].

In [113], the capacitor voltage has been used to determine a harmonic current reference component to emulate a virtual damping resistance. This is achieved in two steps; firstly, the harmonic components of the capacitor voltage have been detected using a second-order Butterworth low-pass filters; after that, a harmonic current reference component has been determined by dividing the detected harmonic components by the virtual damping resistance. It was shown that this method is effective to damp multi-resonance in parallel grid-connected converters.

To match the derivative function without associated noise amplification, two derivatives methods have been recently proposed using either second-order or non-ideal generalized integrator [115], [116]. However, the system becomes more complex.

1.6.2.3 Grid-Current-Based Active Damping

The block diagram for this method is shown in Fig. 1.15 where the grid current is fed back through a general transfer function of $H_g(s)$.

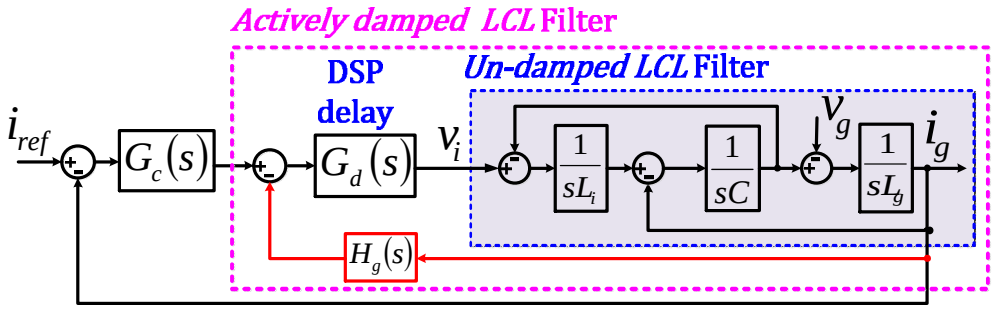

Fig. 1.15 Active damping using capacitor voltage feedback.

In terms of number of sensors and system complexity, grid-current-based active damping is more preferred than capacitor-current-based or capacitor-voltage-based active damping techniques; this is because there is no need to additional sensors or complicated control algorithms. Ideally, this needs an s^2 term in the active damping loop [117]; however, it is not implemented practically due to the noise amplification. Two approaches have been presented in the literature to overcome this issue: one approach employs a second order Infinite Impulse Response (IIR) filter [118]. To acquire robustness against parameter variation with adequate stability margins, the phase of the IIR is tuned to compensate the delay of the DSP and to show a flat characteristics around the resonant frequency. On the other hand, to limit the effect of the IIR around resonant frequency without deterioration of the fundamental current compensation, the gain of the IIR has been tuned to be large at resonant frequency relative to its magnitude at low frequencies. However, the control system is complicated and many iterations are needed to meet pre-specified behavior.

The other approach employs HPF of the grid current feedback [117], [119], [120]. In [117], the feasibility of using two types of filters, first order and second order filter, has been investigated. In terms of noise amplification, phase characteristics, low frequency range attenuation and preserving adequate stability characteristics, the first order high pass filter show superiority over using higher order filters. Based on this

conclusion, the first order HPS has been tuned to behave as the ideal s^2 term around the resonant frequency. However, there are no straightforward design steps introduced especially for the discrete implementation.

This approach has been further investigated in [119] where an independent design for the HPF and the Synchronous Rotating Frame Proportional-Integrator (SRFPI) current regulator has been proposed. However, *d-q* axis coupling of the *LCL* filter has been ignored. This ignorance can lead to an imprecise evaluation for the system performance especially at the resonant frequency. In [117] and [119], there is no consideration for the transport delays of the digitally controlled system and their effect on the open loop system stability which, upon violation, can decline the damping performance and the system robustness. Moreover, as indicated in [120], both the active damping loop and the fundamental current regulator must be co-designed together to meet pre-specified performance.

Based on *s*-domain emulation of the digitally controlled system, a virtual impedance model for the grid-current-based actively damped filter has been derived in [120] as a shunt impedance across the grid side inductance. Based on this realization, it was derived that unstable open loop behavior can be avoided for resonant frequencies up to 0.27 of the sampling frequency. However, such *s*-domain emulation cannot accurately represent the digitally controlled system aspects. Moreover, for certain resonant frequency, it could not identify the parametric influence of the HPF on the open loop stability. Consequently, the tuning process becomes tedious and many iterations are needed to co-design the HPF along with the fundamental current regulator without open loop stability violation. In addition, it is cost-effective to design *LCL* filters with higher resonant frequencies, and without violation of open loop stability especially when selective harmonic compensation is of concern [97].

1.7 Research Objectives

As introduced in the above review, active damping is more preferred over passive damping which increases the power losses. Number of active damping methods have been presented in the literature. Each one of these methods has its own advantages and disadvantages in terms of its ability to avoid the non-minimum phase behavior, the required number of sensors, control system complexity and the tuning steps of the control parameters.

In order to overcome the limitations of the existing active damping methods, some novel algorithms and analysis are proposed. Firstly, an observer in the control system is employed to estimate the capacitor current without the need for additional sensors. After that, a novel two state feedback active damping technique for the LCL filter resonance is proposed using the capacitor voltage and the grid current. Finally, an investigation for grid-current-based active damping method is presented to improve its performance.

1.8 Thesis Outlines

The Thesis is divided into five chapters. The outlines of these chapters are as follows:

In chapter one, a theoretical background about LCL filters, resonance problem and digitally controlled grid-connected converters are introduced. A literature review about the existing damping techniques along with their limitations are presented as well.

In chapter two, an observer in the control system is employed to estimate the capacitor current without the need for additional sensors. A systematic design of the observer loop is presented. The control algorithm is implemented in stationary reference frame to reduce the overall computation burden on control hardware. The

results show that the observer-based system offer a good damping behavior without the need for additional sensors. This, in turn, reduces the overall cost.

In chapter three, a novel active damping method using two feedback loops of the capacitor voltage and the grid current is proposed. The proposed method is derived in the continuous time domain with a discussion for its discrete implementation. To show the superiority of the proposed method, a comparative study is presented. Compared to capacitor-current-based method, the cost is reduced by omitting the high cost current sensor. Moreover, the non-minimum phase behavior is avoided over wide range of resonant frequency. Compared to capacitor-voltage-based method, the proposed method behaves effectively over wide range of resonant frequencies without stability violation or the need to a differentiator which amplifies the noise. Compared to grid current based method, straightforward co-design steps for the active damping loops along with the fundamental current regulator are proposed. The superiority of the proposed method is verified over wide range of resonant frequencies.

In chapter four, Active damping using high-pass filter (HPF) of the grid current is investigated. A detailed study for the actively damped filter in discrete time domain is introduced. Limits for the HPF parameters are derived in order to avoid the non-minimum phase behavior. Based on this investigation, the performance of this method is highly improved where the ability to avoid the non-minimum phase behavior is extended up to resonant frequencies about 0.39 of the sampling frequency. In addition, straightforward co-design steps for the HPF along with the fundamental current regulator are proposed. Numerical example and experimental work are carried out to confirm the obtained results.

Chapter five – the last chapter in the thesis – includes both the final summary and the conclusion outline for the thesis and the expected extended future work.

Chapter 2:

Design and Analysis of Observer-Based Active Damping for the LCL Filter Resonance

2.1 Introduction

It was proved that the proportional feedback of the filter capacitor current is equivalent to a resistor in series with the filter capacitor [94]. This active damping method is simple, flexible, effective and robust. However, it needs an additional high-precision sensor to get the capacitor current or voltage, and this increases the overall cost of the system.

To decrease the required number of sensors, the capacitor current can be estimated using model-based analytical methods. Observer based active damping technique have been proposed to get the non-measured value of the capacitor current [107]. However, it has been applied mainly in the *dq* synchronous reference frame which increases the control effort. Also, in the literature, it was applied with control algorithms based on converter side current control. However, one of the main objectives of the whole control system is controlling the power factor at the point of grid connection [16].

This chapter introduces a systematic design of the observer-based active damping technique. The grid current is adopted as the main controlled state with taking into account the transport delay due to digital implantation. The control algorithm is implemented in stationary reference frame.

2.2 Observer-Based Active Damping System

Fig. 2.1 shows a single phase inverter connected to the grid through an LCL filter. The plant (inverter + filter) transfer function is expressed in (2.1) as $G_f(s)$ where m is the modulation index (control signal to PWM).

$$G_f(s) = \frac{i_g(s)}{m(s)} = \frac{V_{dc}}{L_i L_g C s(s^2+\omega_{res}^2)} \tag{2.1}$$

$$\omega_{res} = \sqrt{(L_i + L_g)/(C L_i L_g)} \tag{2.2}$$

The observer-based system is shown in Fig. 2.2. For design purpose, a state space model for the LCL filter is firstly derived as introduced in the next section.

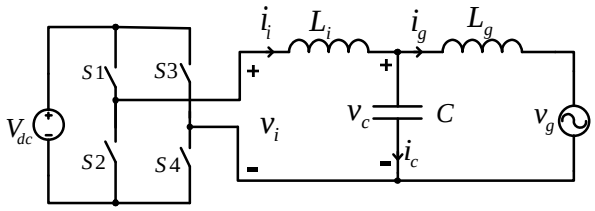

Fig. 2.1. Single phase inverter connected to the grid through an LCL filter.

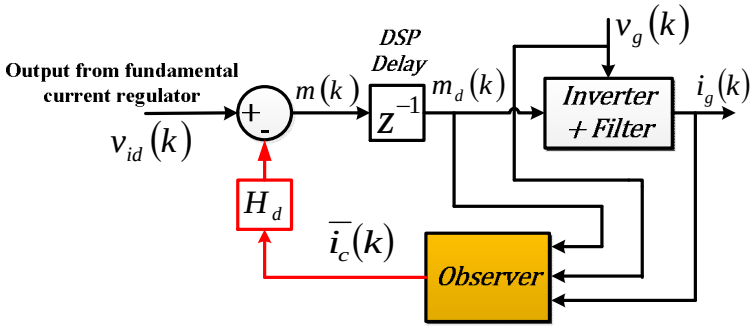

Fig. 2.2. Observer-based active damping system.

2.2.1 Filter State Space Model

The continuous state space model for the LCL filter is expressed as in (2.3)

$$\frac{dx}{dt} = Fx + GU \tag{2.3}$$

with $x(t) = \begin{bmatrix} i_g \\ i_i \\ v_c \end{bmatrix}, F = \begin{bmatrix} 0 & 0 & 1/L_g \\ 0 & 0 & -1/L_i \\ -1/C & 1/C & 0 \end{bmatrix}, G = \begin{bmatrix} 0 & -1/L_g \\ V_{dc}/L_i & 0 \\ 0 & 0 \end{bmatrix}, U = \begin{bmatrix} m(t) \\ v_g(t) \end{bmatrix}$

The filter discrete model can be expressed as in (2.4)

$$x(k+1) = \varphi x(k) + \Gamma U(k) \tag{2.4}$$

where $\varphi = e^{FT}$, $\Gamma = \sum_{k=0}^{\infty} \frac{F^k T_s^{k+1}}{(k+1)!}$

Considering the DSP delay due to computation and digital PWM operation, the modulation index input will be $m_d(k)$ instead of $m(k)$ where:

$$m_d(k) = m(k-1) \tag{2.5}$$

then, the discrete state model is re-written in (2.6) as follow.

$$x(k+1) = \varphi x(k) + \Gamma U_d(k) \tag{2.6}$$

where $U_d(k) = \begin{bmatrix} m_d(k) \\ v_g(k) \end{bmatrix}$

2.2.2 Observer Design

Using Luenberger observer technique [64], the observer state space model is expressed in (2.7).

$$\begin{aligned} \bar{x}(k+1) &= (\varphi - L_p H)\bar{x}(k) + [\Gamma \quad L_p] \begin{bmatrix} U_d(k) \\ i_g(k) \end{bmatrix} \\ \bar{y}(k) &= H\bar{x}(k) \end{aligned} \tag{2.7}$$

with $H = [-1 \quad 1 \quad 0]$.

In (2.7), L_p is the weighting matrix for the correction part between the measured grid current (i_g) and its estimated value. The value of L_p depends on the observer poles which should be at least two times faster than the poles of the plant (actively damped filter) to do not make deterioration for the dynamic characteristics [64]. In our case, the value of L_p is tuned to obtain observer poles equal to three times the plant poles.

2.3 Control Parameters Design

Since the observer poles are chosen to be faster than the plant poles, the fundamental current regulator can be designed separately from the observer.

2.3.1 Fundamental Current Regulator Design

The transfer function for a proportional resonant (PR) controller is expressed as $G_c(s)$ in (2.8) with $\omega_o = 2\pi f_o$ where ω_o and f_o are the fundamental grid frequency in rad/sec and Hz, respectively.

$$G_c(s) = K_p + \frac{K_r S}{S^2+\omega_o^2} \tag{2.8}$$

For the PR regulator coefficients, they are tuned to achieve a pre-specified value of crossover frequency (ω_c) as follow.

- K_p tuning: For frequencies greater than the fundamental frequency (ω_o), the PR controller function can be reduced to K_p since the resonant gain has negligible effect above ω_o [28]. Since the crossover frequency (ω_c) should be adequately higher than the fundamental frequency, K_p can be determined as in (2.9) [13]:

$$K_P = \omega_C\left(L_i + L_g\right) \tag{2.9}$$

- **K_r tuning:** This parameter is tuned to ensure that its phase contribution is small at the crossover frequency (ω_c) as in (2.10) [13].

$$K_r = \frac{K_p\omega_c}{10} \tag{2.10}$$

2.3.2 Design the Active Damping Coefficient (H_d)

This value is tuned to achieve the best possible damping. Fig. 2.3(a) shows the block diagram for the discrete system of the observer-based actively damped filter. The grid voltage is considered as a disturbance input. $G_{gc}(z)$ and $G_{mc}(z)$ are the discrete transfer functions from the inputs of the observer, measured grid current and inverter modulation index respectively, to the estimated capacitor current.

To derive an expression for the actively damped filter, this system is manipulated as shown in Figs. 2.3(b) till 2.3(d) where,

$$G_1(z) = \frac{1}{1+z^{-1}H_d G_{mc}(z)} \tag{2.11}$$

From Fig. 2.3(d), the transfer function of the observer-based actively damped filter can be expressed in (2.12) as $G_{f\text{-}d\text{-}obs}$. The closed loop system transfer function is expressed in (2.13) as $T_{closed\text{-}obs.}$

$$G_{f-d-obs}(z) = \frac{z^{-1}G_1(z)G_f(z)}{1+z^{-1}H_dG_1(z)G_f(z)G_{gc}(z)} \tag{2.12}$$

$$T_{closed-obs}(z) = \frac{G_{f-d-obs}(z)G_c(z)}{1+G_{f-d-obs}(z)G_c(z)} \tag{2.13}$$

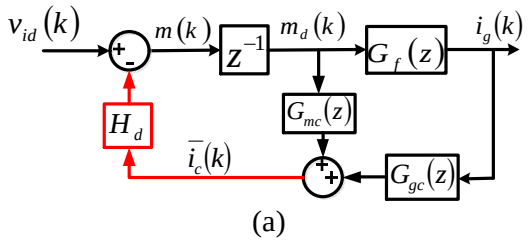

(a)

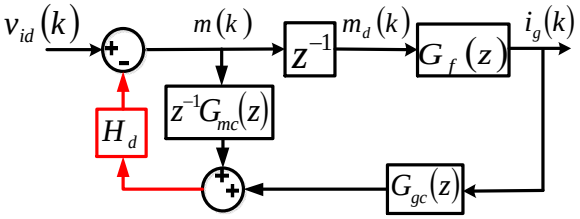

(b)

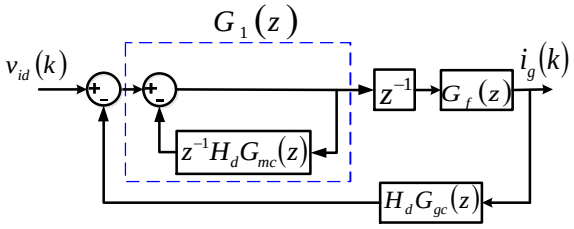

(c)

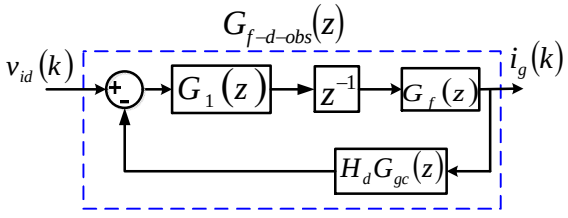

(d)

Fig. 2.3 (a) till (d) Block diagram manupulation for the observer-based actively damped filter.

2.4 Robustness against Grid Inductance Variation

Table 2.1 presents the parameters of the grid-connected single phase invereter. The system robustness is investigated at three capacitance values, corresponding to three resonant frequencies of $0.147\omega_s$, $0.195\omega_s$ and $0.23\omega_s$, denoted as ω_{res1}, ω_{res2} and ω_{res3}, respectively. Firstly, the fundamental current regulator is designed for certain crossover frequency (ω_c). To achieve an adequate phase margin, ω_c should be adequately higher than the fundamental frequency and below the resonant frequency value. For this purpose, the value of ω_c is considered as 0.33 of the corresponding resonant frequency of each case. Then, using (2.9) and (2.10), K_p and K_r are determined.

Table 2.1
System parameters

Symbol	Quantity	Value
P	Rated power	400 W
V_g	Grid voltage	100 V
F_o	Grid Frequency	50 Hz
V_{dc}	DC Voltage	180 V
L_i	Inverter side inductance	2.75 mH
L_g	Grid side inductance	1.2 mH
C	Capacitance	14.1 µF, 8 µF, 5.7 µF
f_{sw}	Switching Frequency	10 kHz
f_s	Sampling Frequency	10 kHz

Table 2.2
Designed Control Parameters

C (µF)	H_d	K_p	K_r
14.1	9	12	3652
8	6	15.94	6436
5.7	5	18.9	9033

The pole maps of the closed loop system are plotted using (2.13) with sweeping the active damping coefficient (H_d). These pole maps are shown in Figs. 2.4(a), 2.5(a) and 2.6(a) for ω_{res1}, ω_{res2} and ω_{res3}, respectively. Using these plots, the values of H_d

corresponding to the farthest resonant poles inside the unit circle are selected to achieve the best possible damping. Table 2.2 lists the designed control parameters.

The system robustness is studied by plotting the closed loop pole map with increasing the grid side inductance. For each resonant frequency, the grid side inductance is swept starting from its original value (L_g) till $3L_g$. The corresponding pole maps are shown in Figs. 2.4(b), 2.5(b) and 2.6(b) for ω_{res1}, ω_{res2} and ω_{res3}, respectively.

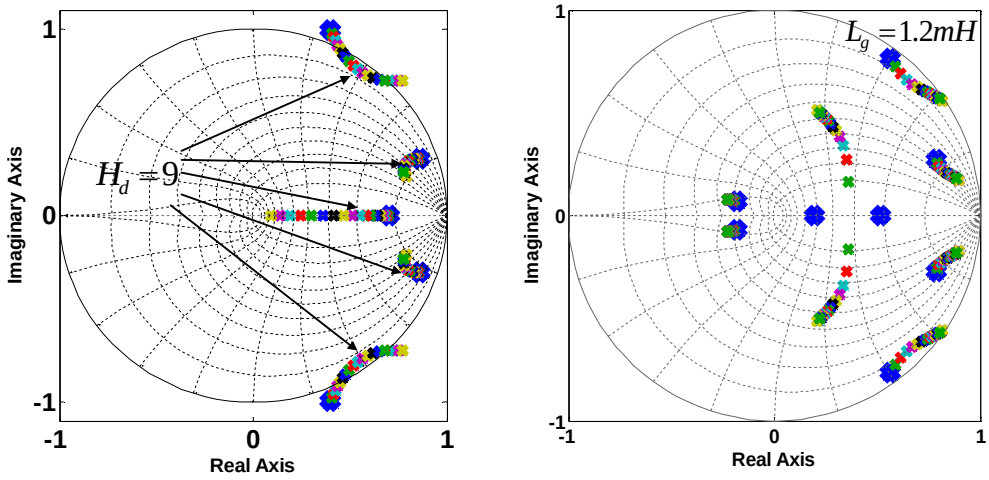

(a) (b)

Fig. 2.4. Pole map of $T_{closed\text{-}obs}$ (z) for ω_{res1}=0.147ω_s, (a) with sweeping H_d to tune the control parameters (b) with sweeping L_g to investigate the system robustness

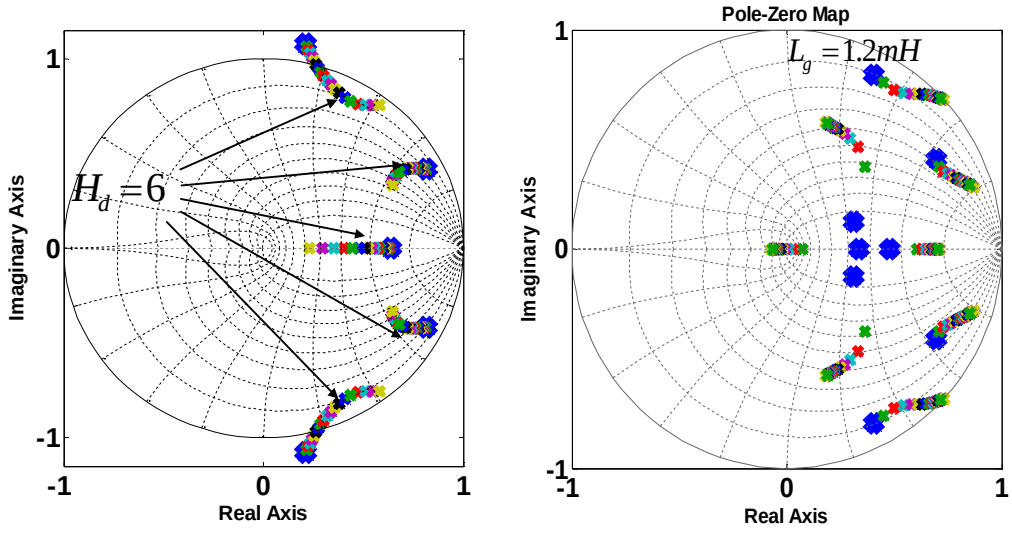

(a) (b)

Fig. 2.5. Pole map of $T_{closed\text{-}obs}$ (z) for ω_{res2}=0.195ω_s, (a) with sweeping H_d to tune the control parameters (b) with sweeping L_g to investigate the system robustness

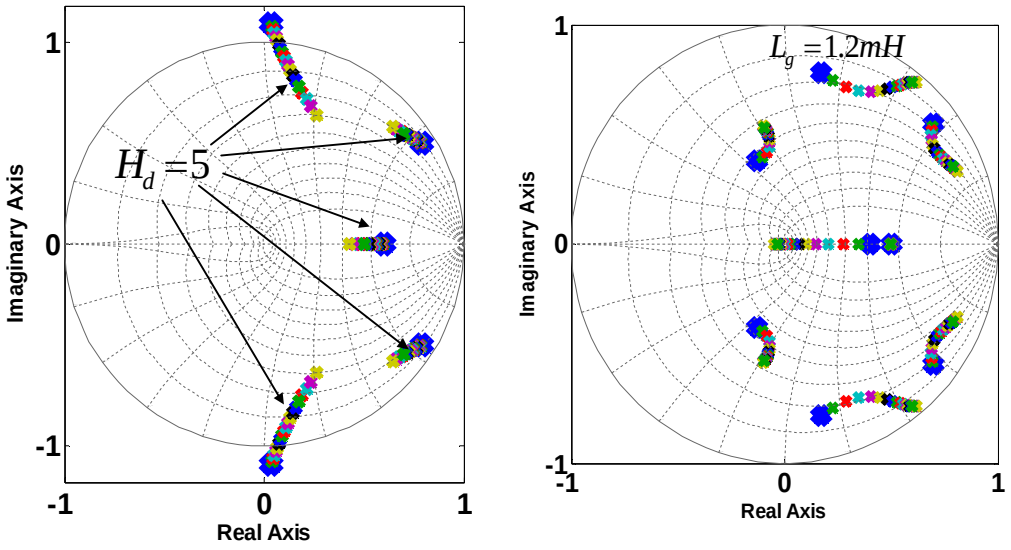

(a) (b)

Fig. 2.6. Pole map of $T_{closed\text{-}obs}$ (z) for ω_{res3}=0.23ω_s, (a) with sweeping H_d to tune the control parameters (b) with sweeping L_g to investigate the system robustness

It is shown from Figs. 2.4(b), 2.5(b) and 2.6(b) that two of the closed loop poles are moving toward the unit circle limit with increasing the grid inductance value. Although the system is still stable in the considered range of grid inductance variation, but, at higher values of the grid inductance, the system may become unstable.

2.5 Simulation & Experimental Results

To verify the behavior of the proposed algorithm, simulation and experimental work are carried out in two cases; using capacitor current sensor and using the proposed observer loop. To verify the dynamic response, the rms value of the reference current (I_{ref}) is stepped up from 2 Arms to 4 Arms (rated value) during these tests.

The simulation work is carried out in PSIM environment. Discrete models for the observer loop and the PR controller are constructed using PSIM digital control modules. For experimental verification, a single phase inverter prototype has been constructed

and connected through an LCL filter to an AC source to emulate the utility grid. The controller was implemented on a Texas Instruments TMS320C6713 DSP.

Figs. 2.7 and 2.8 show the simulation and experimental waveforms of the grid voltage and the grid current for the two considered cases; using capacitor current sensor and observer loop, respectively.

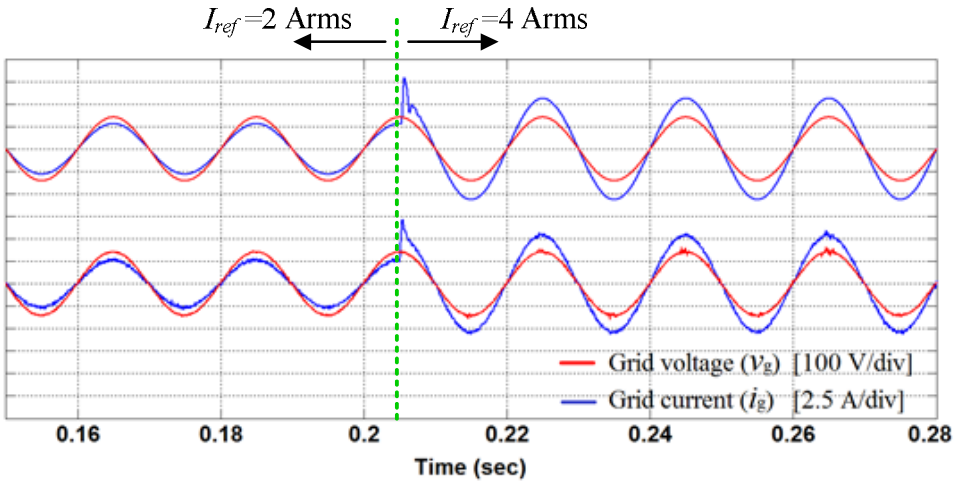

Fig. 2.7. Results with using current sensor for ω_{res2} = 0.195ω_s , upper waveforms (simulation), lower waveforms (experimental).

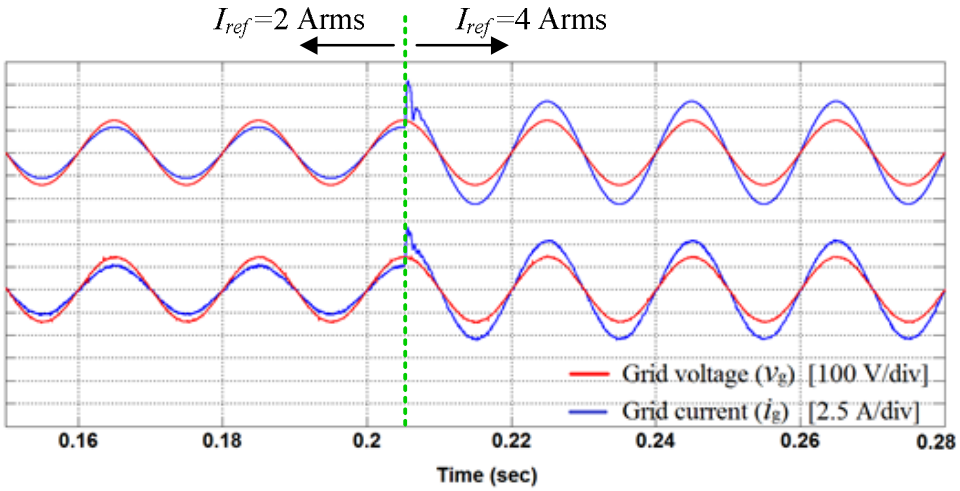

Fig. 2.8. Results with using the proposed observer loop for ω_{res2} = 0.195ω_s, upper waveforms (simulation), lower waveforms (experimental)

Both the simulation and experimental waveforms indicate that the proposed active damping algorithm can damp the resonance oscillations without the need for additional current sensors. For the experimental waveforms, it is shown that the steady state grid current contains some ripples in the sensor-based case. On the other hand, such high frequency switching ripples are largely attenuated with the observer-based case. This is due to the limited bandwidth of the observer. This represents another practical merit for replacing the current sensor by the observer.

2.6 Summary

An active damping algorithm based on the capacitor current estimation is investigated in this chapter. An observer in the control loop to is employed to estimate the capacitor current value without the need for additional current sensor. The observer poles are selected to be faster than the plant poles. This in turn, facilitates a separate design for the fundamental current regulator along with the active damping coefficient to meet pre-specified values of cross over frequency and damping behavior. The robustness of the closed loop stability is investigated against grid inductance variation; it is indicated that the stability get worse as the grid inductance increases. The simulation and the experimental results are introduced to verify the performance of the observer based active damping algorithm. These results show that the observer-based system offer a good damping behavior without the need for additional sensors. Moreover, compared to sensor-based system, it offers lower switching ripples.

Chapter 3:

A Two State Feedback Active Damping Strategy for the LCL Filter Resonance

3.1 Introduction

A novel active damping strategy for the *LCL* filter resonance is propose in this chapter. The proposed strategy uses two feedback loops of the grid current and the capacitor voltage. The proposed strategy is derived in the continuous time domain with a discussion for its discrete implementation. According to the proposed strategy, excitation of unstable open loop poles, which results in non-minimum phase behavior, can be avoided over wide range of resonant frequencies. Moreover, straightforward co-design procedures for both the fundamental current regulator and the active damping loops are proposed. A numerical example along with experimental results are introduced to validate the proposed strategy performance over wide range of resonant frequencies.

3.2 Proposed Active Damping Strategy

3.2.1 System Description

Fig. 3.1 shows a single phase inverter connected to the grid through an *LCL* filter. The block diagram of the capacitor-current-based active damping system is shown in Fig. 3.2, where a proportional feedback (H_d) of the capacitor current is used to actively damp the filter resonance.

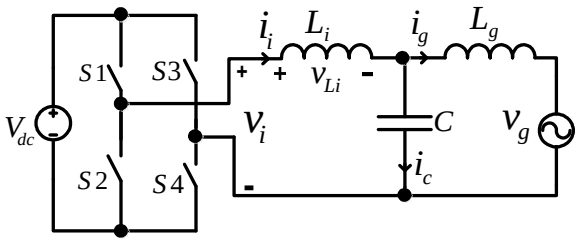

Fig. 3.1. Single phase inverter connected to the utility grid through an *LCL* filter.

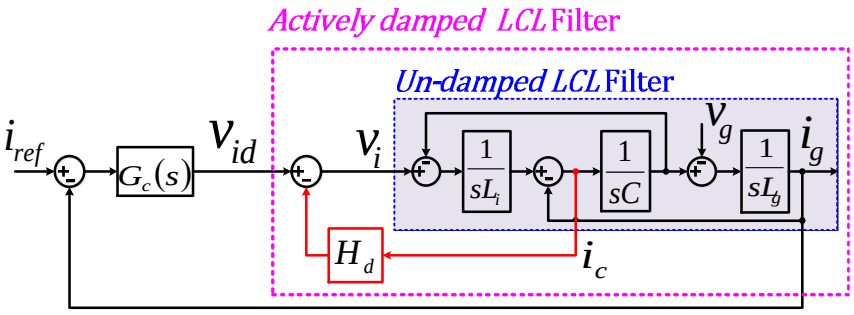

Fig. 3.2. Block diagram of capacitor-current-based active damping.

The un-damped filter transfer function $G_{ig}(s)$ and the filter resonant frequency ω_{res} are re-written in (3.1) and (3.2), respectively.

$$G_{ig}(s) = \frac{i_g(s)}{v_i(s)} = \frac{1}{L_i L_g C s(s^2+\omega_{res}^2)} \tag{3.1}$$

$$\omega_{res} = \sqrt{(L_i + L_g)/(C L_i L_g)} \tag{3.2}$$

A proportional-resonant (PR) controller with a transfer function of $G_c(s)$ is employed for fundamental current regulation. It is expressed in (3.3) with $\omega_o = 2\pi f_o$ where ω_o and f_o are the fundamental grid frequency in rad/sec and Hz, respectively.

$$G_c(s) = K_p + \frac{K_r S}{S^2+\omega_o^2} \tag{3.3}$$

According to Fig. 3.2, the transfer function of the capacitor-current-based actively damped filter can be expressed in (3.4) as $F_{ad}(s)$.

$$F_{ad}(s) = \frac{i_g(s)}{v_{id}(s)} = \frac{1}{C L_g L_i S\left(S^2+\frac{H_d}{L_i}S+\omega_{res}^2\right)} \tag{3.4}$$

In Figs. 3.3(a) till 3.3(d), the capacitor-current-based active damping system is manipulated using signal flow graph manipulation. In Fig. 3.3(a), the capacitor current is replaced by the difference between the inverter output current and the grid injected current.

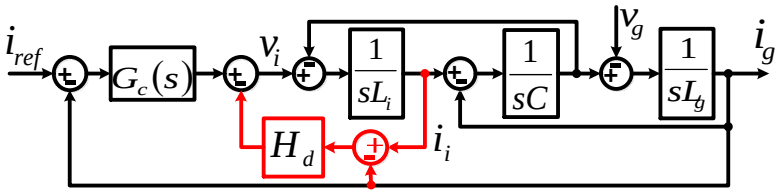

(a)

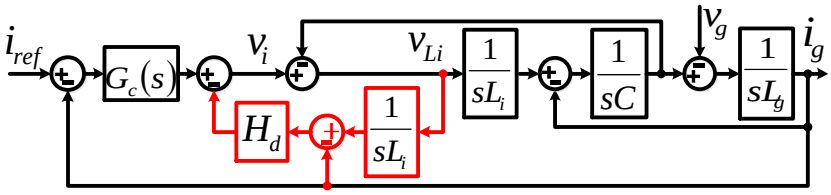

(b)

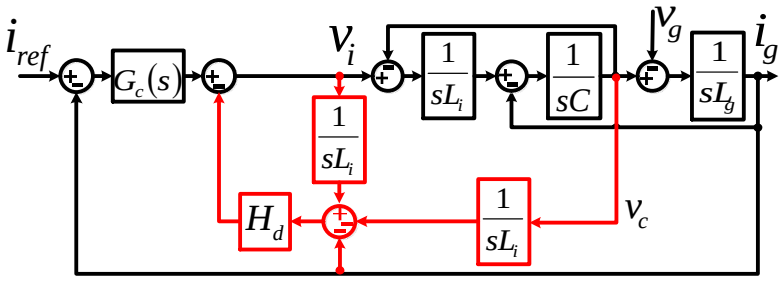

(c)

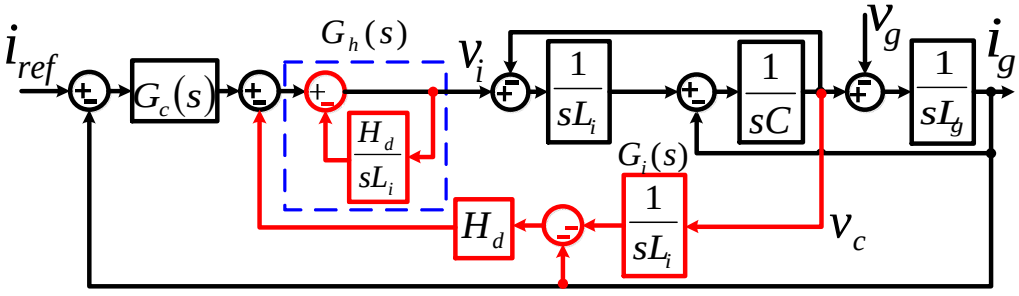

(d)

Fig. 3.3. Manipulation of the capacitor-current-based active damping technique.

With further manipulation, it is shown in Fig. 3.3(c) that the capacitor current feedback is equivalent to multiplying the active damping coefficient (H_d) with three feedback loops of:

- A unity feedback of the grid current (i_g)
- An integrator of the capacitor voltage (v_c) with a time constant of L_i.
- An integrator of the output inverter voltage (v_i) with a time constant of L_i.

By further manipulation, the modulated inverter voltage feedback loop is augmented in the main loop as a high-pass filter (HPF), with a cut off frequency of $\omega_h = H_d/L_i$. This HPF is denoted as $G_h(s)$ and expressed in (3.5). This system is shown in Fig. 3.3(d).

$$G_h(s) = \frac{1}{\omega_h} \cdot \frac{s}{1+s/\omega_h} \tag{3.5}$$

The typical rang for ω_h can be calculated by expressing the transfer function of the actively damped filter (F_{ad}), expressed in (3.4), in terms of ω_h and writing it in a standard form as in (3.6).

$$F_{ad}(s) = \frac{1}{CL_gL_iS(S^2+\omega_hS+\omega_{res}^2)} = \frac{1}{CL_gL_iS(S^2+2\zeta\omega_{res}S+\omega_{res}^2)} \tag{3.6}$$

Since the damping ratio ζ is typically around 0.7 [28], then a range of $0.5<\zeta<1$ will be considered; therefore, the typical range for ω_h can be determined as in (3.7).

$$\omega_{res} < \omega_h < 2\omega_{res} \tag{3.7}$$

Note that the integrator of the capacitor voltage feedback in Fig. 3.3(d). is denoted as $G_i(s)$.

The presence of the HPF (G_h) in cascade with the main control loop can decline both the system disturbance rejection and reference tracking capabilities. More modifications should be done to cope with these issues.

3.2.2 Proposed Active Damping System

The proposed system is derived in two steps as follow:

Step 1

To maintain the damping effect of the cascaded block $G_h(s)$ without deterioration of other control objectives, $G_h(s)$ is eliminated from the main control loop and only inserted into the active damping feedback loop to keep its damping effect. With multiplying $G_h(s)$ by H_d, the resulted transfer function, $G_{ad}(s)$ expressed in (3.8), is still a HPF with a gain of L_i.

$$G_{ad}(s) = \frac{sL_i}{1+s/\omega_h} \tag{3.8}$$

This system is shown in Fig. 3.4. Then, the new actively damped filter transfer function is expressed as $F_{new}(s)$ in (3.9)

$$F_{new}(s) = \frac{G_{ig}(s)}{1-G_{ad}(s)G_{ig}(s)\left(1+sL_gG_i(s)\right)} = \frac{(1+s/\omega_h)}{s^2\left(\frac{CL_iL_g}{\omega_h}s^2+CL_iL_gs+\frac{(L_i+L_g)}{\omega_h}\right)} \tag{3.9}$$

The s^2 term in the denominator of $F_{new}(s)$ results in a constant phase of -180° in the open loop bode plot. This in turn, can dramatically deteriorate the phase margin. As a result, more modifications are necessary.

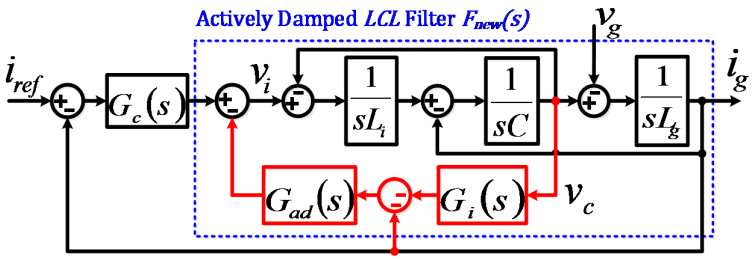

Fig. 3.4. Block diagram of the proposed active damping strategy.

Step 2

Both the gain of $G_{ad}(s)$ and the time constant of $G_i(s)$ are expressed in terms of a new variable (K_d) as in (3.10) and (3.11), respectively.

$$G_{ad}(s) = \frac{(K_d - L_g)s}{1 + s/\omega_h} \tag{3.10}$$

$$G_i(s) = \frac{1}{(K_d - L_g)s} \tag{3.11}$$

Substituting (3.10) and (3.11) into (3.9), $F_{new}(s)$ is re-written as in (3.12).

$$F_{new} = \frac{(1+s/\omega_h)}{CL_iL_gs(s^2+\omega_{res}^2)(1+s/\omega_h) - sK_d} = \frac{(1+s/\omega_h)}{\frac{CL_iL_g}{\omega_h}s^4 + CL_iL_gs^3 + \frac{L_i+L_g}{\omega_h}s^2 + (L_i+L_g-K_d)s} \tag{3.12}$$

Using Routh's criteria, K_d has to follow the constraint in (3.13) to guarantee the open loop system stability and hence minimum phase behavior.

$$0 < K_d < (L_i + L_g) \tag{3.13}$$

To generalize the following analysis, K_d is expressed in terms of the above maximum limit $(L_i + L_g)$ as in (3.14), where $0 < \beta_d < 1$ for a stable open loop system.

$$K_d = \beta_d (L_i + L_g) \tag{3.14}$$

Substituting (3.14) into (3.12), the actively damped filter of the proposed system is finally expressed in (3.15).

$$F_{new}(s) = \frac{(1+s/\omega_h)}{CL_iL_gs(s^2+\omega_{res}^2)(1+s/\omega_h) - s\beta_d(L_i+L_g)} \tag{3.15}$$

3.3 Discret Implementation of the Proposed System

3.3.1 System Discretization

The discrete representation of the proposed active damping strategy is shown in Fig. 3.5 where the DSP delay is represented by one sample delay. Using Tustin approximation with pre-warping at the fundamental frequency, the discrete PR regulator is determined in (3.16) where T_s is the sampling period.

$$G_c(z) = K_p + K_r \frac{sin(\omega_o T_s)}{2\omega_o} \frac{z^2-1}{(z^2 - 2z\,cos(\omega_o T_s)+1)} \tag{3.16}$$

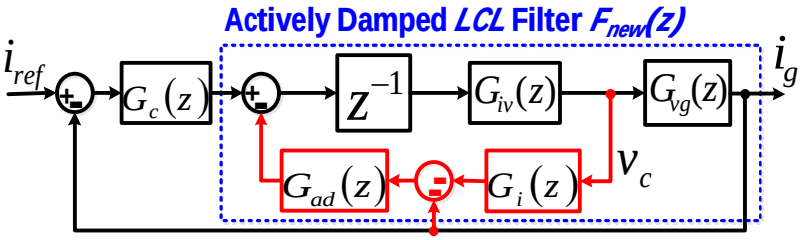

Fig. 3.5. Discrete representation of the proposed system.

In addition to G_{ig}(s), expressed in (3.1), two other transfer functions should be defined for system discretization:

- G_{iv}(s), expressed in (3.17), is the transfer function relating the modulated inverter voltage to the filter capacitor voltage.

$$G_{iv}(s) = \frac{1}{CL_i(s^2+\omega_{res}^2)} \tag{3.17}$$

- G_{vg}(s), expressed in (3.18), is the transfer function relating the filter capacitor voltage to the grid current.

$$G_{vg}(s) = \frac{1}{sL_g} \tag{3.18}$$

Using Zero-Order-Hold (ZOH) discretization, G_{ig}(z) and G_{iv}(z) are expressed as (3.19) and (3.20), respectively. G_{vg}(z) is determined as G_{ig}(z)/G_{iv}(z).

$$G_{ig}(z) = \frac{T_s}{(L_i+L_g)}\left(\frac{(1-\alpha)z^2-2(cos(\delta)-\beta)z+(1-\alpha)}{(z-1)(z^2-2z\,cos(\delta)+1)}\right) \tag{3.19}$$

$$G_{iv}(z) = \frac{1}{L_iC\omega_{res}^2}\frac{(1-cos(\delta))(1+z)}{(z^2-2z\,cos(\delta)+1)} \tag{3.20}$$

where $\delta = \omega_{res}T_s$ and $\alpha = \frac{sin(\omega_{res}T_s)}{\omega_{res}T_s}$

For the active damping loops, G_i(z) and G_{ad}(z) are determined using Tustin approximation and expressed in (3.21) and (3.22), respectively.

$$G_i(z) = \frac{T_s}{2(K_d-L_g)}\frac{z+1}{z-1} \tag{3.21}$$

$$G_{ad}(z) = K_{ad}\frac{z-1}{z+\omega_{ad}} \tag{3.22}$$

where $K_{ad} = \frac{2\omega_h(\beta_d(L_i+L_g)-L_g)}{\omega_h T_s+2}$ and $\omega_{ad} = \frac{\omega_h T_s-2}{\omega_h T_s+2}$

Finally, the discrete actively damped filter and the loop transfer function are expressed in (3.23) and (3.24), respectively.

$$F_{new}(z) = \frac{z^{-1}G_{ig}(z)}{1-z^{-1}G_{ig}(z)G_{ad}(z)(1+G_i(z)/G_{vg}(z))} \tag{3.23}$$

$$T_{loop}(z) = G_c(z)F_{new}(z) \tag{3.24}$$

3.3.2 Control Parameters Design

For tuning purpose, the equivalent *s*-domain representation, shown in Fig. 3.6, is used. As demonstrated in chapter 1, the DSP delay can be modelled by an exponential transfer function of:

$$G_d(s) = e^{-1.5sT_s} \tag{3.25}$$

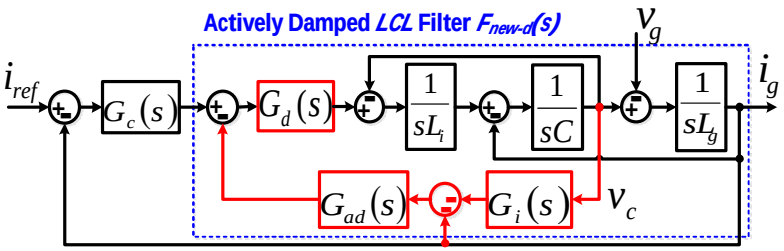

Fig. 3.6. *s*-domain representation for the proposed system discrete implementation.

According to this representation, both the actively damped filter transfer function ($F_{new\text{-}d}$) and the loop transfer function ($T_{loop\text{-}d}$) can expressed in (3.26) and (3.27), respectively.

$$F_{new-d}(s) = \frac{(1+s/\omega_h)G_d(s)}{CL_iL_gs(s^2+\omega_{res}^2)(1+s/\omega_h)-s\beta_d(L_i+L_g)G_d(s)} \tag{3.26}$$

$$T_{loop-d}(s) = G_c(s)F_{new-d}(s) \tag{3.27}$$

At the resonant frequency, the gain of $F_{new\text{-}d}$ can be approximated as in (3.28).

$$|F_{new-d}(j\omega_{res})| \cong \left|\frac{(1+j\omega_{res}/\omega_h)}{-j\omega_{res}\beta_d\,(L_i+L_g)}\right| \tag{3.28}$$

According to (3.28), higher values of ω_h should be adopted to acquire better damping effect. Theoretically, for discrete implementation, ω_h can be extended up to $0.5\omega_s$ (Nyquist sampling theory, where ω_s is the control frequency in rad/sec). However, such high value can deteriorate the discretization process. A value of ω_h $=0.4\omega_s$ is adopted here.

Since the resonant gain of the PR regulator is mainly effective at the fundamental frequency, the PR controller can be approximated as (3.29)

$$G_c(j\omega) = \begin{cases} K_p & for \quad \omega > \omega_o \\ K_r & for \quad \omega = \omega_o \end{cases} \tag{3.29}$$

At the crossover frequency (ω_c), which should be sufficiently higher than ω_o and below both ω_{res} and the adopted ω_h ($0.4\omega_s$), the loop gain can be approximated as (3.30).

$$T_{loop-d}(j\omega_c) = \frac{K_p}{\omega_c(L_i + L_g)}\frac{e^{-j1.5T_s\omega_c}}{(1-\beta_d e^{-j1.5T_s\omega_c})}$$

$$\left|T_{loop-d}(j\omega_c)\right| = \frac{K_p}{\omega_c(L_i+L_g)}\left|\frac{1}{(1-\beta_d e^{-j1.5T_s\omega_c})}\right| = 1 \tag{3.30}$$

Using Trigonometry, this gain is reduced to (3.31).

$$\left|T_{loop-d}(j\omega_c)\right| = \frac{K_p}{\omega_c(L_i+L_g)}\left|\frac{1}{A_c e^{j\theta_c}}\right| = \frac{K_p}{\omega_c(L_i+L_g)A_c} = 1 \tag{3.31}$$

where

$$A_c = \sqrt{1 + \beta_d^2 - 2\beta_d^2\cos(1.5T_s\omega_c)}$$

$$\theta_c = \sin^{-1}\frac{\beta_d \sin(1.5T_s\omega_c)}{A_c} \tag{3.32}$$

Hence, for certain value of β_d, K_p should be calculated as in (3.33) to obtain certain crossover frequency.

$$K_p = \omega_c(L_i + L_g)A_c \tag{3.33}$$

Substituting (3.32) into (3.24), the loop transfer function is expressed in (3.34)

$$T_{loop}(z) = A_c\omega_c(L_i + L_g)F_{new}(z) \tag{3.34}$$

At the fundamental frequency, the loop gain can be approximated as in (3.35).

$$\left|T_{loop-d}(j\omega_o)\right| = \frac{K_r}{\omega_o(L_i+L_g)A_o} \tag{3.35}$$

where $A_o = \sqrt{1 + \beta_d^2 - 2\beta_d^2\cos(1.5T_s\omega_o)}$

This is expressed in dB in (3.36) from which K_r can be determined from (3.37) for certain fundamental loop gain (T_{fo}).

$$T_{fo} = 20\log_{10}\frac{K_r}{\omega_o(L_i+L_g)A_o} \tag{3.36}$$

$$K_r = \omega_o(L_i + L_g)A_o \cdot 10^{\frac{T_{fo}}{20}} \tag{3.37}$$

Using the above-derived expressions, the following steps are proposed to co-design the control system parameters.

1. Plot the pole-map of $F_{new}(z)$, expressed in (3.23), by sweeping β_d. Select β_d so that it corresponds to the farthest resonant poles inside the unit circle to achieve the best damping.
2. For a certain value of the fundamental loop gain (T_{fo}) along with the selected value for β_d, use (3.37) to determine K_r.
3. For a certain value of the crossover frequency (ω_c) along with the selected value of β_d, use (3.33) to determine K_p.
4. Plot a bode diagram for the loop transfer function expressed in (3.24). Check the resonant peak. If the resonant peak is more than 0 dB, then decrease the pre-specified crossover frequency (ω_c) and repeat steps 3 and 4.

   These steps are organized in the flowchart shown in Fig. 3.7.

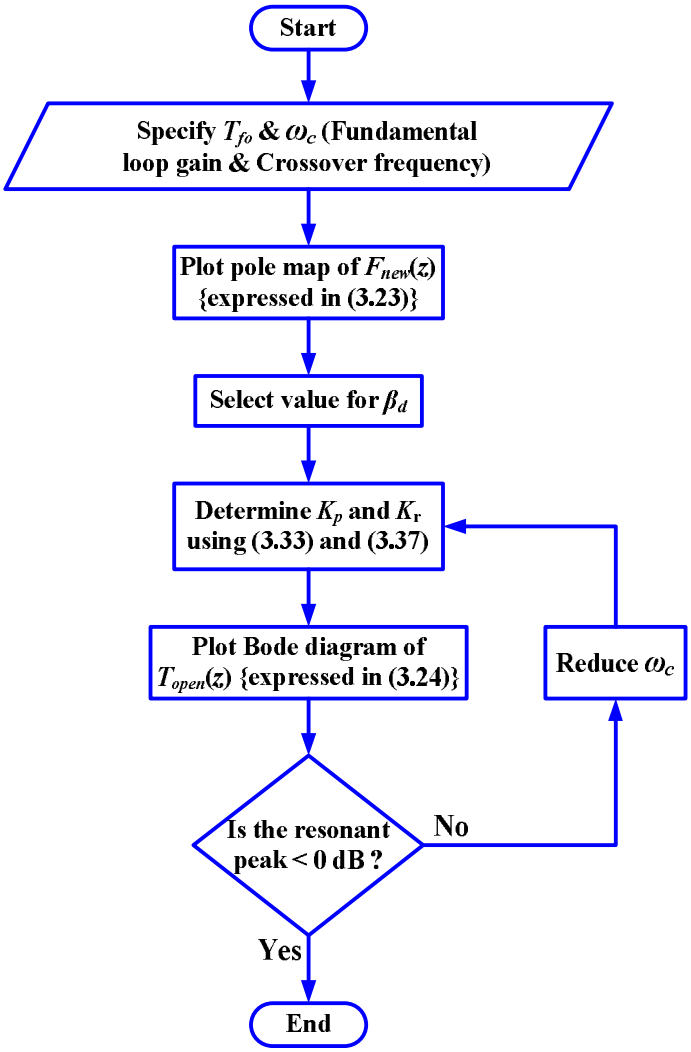

Fig. 3.7 Flowchart of the co-design steps for the control parameters of the proposed active damping strategy

3.4 Numerical Verification

3.4.1 Numerical Example

Table 3.1 lists the parameter values of the grid-connected inverter shown in Fig. 3.1. Four capacitance values, corresponding to resonant frequencies of $0.143\omega_s$, $0.179\omega_s$, $0.209\omega_s$ and $0.241\omega_s$ are used to verify the performance of the proposed system over wide range of resonant frequencies with respect to the control frequency. These resonant frequencies are denoted as ω_{res1}, ω_{res2}, ω_{res3} and ω_{res4}, respectively.

The HPF cut off frequency (ω_h) value is taken as $0.4\omega_s$ to mitigate the resonant peak as much as possible. In addition, a value of 60 dB is adopted for the fundamental loop gain (T_{fo}). Finally, an initial value for the crossover frequency of 0.3 of each corresponding resonant frequency is adopted.

Using the tuning steps presented in the last section, a pole-map of $F_{new}(z)$ is plotted with variation of β_d. These pole-maps are plotted in Figs. 3.8(a), 3.9(a), 3.10(a) and 3.11(a) for the resonant frequencies ω_{res1}, ω_{res2}, ω_{res3} and ω_{res4}, respectively. To achieve the best damping effect, the values of β_d corresponding to the farthest resonant poles inside the unit circle are selected. These values are determined as 0.55, 0.45, 0.3 and 0.15 for ω_{res1}, ω_{res2}, ω_{res3} and ω_{res4}, respectively. Using the selected values of β_d along with the pre-specified values of ω_c and T_{fo}, the corresponding values of K_p and K_r are determined from (3.33) and (3.37), respectively.

For ω_{res1} and ω_{res2}, Figs. 3.8(b) and 3.9(b) show bode plots of the loop transfer function, expressed in (3.24), respectively. It is shown that the resonance peak is less than 0 dB.

Table 3.1
System Parameters

Symbol	Quantity	Value
P	Rated power	400 W
V_g	Grid voltage	100 V
F_o	Grid Frequency	50 Hz
V_{dc}	DC Voltage	200 V
L_i	Inverter side inductance	1.85 mH
L_g	Grid side inductance	1.3 mH
C	Capacitance	16.3 µF, 10.4 µF, 7.6 µF, 5.7 µF
f_{sw}	Switching Frequency	10 kHz
f_s	Sampling Frequency	10 kHz

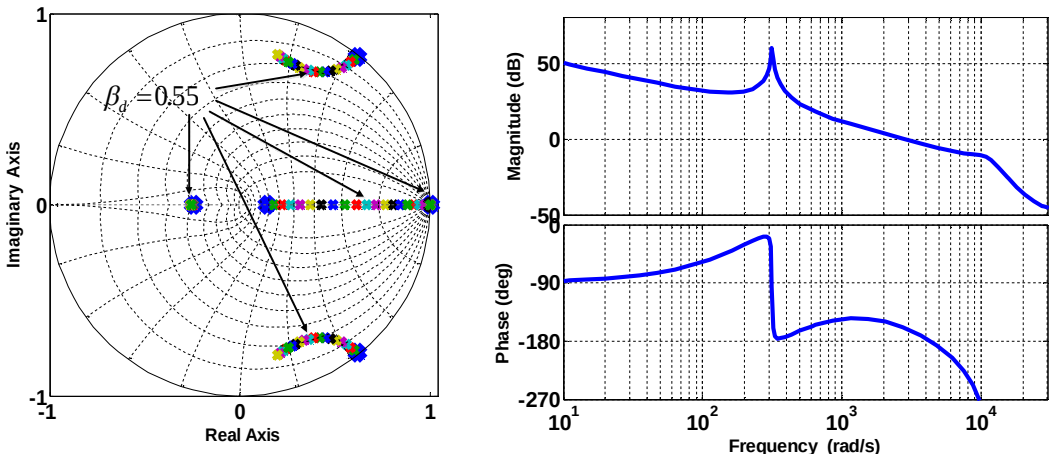

(a) (b)

Fig. 3.8: (a) pole-map of $F_{new}(z)$ for $\omega_{res1}=0.143\omega_s$ with sweeping β_d (b) corresponding bode plot for T_{loop} at β_d =0.55

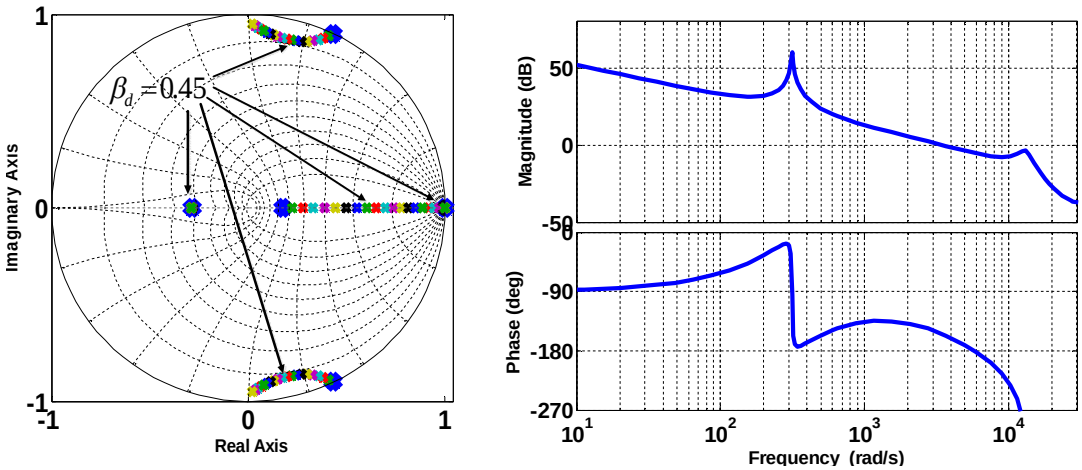

(a) (b)

Fig. 3.9: (a) pole-map of $F_{new}(z)$ for ω_{re2} =0.179ω_s with sweeping β_d, (b) corresponding bode plot for T_{loop} at β_d =0.45

For ω_{res3} and ω_{res4}, it is found that the frequency response exhibits a resonant peak of more than of 0 dB. To overcome this issue, a reduction in the crossover frequency has to be adopted. For ω_{res3}, it is found that a reduction of the crossover frequency of $0.12\omega_{res3}$ can reduce the resonant peak to less than 0 dB However, for ω_{res4}, a large crossover frequency reduction is required to obtain a resonant peak of less than 0 dB. Such a reduction can deteriorate the system dynamic performance. Moreover, the phase lag introduced by the PR controller at low frequencies dramatically reduces the phase

margin. Therefore, only a reduction of the crossover frequency to $0.1\omega_{res4}$ is adopted. Figs. 3.10(b) and 3.11(b) show the frequency responses for ω_{res3} and ω_{res4}, respectively.

Table 3.2 summaries the designed control parameters and the achieved performance of the phase margin (PM), ω_c and T_{fo}. These results indicate the well damped performance of the proposed method over a wide range of resonant frequencies while meeting the pre-specified values of ω_c and T_{fo}.

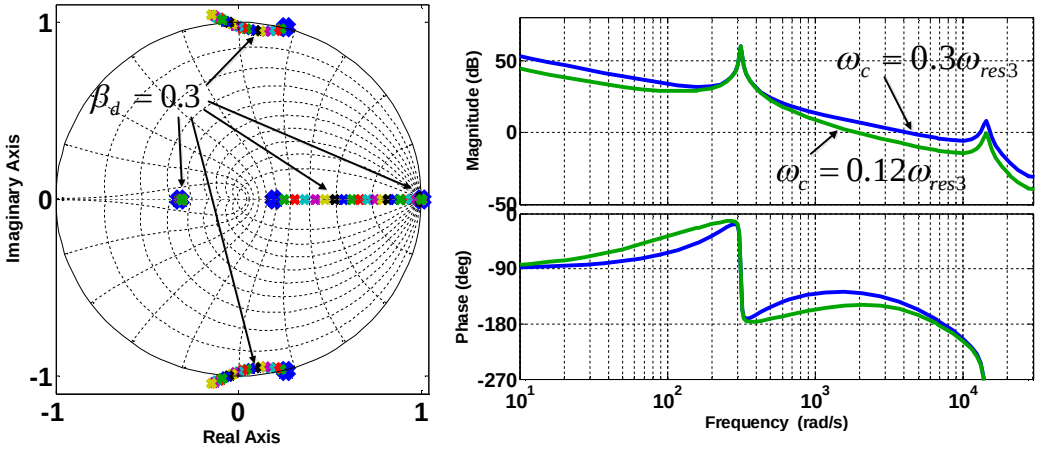

(a) (b)

Fig. 3.10: (a) pole-map of $F_{new}(z)$ for ω_{re3} =0.209ω_s with sweeping β_d, (b) corresponding bode plot for T_{loop} at β_d =0.3 and different crossover frequencies

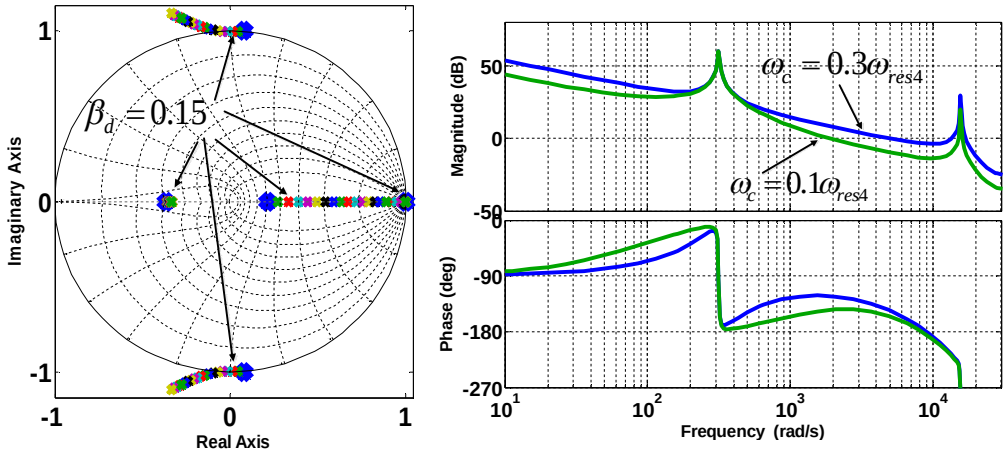

(a) (b)

Fig. 3.11: (a) pole-map of $F_{new}(z)$ for ω_{res4}=0.241ωs with sweeping β_d, (b) corresponding bode plot for T_{loop} at β_d =0.15 and different crossover frequencies

Table 3.2
Designed Control Parameters & Frequency Response Results

C (µF)	Assumed ω_c (rad/sec)	Designed Parameters			Achieved frequency response		
		β_d	K_r	K_p	ω_c (rad/sec)	PM (degree)	T_{fo} (dB)
16.3	$0.3\omega_{res1}$	0.55	446	4.57	$0.32\omega_{res1}$	19.9	60.1
10.4	$0.3\omega_{res2}$	0.45	545	6.83	$0.31\omega_{res2}$	25.2	60.1
7.6	$0.3\omega_{res3}$	0.3	693	9.54	$0.32\omega_{res3}$	31.2	60.1
	$0.12\omega_{res3}$			3.53	$0.14\omega_{res3}$	31.5	60
5.7	$0.3\omega_{res4}$	0.15	841	12.73	$0.32\omega_{res4}$	35.2	60.1
	$0.1\omega_{res4}$			4.08	$0.12\omega_{res4}$	35.1	60

3.4.2 Robustness against Grid Inductance Variations

In real operation, the grid side inductance (L_g) may vary significantly. To investigate system robustness against such variations, the pole-maps of the closed loop system T_{closed}, expressed in (3.38), are plotted in Fig. 3.12 while sweeping L_g between 100-300% of its original value.

$$T_{closed}(z) = \frac{T_{loop}(z)}{1+T_{loop}(z)} \tag{3.38}$$

For the considered resonant frequencies, it is shown from the above pole-map plots that the closed loop poles move inside the unit circle with an increasing L_g. These plots reflect the system robustness against grid inductance variations.

3.5 Comparative Study

To show the superiority of the proposed active damping method compared to the existing capacitor voltage-based and current-based AD methods, the limitations of these methods are clarified under the same parameters used in the aforementioned numerical example as follow.

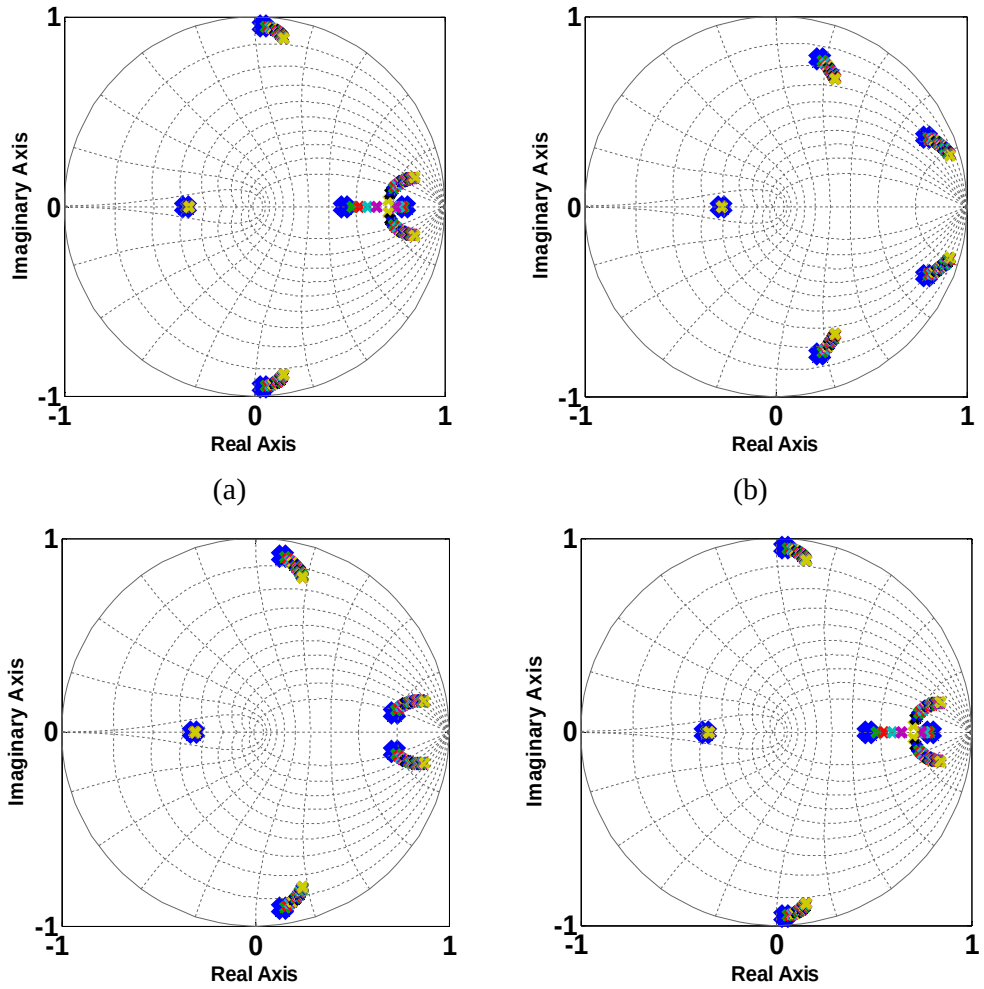

Fig. 3.12. Closed loop pole-maps with grid inductance (L_g) variation for (a) ω_{res1}=0.143ω_s, (b) ω_{res2}=0.179ω_s, (c) ω_{res3}=0.201ω_s, (d) ω_{res4}=0.241ω_s

3.5.1 Capacitor-Voltage-Based AD Method Limitation:

Fig. 3.13 shows the discrete representation of the capacitor-voltage-based AD method, where a lead-lag network of $G_{ad\text{-}v}(z)$ is used for damping purpose. The *s*-domain counterpart of this network is expressed as $G_{ad\text{-}v}(s)$ in (3.39). Using Fig. 3.13, the discrete loop transfer function can be expressed as (3.40).

$$G_{ad-v}(s) = K_d C \omega_{res} \frac{s+K_f\omega_{res}}{K_f s+\omega_{res}} \tag{3.39}$$

$$T_{open-v}(z) = \frac{z^{-1}G_c(z)G_{iv}(z)G_{vg}(z)}{1+z^{-1}G_{ad-v}(z)G_{iv}(z)} \tag{3.40}$$

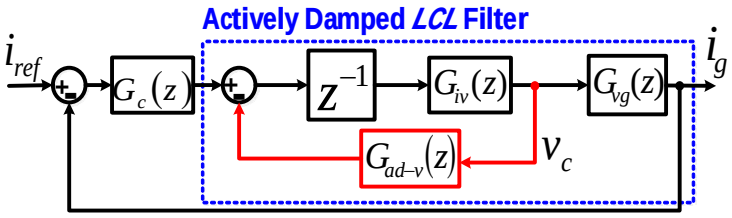

Fig. 3.13. Block representation of capacitor-voltage-based AD method.

It was shown in [112] that this method can behave effectively over the limited range of resonant frequencies between 1/3.2 and 1/3.4 of the sampling frequency (ω_s). To emphasize the difficulty of using this method outside these specified limits, the AD loop design procedures presented in [112] are used for the resonant frequencies ω_{res1} and ω_{res2} ($<\omega_s/3.2$); these procedures are shown in Fig. 3.14.

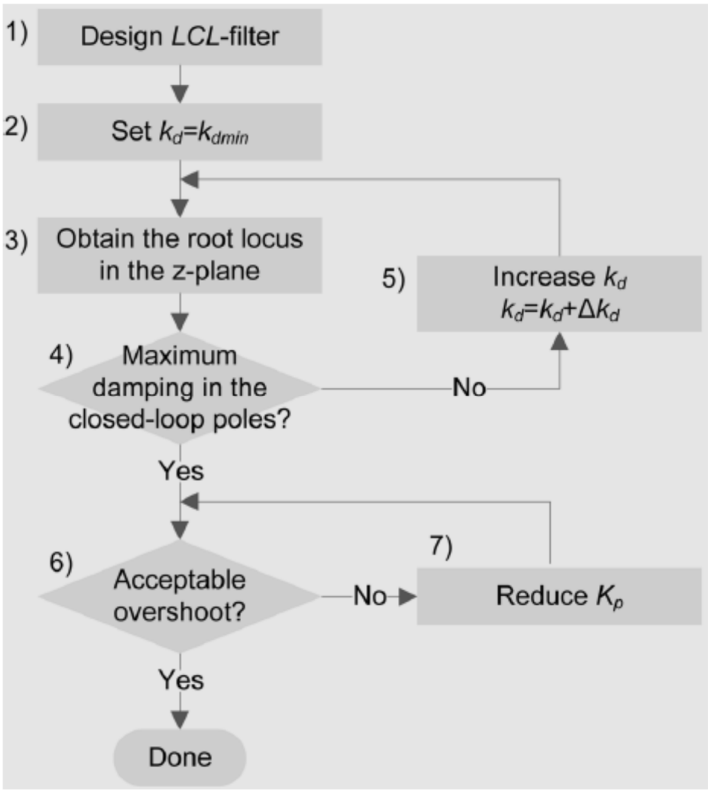

Fig. 3.14 Design steps for capacitor voltage based AD method [112].

Firstly, the value of K_f is determined using (3.41) to achieve a maximum network angle (φ_{max}) of 75 degree at a frequency of $\omega_{max} = \omega_{res}$. Then, the minimum value of K_d is determined as $\left(K_{dmin} = L_g/3T_s\right)$.

$$K_f = \sqrt{\frac{1-\sin\varphi_{max}}{1+\sin\varphi_{max}}} \tag{3.41}$$

Following this, the root locus of the closed loop system, expressed in (3.42), is plotted while sweeping K_d (starting from K_{dmin}) as shown in Figs. 3.15(a) and 3.15(b) for the resonant frequencies ω_{res1} and ω_{res2}, respectively.

$$T_{closed-v}(z) = \frac{T_{open-v}(z)}{1+T_{open-v}(z)} \tag{3.42}$$

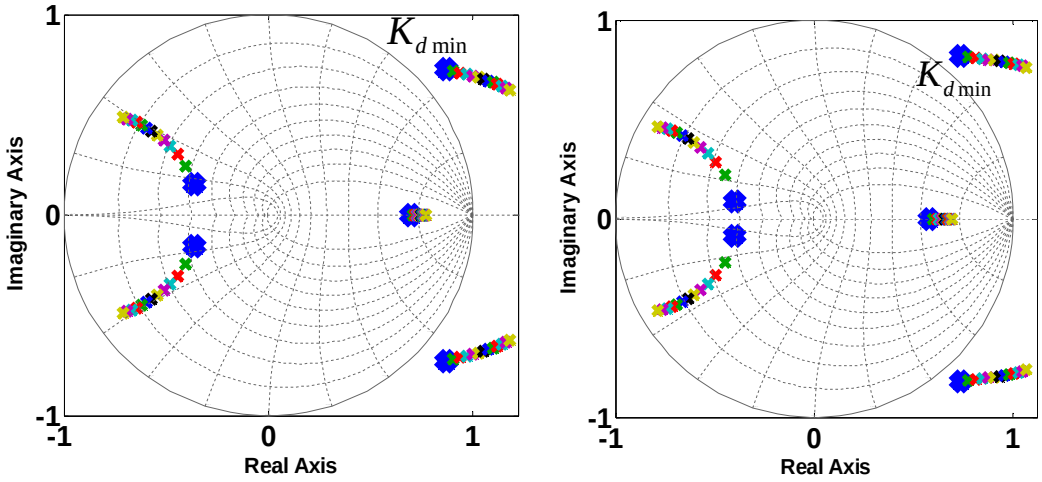

Fig. 3.15. Closed loop pole-map using capacitor-voltage-based AD method with sweeping K_d, a) for ω_{res1}=0.143ω_s (K_p=8.47), b) for ω_{res2}=0.179ω_s (K_p=10.6).

It is shown in these plots that the system cannot be stable for any values of K_d. This ensures the difficulty of using this method for resonant frequencies outside specific limits. On the other hand, the proposed method behaves effectively over a wide range of resonant frequencies as verified in the above numerical example.

3.5.2 Capacitor-Current-Based AD Method Limitation:

The discrete representation of the capacitor-current-based AD method is shown Fig. 3.16. For analysis purpose, the filter transfer function is divided into two functions as follow;

- $G_{ic}(s)$, expressed in (3.43), is the transfer function relating the modulated inverter voltage to the filter capacitor current.

$$G_{ic}(s) = \frac{s}{L_i(s^2+\omega_{res}^2)} \tag{3.43}$$

- $G_{cg}(s)$, expressed in (3.44), is the transfer function relating the filter capacitor current to the grid current.

$$G_{cg}(s) = \frac{1}{cL_g s^2} \tag{3.44}$$

ZOH discretization for $G_{ic}(s)$ is used to determine $G_{ic}(z)$ as expressed in (3.45). On the other hand, $G_{cg}(z)$ is expressed in (3.46) from dividing $G_{ig}(z)$, expressed in (3.19), by $G_{ic}(z)$.

$$G_{ic}(z) = \frac{sin(\omega_r T_s)}{\omega_r L_i} \frac{z^{-1}(1-z^{-1})}{(1-2z^{-1}\,cos(\omega_r T_s)+z^{-2})} \tag{3.45}$$

$$G_{cg}(z) = \frac{G_{ig}(z)}{G_{ic}(z)} \tag{3.46}$$

Using the above expressions, the closed loop transfer function is expressed as $T_{closed\text{-}c}$ in (3.47).

$$T_{closed-c}(z) = \frac{z^{-1}G_{ig}(z)G_c(z)}{1+z^{-1}G_{ic}(z)(G_c(z)G_{cg}(z)+H_d)} \tag{3.47}$$

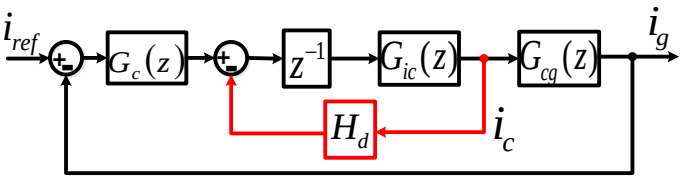

Fig. 3.16. Discrete representation of capacitor-current-based AD method

In addition to its need for a high cost current sensor or a complicated observer loop to measure or estimate the capacitor current, it was shown in [96] and [99] that non-minimum phase behavior in the capacitor-current-based active damping method cannot be avoided for resonant frequencies of more than one-sixth of the sampling frequency, which implies an ineffective active damping [97]. Moreover, it was demonstrated in [96] and [99] that closed loop systems can hardly be stable at resonant frequency equal to one-sixth of the sampling frequency. This value of the resonant frequency can likely be reached due to grid inductance variations, which in turn implies a weak robustness.

To emphasize the above-mentioned limitations, the capacitor-current-based AD method is used with the resonant frequencies ω_{res2} and ω_{res3} ($>\omega_s/6$). To verify the system robustness, the pole-maps of $T_{closed\text{-}c}$ is plotted while sweeping L_g between 100-300% of its original value. These plots are shown in Figs. 3.17(a) and 3.17(b) for ω_{res2} and ω_{res3}, respectively. (The control parameters are determined using the procedures presented in [13] and listed in below the corresponding plots).

It is shown that the closed loop poles are very close to the unit circle. This in turn, demonstrates the ineffective damping performance of this method for resonant frequencies of more than one-sixth of the sampling frequency. Moreover, as shown in the zoomed part, the system stability violates around a certain value of the grid inductance corresponding to a resonant frequency of one-sixth of the sampling frequency.

On the other hand, it has been shown that avoiding such non-minimum behavior and high robustness against grid inductance variations can be achieved over a wide range of resonant frequencies using the proposed AD method.

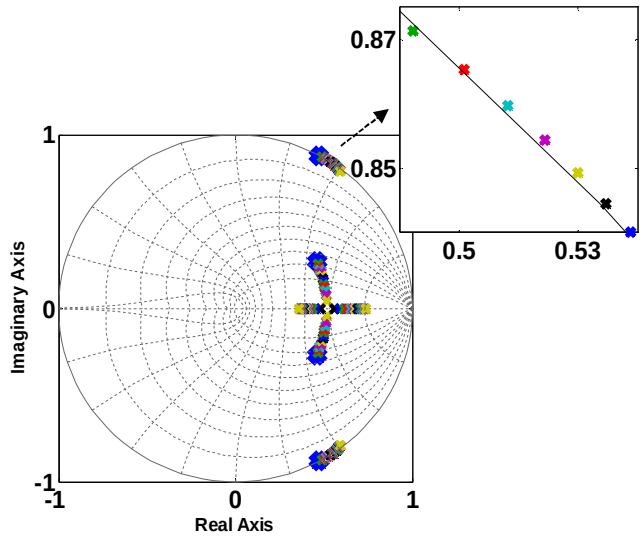

(a)

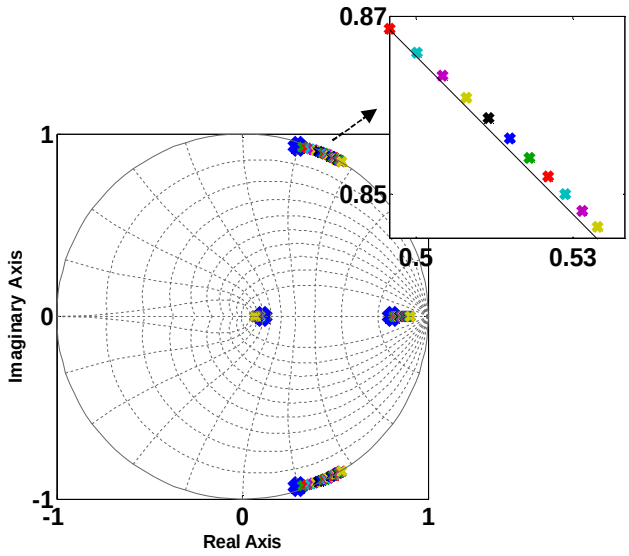

(b)

Fig. 3.17 Closed loop pole-map of capacitor-current-based AD method with sweeping L_g, a) for ω_{res2} (K_p=10.6, H_d=5) , b) for ω_{res3} (K_p=4.96, H_d=1).

3.6 Experimental Work

Using the system parameters listed in Table 3.1, a single phase inverter prototype has been built and connected through an *LCL* filter to an AC power supply to emulate the utility grid. The control algorithm has been implemented using the PE-Expert3

platform, which consists of a C6713-A DSP development board along with a high-speed PEV board for analog-to-digital conversion and PWM signal generation.

To verify the dynamic response, the rms value of the reference current (I_{ref}) is stepped up from 2 Arms to 4 Arms (rated value). Using the designed parameters listed in Table 3.2, the experimental tests are carried out with and without the proposed active damping method.

For ω_{res1}, which is lower than one-sixth of the sampling frequency, the system cannot be stabilized without active damping (AD). Thus, removing the active damping loop for this case causes a high oscillatory current as shown in Fig. 3.18(a). On the other hand, Fig. 3.18(b) shows the stabilization effect of active damping loops.

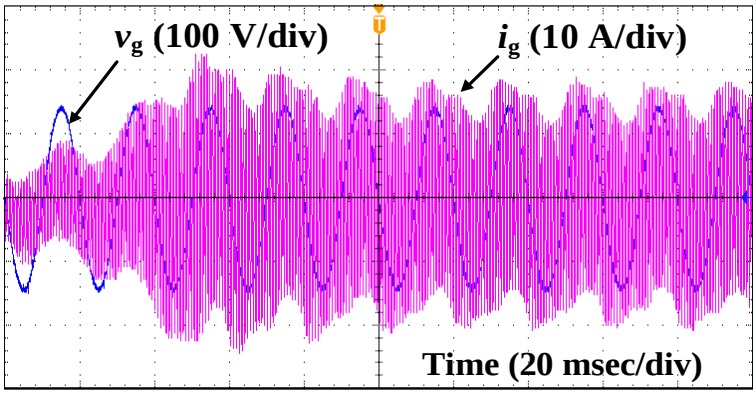

(a)

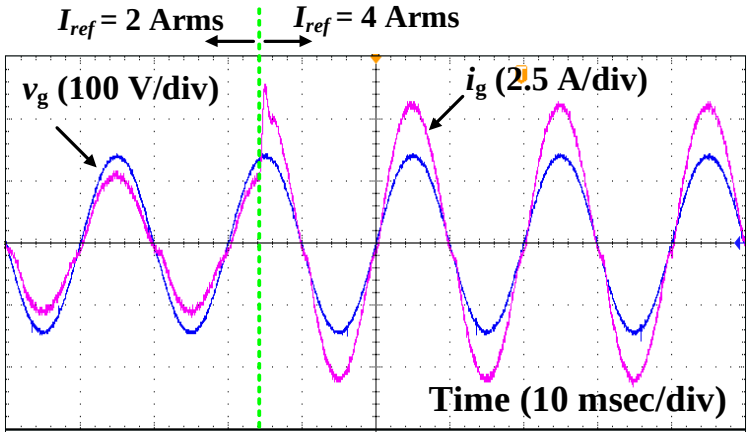

(b)

Fig. 3.18 Experimental waveforms of grid current (i_g) and grid voltage (v_g) for ω_{res1} =0.143ω_s (a) without AD, (b) with AD.

For ω_{res2}, ω_{res3} and ω_{res4}, the system can be stabilized without active damping as shown in Figs. 3.19(a), 3.20(a) and 3.21(a). However, it can recognize the dynamic oscillations which are caused by weak damping (there is some damping introduced by the small resistance of the coils). Figs. 3.19(b), 3.20(b) and 3.21(b) show the waveforms when using the proposed active damping loops. The mitigation of the dynamic oscillations can be recognized when using the proposed active damping method.

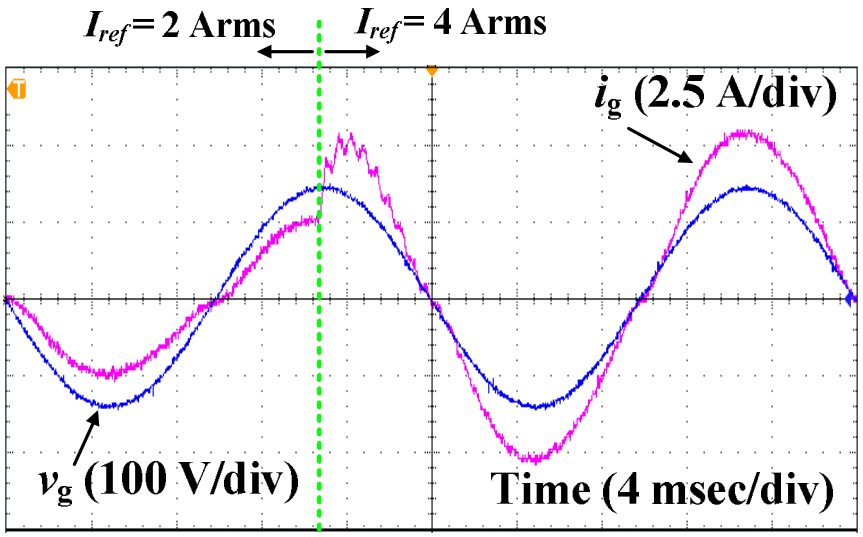

(a)

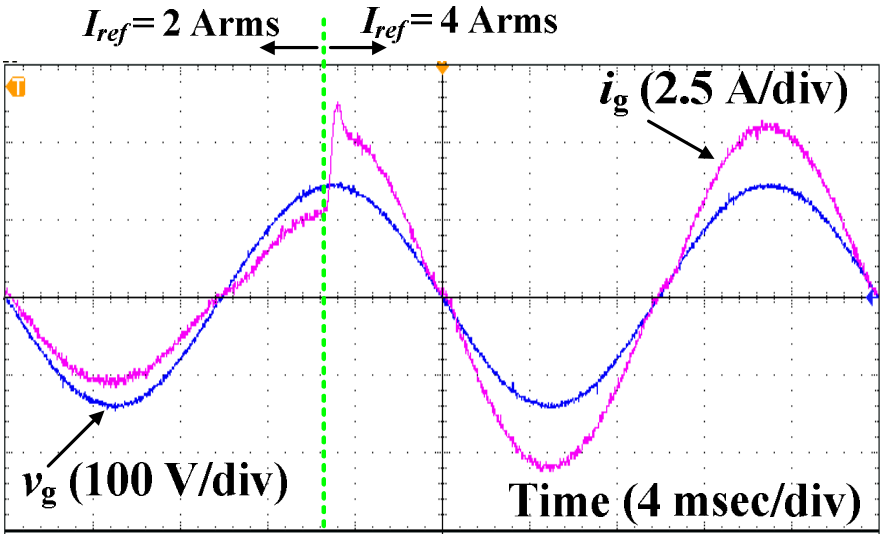

(b)

Fig. 3.19 Experimental waveforms of grid current (i_g) and grid voltage (v_g) for ω_{res2} =0.179ω_s (a) without AD, (b) with AD.

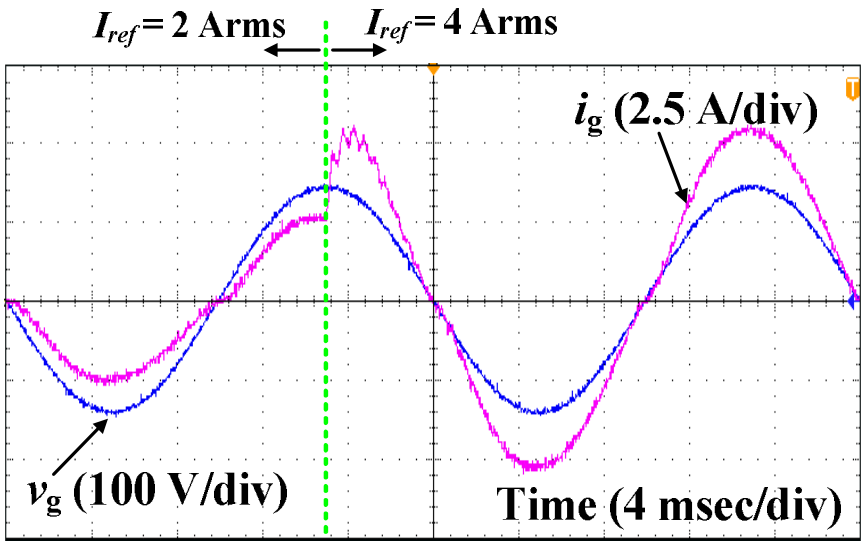

(a)

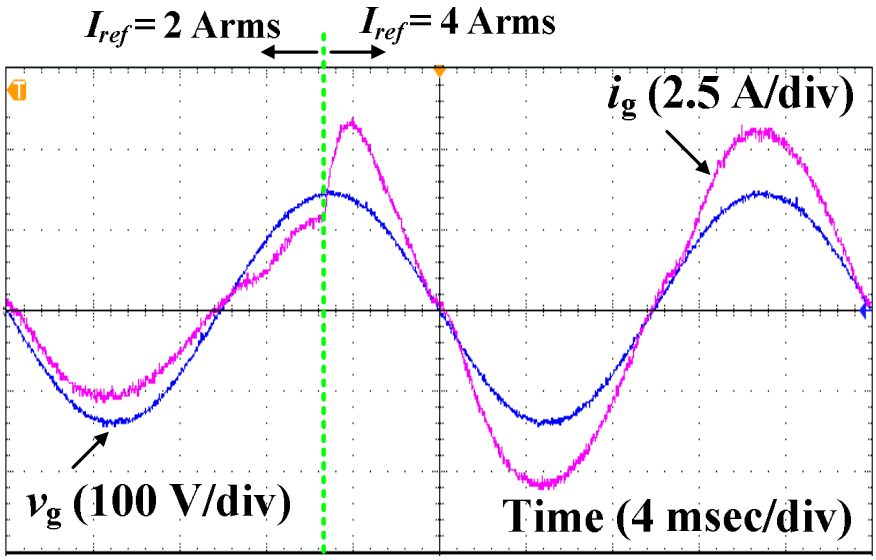

(b)

Fig. 3.20. Experimental waveforms of grid current (i_g) and grid voltage (v_g) for ω_{res3} =0.209ω_s (a) without AD, (b) with AD.

The resonance mitigation effect of the AD loop can be further clarified by plotting the spectrum of the grid current with and without the proposed active damping method. These spectrums are shown in Figs. 3.22, 3.23 and 3.24 at the resonant frequencies ω_{res2}, ω_{res3} and ω_{res4}, respectively.

Without using AD loop, it can be recognized from Figs. 3.22(a), 3.23(a) and 3.24(a) that there is a significant current harmonic component, denoted as i_{res}, with a frequency equal to the corresponding resonant frequency in each case. On the other hand, In Figs. 3.22(b), 3.23(b) and 3.24(b), it is shown that this resonance harmonic component is completely suppressed.

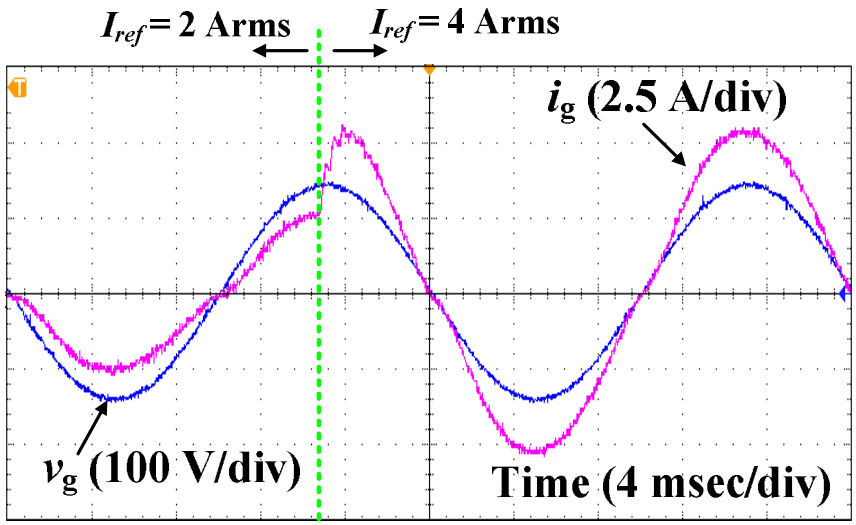

(a)

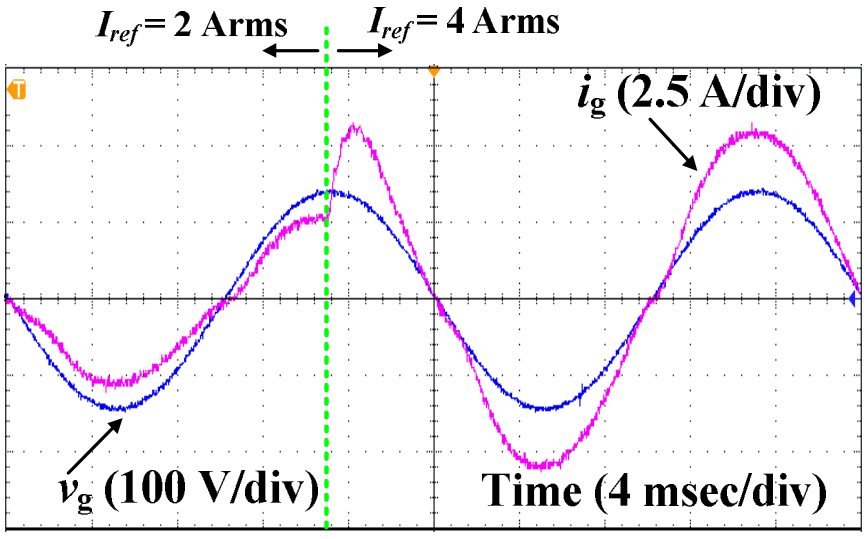

(b)

Fig. 3.21. Experimental waveforms of grid current (i_g) and grid voltage (v_g) for ω_{res4} =0.241ω_s (a) without AD, (b) with AD.

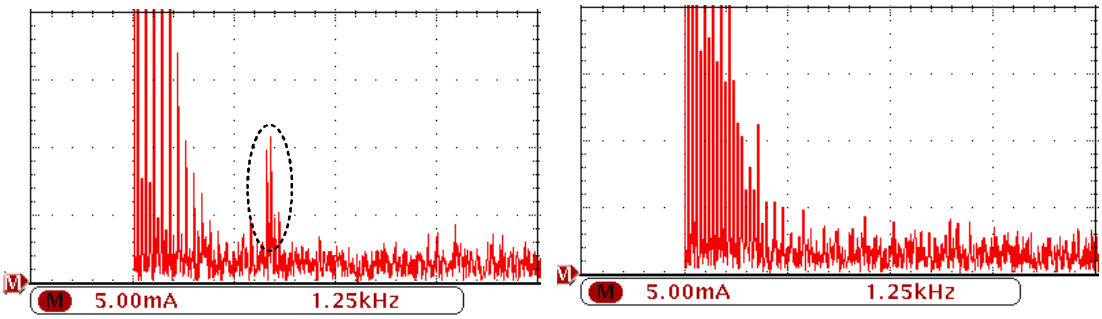

(a) (b)

Fig. 3.22. Spectrum of the grid current (i_g) for ω_{res2}=0.179ω_s (a) without active damping loops (b) with active damping loops

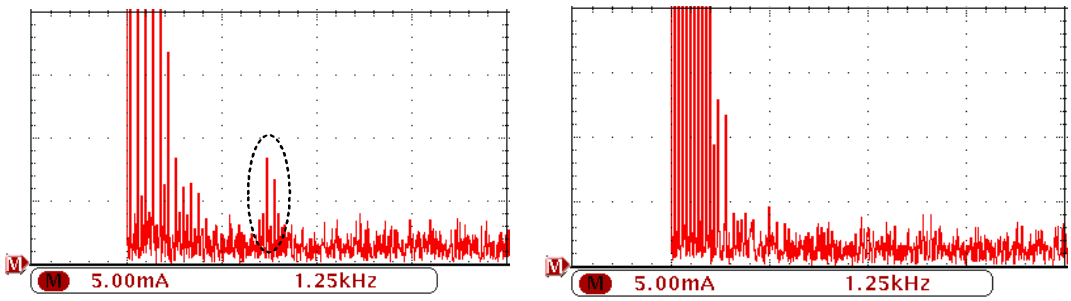

(a) (b)

Fig. 3.23. Spectrum of the grid current (i_g) for ω_{res3} =0.209ω_s (a) without active damping loops (b) with active damping loops

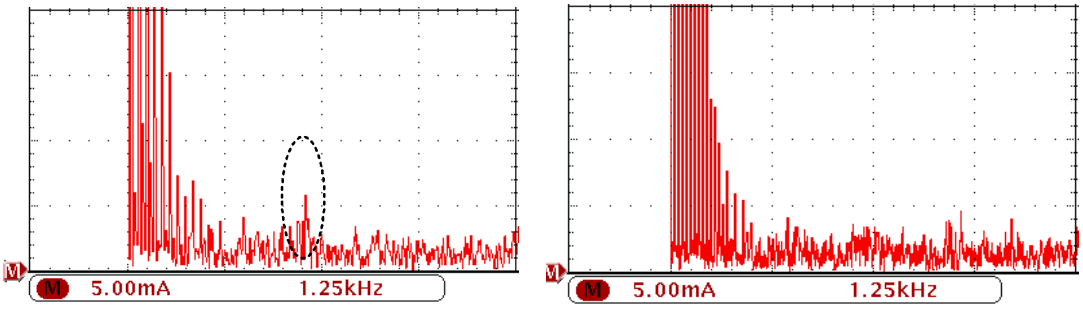

(a) (b)

Fig. 3.24. Spectrum of the grid current (i_g) for ω_{res4}=0.241ω_s (a) without active damping loops (b) with active damping loops

For experimental verification of its ineffective damping for resonant frequencies of more than one-sixth of the sampling frequency, the capacitor current based AD method has been used for the resonant frequency ω_{res2} (=0.179ω_s), and Fig. 2.25 shows the corresponding experimental waveforms. It can be seen that the resonant current

oscillations are still present in this case. On the other hand, the damping of the proposed AD method at the same resonant frequency has been clarified in Fig. 3.19(b).

The above-introduced results, along with the frequency response analysis introduced in the above numerical example, reflect satisfactory steady state and transient performances along with resonance damping over a wide range of resonant frequencies using the proposed active damping method and the control parameters tuning steps.

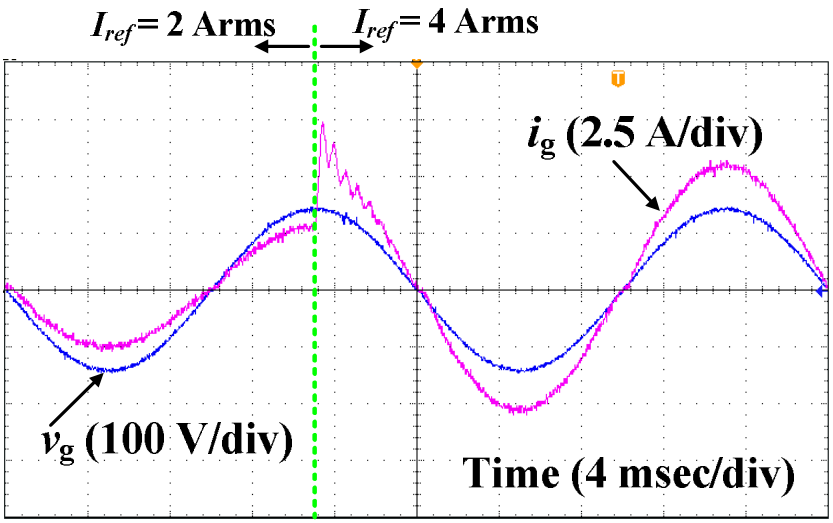

Fig. 3.25. Experimental waveforms of grid voltage (v_g) and grid current (i_g) using capacitor-current-based AD at ω_{res2} =0.179ω_s.

3.7 Summary

A novel active damping strategy using two feedback loops of the grid current and filter capacitor voltage is proposed in this chapter. Compared to the previous active damping methods, the proposed one can offer the following merits.

- Compared to the capacitor-current-based method, the cost can be reduced by omitting the high cost current sensor. Moreover, the non-minimum phase behavior can be avoided over a wide range of resonant frequencies.

- Compared to the capacitor-voltage-based method, the proposed strategy can behave effectively over a wide range of the resonant frequencies without stability violations.
- Compared to the grid current based method, a straightforward co-design method for the fundamental current regulator and the active damping loops are proposed.

A numerical example has been introduced to verify the performance of the proposed method over a wide range of resonant frequencies. To show the superiority of the proposed method, the drawbacks of the capacitor voltage/current based methods have been clarified. This example along and experimental results reflect the satisfactory performance of the proposed method.

Chapter 4:

Synthesis of Grid-Current-Based Active Damping for the *LCL* Filter Resonance

4.1 Introduction:

Compared to other active damping techniques, Grid-current-based active damping is more preferred where there is no need to additional sensors or complicated control algorithms. Ideally, this needs an s^2 term in the active damping loop [117]; however, it is not implemented practically due to the associated noise amplification. One approach to overcome this issue has been introduced in [117], [119] and [120] where the s^2 term is replaced by a high-pass filter (HPF). However, the following challenges can be identified when handling with this approach:

- Identifying the parametric influence of the HPF on the open loop system stability of the digitally controlled system at certain resonant frequency.
- Extending the resonant frequency range over which unstable open loop behavior can be avoided.
- Straightforward co-design steps for the HPF along with the fundamental current regulator to meet pre-specified behavior.

This chapter investigates active damping of grid-connected *LCL* filter resonance using HPF of the grid current. By extending the signal flow graph manipulation of the active damping method introduced in the previous chapter, a new expression for such HPF is derived in terms of the filter components. This expression facilitates a detailed

study for the actively damped filter behavior in discrete time domain. Limits for the HPF parameters are derived in order to avoid excitation of unstable open loop poles which, upon excitation, can worse the damping performance and the system robustness. Moreover, straightforward co-design steps for the HPF along with the fundamental current regulator are presented. To investigate the system performance, a numerical example at different resonant frequencies is introduced. Finally, the experimental work is presented.

4.2 Proposed HPF Form for Active Damping

The grid-connected single phase inverter considered in the previous chapter along with the block diagram of the proposed active damping system presented in the previous chapter are shown in Figs. 4.1 and 4.2, respectively. A proportional-resonant (PR) controller with a transfer function of $G_c(s)$ is employed for fundamental current regulation. It is expressed in (4.1) with $\omega_o = 2\pi f_o$ where ω_o and f_o are the fundamental grid frequency in rad/sec and Hz, respectively.

$$G_c(s) = K_p + \frac{K_r S}{S^2+\omega_o^2} \tag{4.1}$$

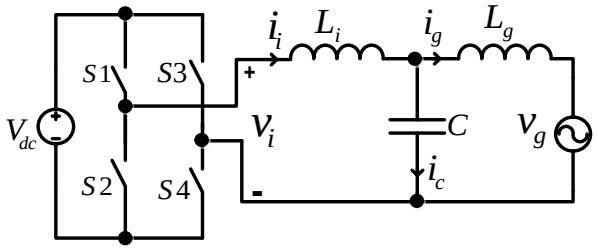

Fig. 4.1. A single phase inverter connected to the grid through an *LCL* filter.

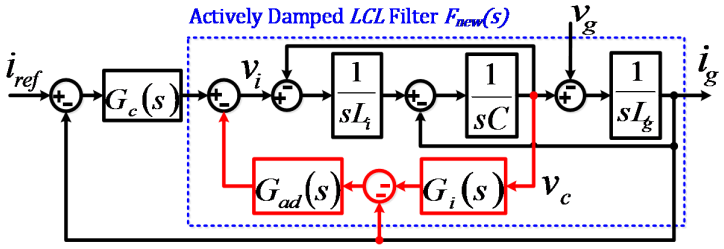

Fig. 4.2. Block diagram of the active damping strategy presented in chapter 2.

By further manipulation for the proposed active damping system presented in the previous chapter, the capacitor voltage feedback can be shifted towards the grid current to produce single feedback loop of the grid current with a transfer function of $G_{ad\text{-}g}(s)$; this transfer function is expressed in (4.2) where $\omega_h = H_d/L_i$. The manipulated system is shown in Fig. 4.3.

$$G_{ad-g}(s) = \frac{s\beta_d(L_i+L_g)}{1+s/\omega_h} \tag{4.2}$$

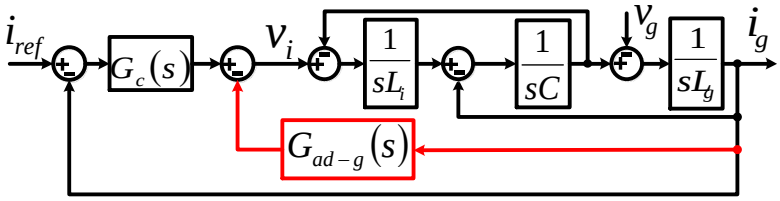

Fig. 4.3. System block diagram with a HPF of grid current.

Expressing the HPF gain in terms of the filter inductances helps to clarify the different system characteristics in terms of the filter parameters and in turn, makes the tuning steps simple and straightforward as indicated in the following sections.

4.3 Discussing the Effect of HPF Parameters

4.3.1 System Discretization

Fig. 4.4 shows the system discrete representation where the digital signal processor (DSP) delay is modeled by one sample delay. $G_{ig}(z)$ and $G_c(z)$ are the discrete transfer function the un-damped LCL filter and the PR controller. They have been determined in the previous chapter and are re-written here in (4.3) and (4.4) respectively. $G_{ad\text{-}g}(z)$ is determined using Tustin approximation and expressed in (4.5).

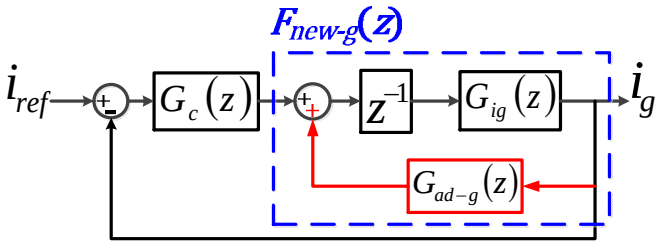

Fig. 4.4. Discrete representation of the grid-current-based AD system.

$$G_{ig}(z) = \frac{T_s}{(L_i+L_g)}\left(\frac{(1-\alpha)z^2-2(cos(\delta)-\alpha)z+(1-\alpha)}{(z-1)(z^2-2z\,cos(\delta)+1)}\right) \tag{4.3}$$

$$G_c(z) = K_p + K_r\frac{sin(\omega_o T_s)}{2\omega_o}\frac{z^2-1}{(z^2-2z\,cos(\omega_o T_s)+1)} \tag{4.4}$$

$$G_{ad-g}(z) = K_{ad}\frac{z-1}{z+\omega_{ad}} \tag{4.5}$$

where

$$\delta = \omega_{res}T_s, \qquad \alpha = \frac{sin(\omega_{res}T_s)}{\omega_{res}T_s},$$
$$K_{ad-g} = \frac{2\omega_h\beta_d(L_i+L_g)}{\omega_h T_s+2}, \qquad \omega_{ad} = \frac{\omega_h T_s - 2}{\omega_h T_s + 2} \tag{4.6}$$

and T_s denotes the sampling time.

To generalize the analyses, both ω_{res} and ω_h are expressed in terms of the sampling frequency (ω_s) as in (4.7). Then, the expressions in (4.6) are re-written in (4.8).

$$\omega_{res} = \beta_{res}\omega_s, \qquad \omega_h = \beta_h\omega_s \tag{4.7}$$

$$\delta = 2\pi\beta_{res}, \qquad \alpha = \frac{sin(2\pi\beta_{res})}{2\pi\beta_{res}},$$
$$K_{ad-g} = \frac{2\omega_s\beta_h\beta_d(L_i+L_g)}{2\pi\beta_h+2}, \qquad \omega_{ad} = \frac{2\pi\beta_h-2}{2\pi\beta_h+2} \tag{4.8}$$

Using (4.3), (4.5) and (4.7), the discrete model of the actively damped filter ($F_{new\text{-}g}(z)$) is expressed in (4.9).

$$F_{new-g}(z) = \frac{z^{-1}G_{ig}(z)}{1-z^{-1}G_{ad}(z)G_{ig}(z)} = \frac{T_s}{(L_i+L_g)}\cdot$$
$$\frac{(z+\omega_{ad})\left((1-\alpha)z^2-2(cos(\delta)-\alpha)z+(1-\alpha)\right)}{(z-1)\left[z(z+\omega_{ad})(z^2-2z\,cos(\delta)+1)-\frac{4\pi\beta_d\beta_h}{2\pi\beta_h+2}\left((1-\alpha)z^2-2(cos(\delta)-\alpha)z+(1-\alpha)\right)\right]} \tag{4.9}$$

Only the gain of $F_{new\text{-}g}(z)$ depends on the specific values of the sampling frequency and the filter inductances. On the other hand, zeros and poles of $F_{new\text{-}g}(z)$ do not depend on these specific values; they depend only on β_d (gain-multiplier of HPF), β_{res} (ratio of ω_{res} to ω_s) and β_h (ratio of ω_h to ω_s). From (4.9), $F_{new\text{-}g}(z)$ has one constant pole at z=1

and four other poles depend on β_d, β_{res} and β_h: two resonant poles at the resonant frequency of $F_{new\text{-}g}(z)$, and the other two poles will be called non-resonant poles.

Since the PR controller, expressed in (4.4), does not have unstable poles, the stability of the open loop system ($T_{open}(z) = G_c(z)F_{new-g}(z)$) is implied only by $F_{new\text{-}g}(z)$, and in turns, by β_d, β_{res} and β_h. In the next sections, detailed study is introduced to investigate the effect of β_d, β_{res} and β_h on the stability of $F_{new\text{-}g}(z)$.

4.3.2 Discussing the Effect of HPF Parameters

In Fig. 4.5, the pole-map of $F_{new\text{-}g}(z)$ is plotted by sweeping β_h from 0 to 0.5 (corresponding to ω_h equals Nyquist frequency) at constant value of β_d (β_d=1; corresponding to HPF gain of L_i+L_g) and three values of β_{res} (β_{res1}<β_{res2}<β_{res3}; corresponding to different resonant frequencies). The following remarks can be revealed from this plot:

1. Beside the constant pole at z=1, one of the non-resonant poles is also constant at z=1; the second non-resonant pole tracks entirely inside the unit circle for all values of β_{res} (its track direction is not shown to make the figure clear).

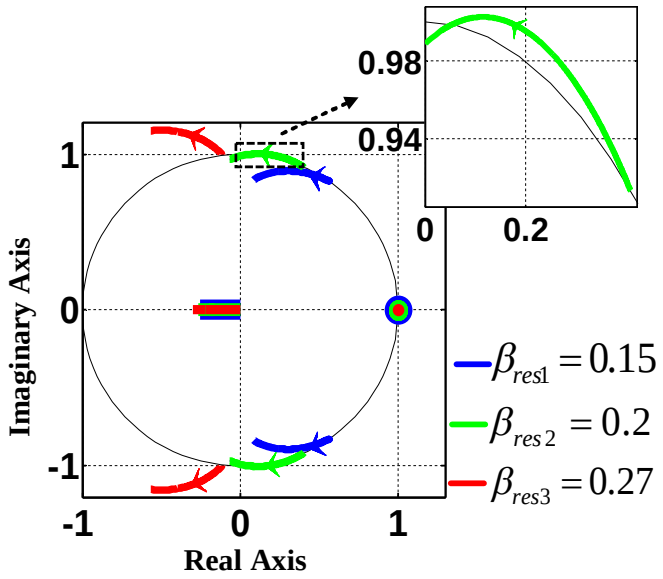

Fig. 4.5. Pole-maps of $F_{new\text{-}g}$ (z) with sweeping β_h (at β_d =1 and different β_{res}).

2. The tracks of the resonant poles start from some point on the unit circle (corresponding to undamped *LCL* filter). By increasing β_h, the resonant poles may track entirely inside the unit circle (as for β_{res1}), or it may track entirely outside the unit circle (as for β_{res3}), or it may initially track outside the unit circle before tracking inside the unit circle above certain value of β_h (as for β_{res2}).

From the second remark, it is expected that there is a maximum limit for β_{res} above which $F_{new\text{-}g}(z)$ is unstable in the range of β_h (<0.5). This maximum limit will be denoted as $\beta_{res\text{-}max}$ (corresponding to resonant frequency of $\omega_{res\text{-}max}$). At $\beta_{res\text{-}max}$, the tracks of the resonant poles should track outside the unit circle and end by intersection with the unit circle at β_h=0.5. Based on this understanding, $\beta_{res\text{-}max}$ can be determined by plotting the pole-map of $F_{new\text{-}g}(z)$ with sweeping β_{res} at constant value of β_h=0.5.

To investigate the effect of HPF gain variation, this pole-map is plotted for different values of β_d. Two regions of β_d are considered; ($0<\beta_d \leq 1$) and ($\beta_d <0$) as shown in Figs. 4.6 (a) and (b), respectively. In this plot, β_{res} is swept from 0.1 to 0.45. Theoretically, β_{res} can be extended to 0.5; however, due to the resonant frequency variation with discrete implementation, the resonant frequency should be adequately far from the vicinity of the Nyquist frequency [64]. ***From these figures, the following remarks can be revealed:***

1. ***For $0<\beta_d \leq 1$:*** in Fig. 4.6(a), the resonant poles track initially inside the unit circle before tracking outside the unit circle above certain value of $\beta_{res}=\beta_{res\text{-}max}$. It is observed that all the tracks of the resonant poles intersect with the unit circle at certain point corresponding to resonant poles denoted as $P_{1,2}$. Accordingly, for $0<\beta_d \leq 1$, $F_{new\text{-}g}(z)$ is stable only for resonant frequencies below certain value of $\omega_{res\text{-}max}$ ($=\beta_{res\text{-}max}\omega_s$).

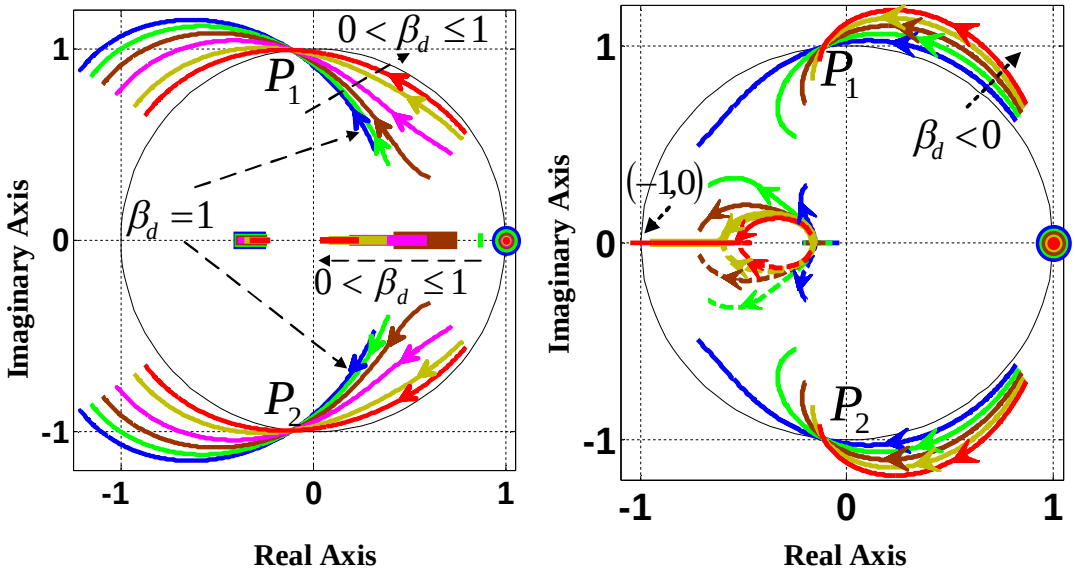

Fig. 4.6. Pole-maps of $F_{new\text{-}g}$ (z) with sweeping β_{res} at β_h=0.5 and different values of β_d. (a) $1 \geq r > 0$. (b) $r < 0$

2. ***For β_d <0:*** in Fig. 4.6(b), the resonant poles track initially outside the unit circle before tracking inside the unite circle above certain value of β_{res}; this value will be denoted as $\beta_{res\text{-}min}$. Furthermore, it is observed that all the tracks of the resonant poles intersect with the unit circle at the same point corresponding to resonant poles $P_{1,2}$. For low values of β_d in this region and with increasing β_{res} above $\beta_{res\text{-}min}$, one of the non-resonant poles tracks outside the unit circle above -certain value of β_{res} corresponding to one of the non-resonant poles at (-1,0). This value will be denoted as $\beta_{res\text{-}high}$. Accordingly, for certain value of β_d <0, $F_{new\text{-}g}$(z) is stable only over certain range of resonant frequencies between $\omega_{res\text{-}min}$ (=$\beta_{res\text{-}min}\omega_s$) and $\omega_{res\text{-}high}$ (=$\beta_{res\text{-}high}\omega_s$). By decreasing β_d in this region, the range between $\beta_{res\text{-}min}$ and $\beta_{res\text{-}high}$ shrinks till it vanishes at certain β_d corresponding to $\beta_{res\text{-}min}$=$\beta_{res\text{-}high}$. This value of β_d will be denoted as $\beta_{d\text{-}b}$ with corresponding β_{res} denoted as $\beta_{res\text{-}b}$.

4.3.3 HPF Cutoff Frequency Variation at Different HPF Gains

For the two regions of r ($0<\beta_d \leq 1$ and $\beta_d<0$), the above analyses are respectively repeated in Figs. 4.7, 4.8 and 4.9 for three values of β_h of 0.4, 0.3 and 0.2, respectively. It is shown that, by decreasing β_h, the resonant poles $P_{1,2}$ move to the right on the unit circle. The performance in the two ranges of β_d is still the same: for $0<\beta_d\leq 1$, $F_{new\text{-}g}(z)$ is stable below certain value of $\beta_{res}= \beta_{res\text{-}max}$; for $\beta_d<0$, $F_{new\text{-}g}(z)$ is stable over certain range of $\beta_{res\text{-}min} <\beta_{res}< \beta_{res\text{-}high}$.

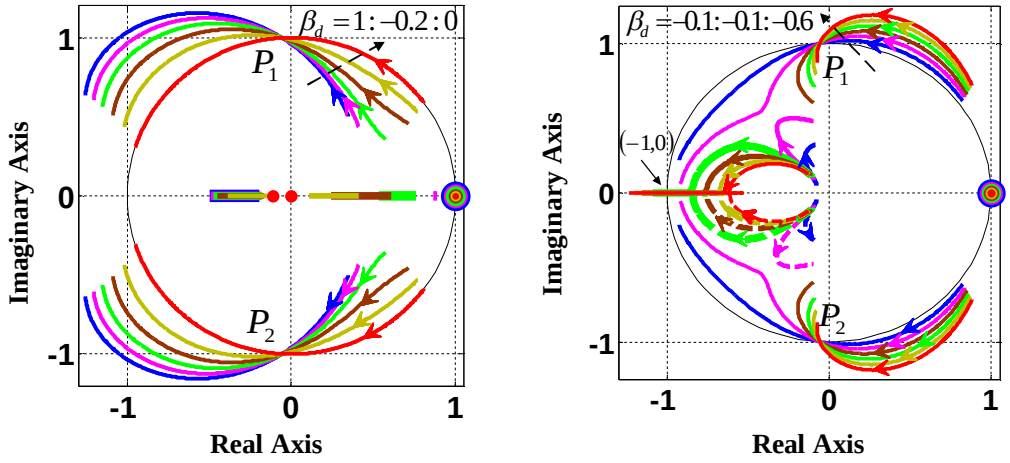

(a) (b)

Fig. 4.7. Pole-maps of $F_{new\text{-}g}$ (z) at β_h=0.4 with sweeping β_{res} for (a) $0<\beta_d\leq 1$, (b) $\beta_d<0$.

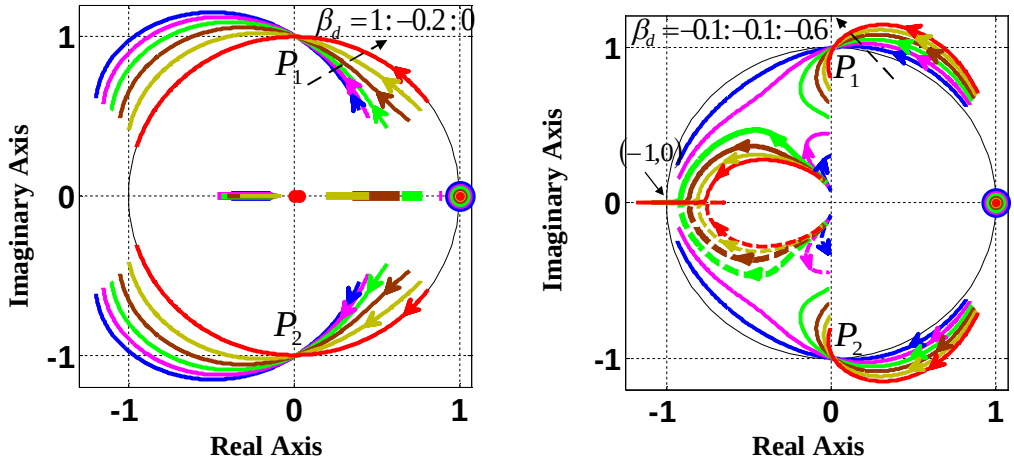

(a) (b)

Fig. 4.8. Pole-maps of $F_{new\text{-}g}$ (z) at β_h=0.3 with sweeping β_{res} for (a) $0<\beta_d\leq 1$, (b) $\beta_d<0$.

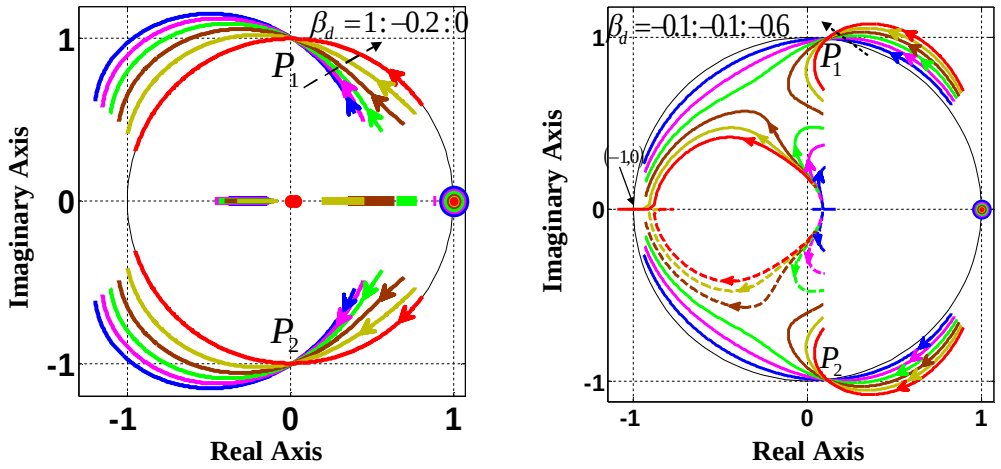

(a) (b)

Fig. 4.9. Pole-maps of $F_{new\text{-}g}$ (z) at β_h=0.2 with sweeping β_{res} for (a) $0<\beta_d\leq 1$, (b) $\beta_d<0$.

4.4 Regions for Stable Open Loop System

From the above discussion, the stability of $F_{new\text{-}g}(z)$ in the two regions of β_d can be identified for certain β_h as follow:

1. $0<\beta_d\leq 1$; for certain β_d in this region, $F_{new\text{-}g}(z)$ is stable only for resonant frequencies below certain value of $\omega_{res\text{-}max}$.
2. $0>\beta_d\geq \beta_{d\text{-}b}$; for certain β_d in this region, $F_{new\text{-}g}(z)$ is stable only over certain range of resonant frequencies between $\omega_{res\text{-}min}$ and $\omega_{res\text{-}high}$.

   The values of $\beta_{res\text{-}max}$, $\beta_{res\text{-}min}$, $\beta_{res\text{-}b}$ and $\beta_{d\text{-}b}$ can be determined for certain value of β_h as follows: at $\beta_{res\text{-}max}$ or $\beta_{res\text{-}min}$, it was shown that $F_{new\text{-}g}(z)$ has five poles: one pole at z=1, two resonant poles at $P_{1,2}$ and two non-resonant poles (will be denoted as P_3 and P_4). Accordingly, the denominator of $F_{new\text{-}g}(z)$ at $\beta_{res\text{-}max}$ or $\beta_{res\text{-}min}$ can be expressed as in (4.10).

$$den\left(F_{new}(z)\right)\Big|_{\beta_{res-max}/\beta_{res-min}} = (z-1)\left(z \pm P_{1,2}\right)(z-P_3)(z-P_4) \qquad (4.10)$$

By expanding (4.10) and equating its coefficients with the denominator coefficients of $F_{new\text{-}g}(z)$, expressed in (4.9), the expressions of (4.11), (4.12) and (4.13) can be derived to determined β_d, P_3 and P_4 respectively.

$$\beta_d = \frac{2\pi\beta_h+2}{4\pi\beta_h} \cdot \frac{\cos\delta - Real\{P_{1,2}\}}{(1-\alpha)\cdot Real\{P_{1,2}\}+\alpha-\cos\delta} \tag{4.11}$$

$$P_3 = \frac{1}{2}\left(2\cos\delta - \omega_{ad} - 2Real\{P_{1,2}\} - \sqrt{\left(2\cos\delta - \omega_{ad} - 2Real\{P_{1,2}\}\right)^2 + \frac{16\pi\beta_d\beta_h(1-\alpha)}{2\pi\beta_h+2}}\right) \tag{4.12}$$

$$P_4 = \frac{4\pi\beta_d\beta_h(1-\alpha)}{(2\pi\beta_h+2)P_3} \tag{4.13}$$

Fig. 4.10 plots β_d along with the magnitudes of P_3 and P_4 versus $\beta_{res\text{-}max}/\beta_{res\text{-}min}$ at β_h of 0.5. Using this figure, it can be implied that:

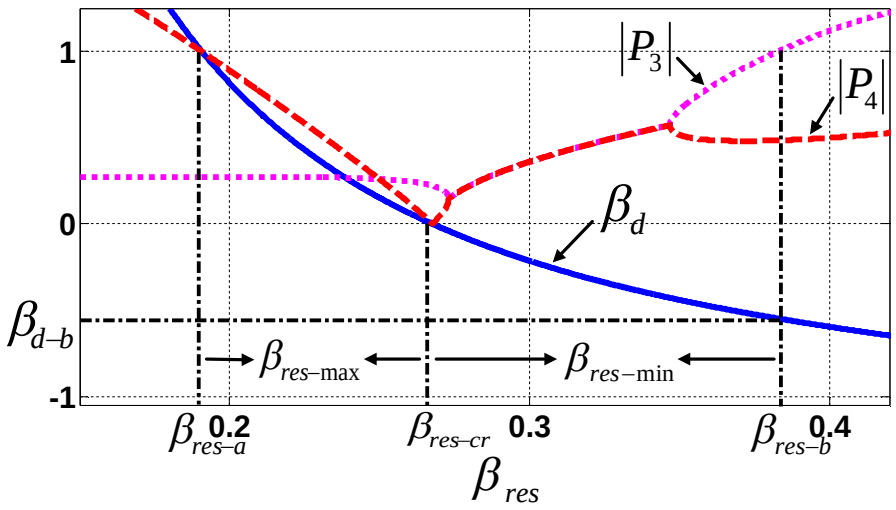

Fig. 4.10. HPF gain factor (β_d) along with $|P_3|$ and $|P_4|$ versus $\beta_{res\text{-}max}/\beta_{res\text{-}min}$ at β_h=0.5.

1. For $0<\beta_d \leq 1$, the minimum limit of $\beta_{res\text{-}max}$ is corresponding to β_d =1 and denoted as $\beta_{res\text{-}a}$. Furthermore, by decreasing r, $\beta_{res\text{-}max}$ increases till reaches its maximum limit at β_d=0. On the other hand, for $0>\beta_d \geq \beta_{d\text{-}b}$, the maximum limit of $\beta_{res\text{-}min}$ is

corresponding to $\beta_{d\text{-}min} = \beta_{d\text{-}b}$. Furthermore, by increasing β_d, $\beta_{res\text{-}min}$ decreases till it reaches its minimum limit at β_d=0. At β_d=0, both $\beta_{res\text{-}max}$ and $\beta_{res\text{-}min}$ have the same value which is denoted as $\beta_{res\text{-}cr}$ and expressed in (4.14) by substituting β_d=0 in (4.11). It is shown from Figs. 4.7 till 4.9 that decreasing β_h causes right movement for the poles $P_{1,2}$ on the unit circle; and, in turn, increasing of $real\{P_{1,2}\}$. Accordingly, from (4.14), $\beta_{res\text{-}cr}$ decrease as β_h decreases; and, in turn, the maximum value for $\beta_{res\text{-}cr}$ is corresponding to β_h=0.5 at which $real\{P_{1,2}\}$ is determined from Figs. 4.6(a) or 4.6(b) as -0.111. By substituting this value into (4.14), the maximum value of $\beta_{res\text{-}cr}$ is determined as 0.268. Therefore, for $0<\beta_d\leq 1$, $F_{new\text{-}g}(z)$ can be stable only for resonant frequencies less than $0.268\omega_s$.

$$\beta_{res-cr} = \frac{\cos^{-1}(Real\{P_{1,2}\})}{2\pi} \tag{4.14}$$

2. For $0>\beta_d\geq \beta_{d\text{-}b}$, both $\beta_{d\text{-}b}$ and $\beta_{res\text{-}b}$ are corresponding to one pole of P_3 or P_4 at (-1,0).Thus $\beta_{d\text{-}b}$ and $\beta_{res\text{-}b}$ can be determined from Fig. 4.10 by locating their values at unity magnitude of P_3 or P_4.

$\beta_{res\text{-}high}$ is not corresponding to resonant poles at $P_{1,2}$, it is corresponding only to one pole of P_3 or P_4 at (-1,0); so, it cannot be determined from Fig. 4.10. However, at high values of β_d in its second region, the non-resonant poles track entirely inside the unit circle over the entire range of β_{res} as shown in Figs. 4.7 (b), 4.8 (b) and 4.9 (b) (e.g. the non-resonant poles track entirely inside the unit circle for β_d of -0.1 and -0.2). Hence the stable range of $F_{new\text{-}g}(z)$ can be extended to $\beta_{res\text{-}high}$ of 0.45 (the maximum considered limit of β_{res}) using high values of β_d in its second region.

Then, using Fig. 4.10, the stable regions of $F_{new\text{-}g}(z)$ can be re-identified at constant β_h as follow:

1. For $\beta_{res} \leq \beta_{res\text{-}a}$, $F_{new\text{-}g}(z)$ can be stable only in the first region of β_d ($0<\beta_d \leq 1$).

2. For $\beta_{res\text{-}a}<\beta_{res}<\beta_{res\text{-}cr}$, $F_{new\text{-}g}(z)$ can be stable only over certain range in the first region of β_d between 0 and the value of β_d corresponding to β_{res} in Fig. 4.10.
3. For $\beta_{res\text{-}cr}<\beta_{res}<\beta_{res\text{-}b}$, $F_{new\text{-}g}(z)$ can be stable only over certain range in the second region of β_d between 0 and the value of β_d corresponding to β_{res} in Fig. 4.10.

4.5 Control System Design

4.5.1 HPF Cutoff Frequency Tuning (β_h tuning)

To tune β_h, the pole-maps of $F_{new\text{-}g}(z)$ are plotted with sweeping β_h for different values of β_{res} in the two identified regions of β_d:

- **First region; $0<\beta_d\leq 1$**, the pole-maps are plotted in Figs. 4.11 (a), (b) and (c) for three values of r at 0.2, 0.5 and 0.8 respectively. In each figure, three β_{res} values of 0.17, 0.2 and 0.24 are considered (these values are less than $\beta_{res\text{-}cr}$=0.268; above which positive β_d cannot be used for the stability of $F_{new\text{-}g}(z)$). By increasing β_h, the resonant poles may track entirely outside or inside the unit circle or it may initially track outside the unit circle before tracking inside the unit circle with increasing β_h. To ensure the stability of $F_{new\text{-}g}(z)$, high β_h should be adopted. Theoretically, β_h can be extended to 0.5; however, such value can deteriorate the discretization process. A value of β_h=0.4 will be adopted. At this value, $\beta_{res\text{-}cr}$ and $\beta_{res\text{-}a}$ are determined by plotting the pole-map of $F_{new\text{-}g}(z)$ with sweeping β_{res} at any constant value of β_d (any of the pole-maps in Fig. 4.7(a) or Fig. 4.7(b) can be used). From these figures, $real\{P_{1,2}\}$ is determined as -0.0562. Using (4.11), (4.12) and (4.13), Fig. 4.12 plots β_d along with the magnitudes of P_3 and P_4 versus $\beta_{res\text{-}max}/\beta_{res\text{-}min}$ in the first region of β_d. From this figure,$\beta_{res\text{-}cr}$ and $\beta_{res\text{-}a}$ are determined as 0.188 and 0.259 respectively. Then the first and the second regions of β_{res} at β_h=0.4 are identified as $\beta_{res}\leq 0.188$ and $0.188<\beta_{res}<0.259$ respectively.

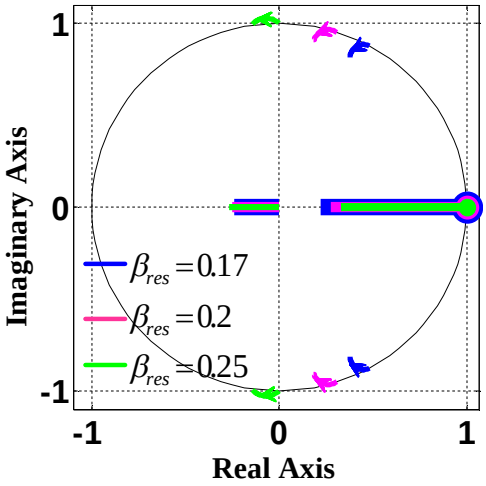

(a)

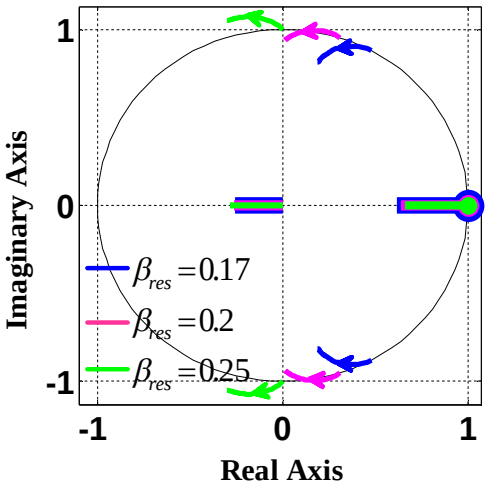

(b)

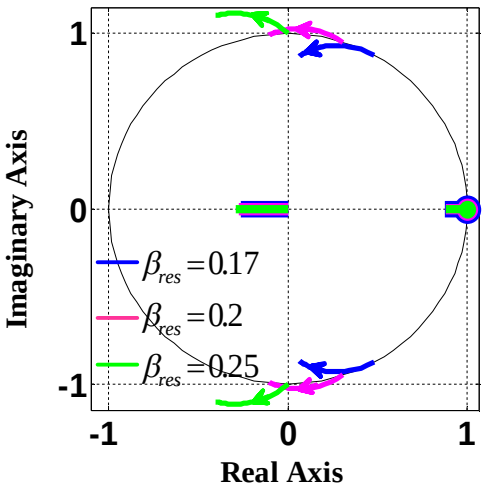

(c)

Fig. 4.11. Pole-maps of $F_{new\text{-}g}(z)$ with sweeping β_h at different β_{res} and different values of r in its first region ($0<\beta_d\leq 1$). (a) β_d=0.2, (b) β_d=0.5 and (c) β_d=0.8.

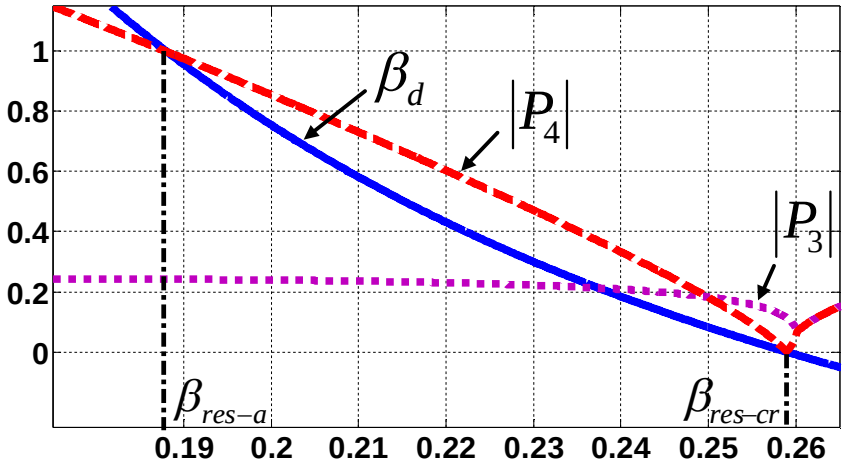

Fig. 4.12. HPF gain factor (β_d) along with $|P_3|$ and $|P_4|$ versus $\beta_{res\text{-}max}$ at β_h =0.4.

- ***Second region*; $0>\beta_d\geq\beta_{d\text{-}b}$**, the pole-maps of $F_{new\text{-}g}(z)$ are plotted in Figs. 4.13 (a), (b) and (c) for values of β_d at -0.2, -0.4 and -0.6, respectively. In each figure, three β_{res} values of 0.3, 0.34 and 0.38 are considered. By increasing β_h, the resonant poles may track entirely inside the unit circle or it may initially track inside the unit circle before tracking outside the unit circle with increasing β_h. From these pole-maps, using a medium value for β_h (0.25) is a good tradeoff to ensure the stability of $F_{new\text{-}g}(z)$. At this value, $\beta_{res\text{-}cr}$ and $\beta_{res\text{-}b}$ can be determined by plotting the pole-map of $F_{new\text{-}g}(z)$ with sweeping β_{res} at any value of β_d (β_d=1 is used) as shown in Fig. 4.14 (a) from which $real\{P_{1,2}\}$ is determined as 0.0653. Using (4.11), (4.12) and (4.13), Fig. 4.14 (b) plots β_d and the magnitudes of P_3 and P_4 versus $\beta_{res\text{-}max}/\beta_{res\text{-}min}$ in the second region of β_d. From this figure, $\beta_{res\text{-}cr}$ and $\beta_{res\text{-}b}$ are determined as 0.239 and 0.395 respectively; also $\beta_{d\text{-}b}$ is determined as -0.875. Then the third region of β_{res} at β_h=0.25 is identified as $0.239<\beta_{res}<0.395$. Note that, as indicated previously, for values of $0.395<\beta_{res}<0.45$, higher values of β_d in its second region has to be adopted to stabilize $F_{new\text{-}g}(z)$ (e.g. -0.1 and -0.2).

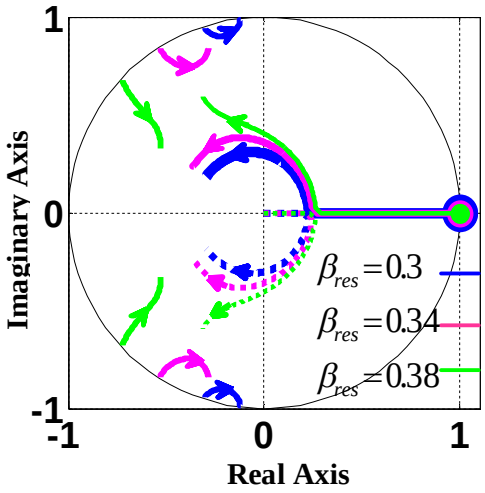

(a)

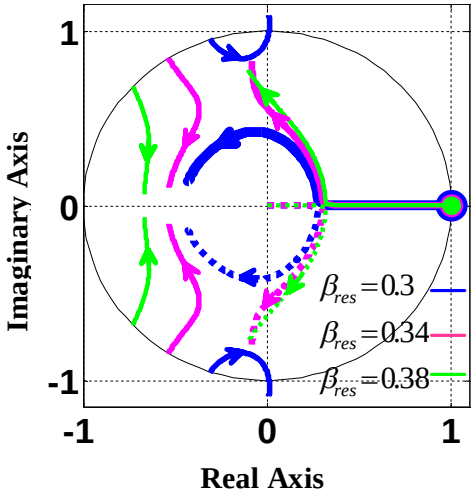

(b)

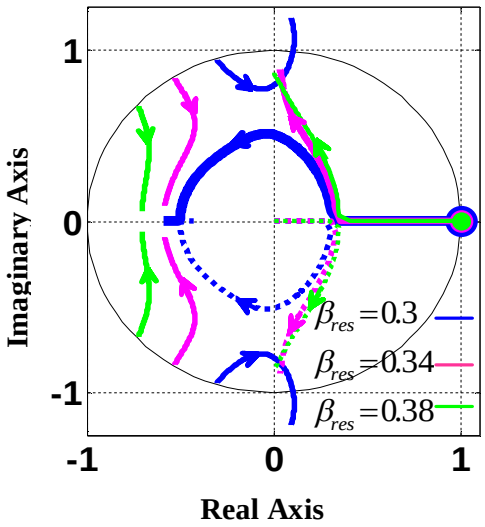

(c)

Fig. 4.13. Pole-maps of $F_{new\text{-}g}(z)$ with sweeping β_h at different β_{res} and different values of β_d in its second region ($0>\beta_d\geq\beta_{d\text{-}b}$). (a) β_d=-0.2, (b) β_d=-0.4 and (c) β_d=-0.6.

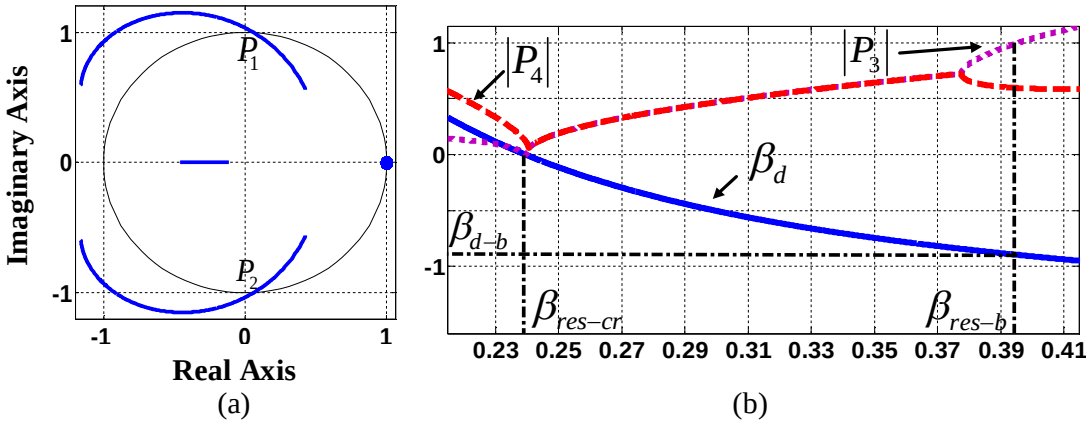

Fig. 4.14. At β_h=0.25, (a) Pole-map of $F_{new\text{-}g}(z)$, (b) HPF gain factor (β_d) along with $|P_3|$ an $|P_4|$ versus $\beta_{res\text{-}min}$.

- If β_{res} is between 0.239 ($\beta_{res\text{-}cr}$ at β_h =0.25) and 0.259 ($\beta_{res\text{-}cr}$ at β_h =0.4), either β_h of 0.25 or 0.4 with the corresponding regions of β_d can be used.

4.5.2 Control Parameters Design

The design objectives of the overall system are:

1. To ensure the stability of $F_{new\text{-}g}(z)$.
2. To meet pre-specified values of fundamental loop gain (T_{fo}) and crossover frequency (ω_c).

The equivalent *s*-domain model, shown in Fig. 4.15, is used to design the control parameters.

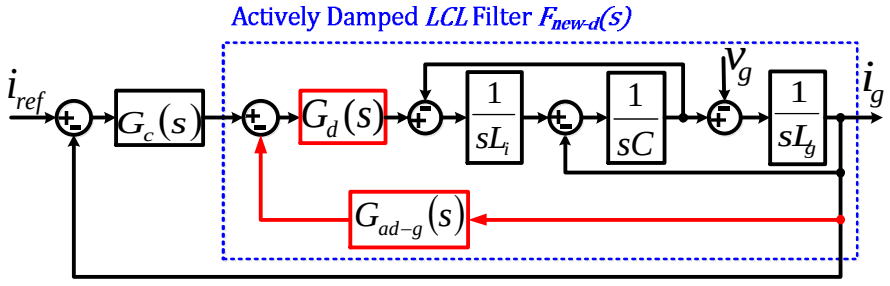

Fig. 4.15 S-domain representation for the discrete control system.

It can be shown that the equivalent s-domain actively damped filter has the same transfer function as the proposed system presented in the previous chapter. So, the same relations to determine the PR controller parameters, k_p and k_r, can be employed here. These relations are re-written below.

$$K_p = \omega_c(L_i + L_g)A_c \tag{4.15}$$

$$K_r = \omega_o(L_i + L_g)A_o \cdot 10^{\frac{T_{fo}}{20}} \tag{4.16}$$

where $A_c = \sqrt{1 + \beta_d^2 - 2\beta_d \cos(1.5T_s\omega_c)}$ & $A_o = \sqrt{1 + \beta_d^2 - 2\beta_d \cos(1.5T_s\omega_o)}$

Substituting of (4.15) and (4.16) into (4.4), $G_c(z)$ is expressed in terms of β_d and the pre-specified quantities as in (4.17).

$$G_c(z) = \omega_c(L_i + L_g)A_c + \frac{\omega_o(L_i+L_g)A_o \cdot 10^{\frac{T_{fo}}{20}} \cdot sin(\omega_o T_s)(z^2-1)}{2\omega_o(z^2-2z\,cos(\omega_o T_s)+1)} \tag{4.17}$$

From Fig. 4.4, the discrete closed loop transfer function is expressed in (4.18).

$$T_{closed}(z) = \frac{G_c(z)F_{new-g}(z)}{1+G_c(z)F_{new-g}(z)} \tag{4.18}$$

Using the above-addressed expressions, the control parameters are co-designed as follow:

1. Check the value of β_{res}; if $\beta_{res} \leq 0.259$, use high β_h (0.4); if β_{res}>0.259, use medium β_h (0.25).
2. Using (4.11), (4.12) and (4.13), plot β_d along with $|P_3|$ and $|P_4|$ versus $\beta_{res\text{-}max}/\beta_{res\text{-}min}$ for the adopted β_h and determine β_d corresponding to β_{res}.
3. Identify the range of β_d for stability of $F_{new}(z)$ as follow:
   a. For $\beta_{res} \leq 0.188$, the stable range is $0 < \beta_d \leq 1$.
   b. For $0.188 < \beta_{res} < 0.259$, the stable range is from 0 to the value of β_d in its first region corresponding to β_{res}.
   c. For β_{res}>0.259, the stable range is from 0 to the value of β_d in its second region corresponding to β_{res}.

4. Use the adopted β_h along with the pre-specified quantities (T_{fo} and ω_c) to plot the pole-map of T_{closed}, expressed in (4.18), with sweeping β_d over its identified range in step 3. Select the value for β_d corresponding to the farthest poles inside the unit circle.
5. Use the selected β_d to determine K_p and K_r from (4.15) and (4.16) respectively.

4.6 Numerical & Experimental Verification

4.6.1 Numerical Example

Table 4.1 presents the parameters of the system shown in Fig. 4.1. Four capacitance values, corresponding to β_{res} of 0.146, 0.197, 0.296 and 0.379 are used to verify the proposed tuning steps. These values are respectively denoted as β_{res1}, β_{res2}, β_{res3} and β_{res4} with corresponding resonant frequencies denoted as ω_{res1}, ω_{res2}, ω_{res3} and ω_{res4} respectively. T_{fo} is specified as 65 dB, and ω_c is specified as ratio of the corresponding resonant frequencies as follows: $0.3\omega_{res1}$, $0.25\omega_{res2}$, $0.22\omega_{res3}$ and $0.18\omega_{res4}$.

Table 4.1

System parameters

Symbol	Quantity	Value
P	Rated power	1 kW
V_g	Grid voltage	120 V
F_o	Grid Frequency	50 Hz
V_{dc}	DC Voltage	220 V
L_i	Inverter side inductance	2.75 mH
L_g	Grid side inductance	1.2 mH
C	Capacitance	22.2 µF, 12.2 µF, 5.4 µF, and 3.3 µF
f_{sw}	Switching Frequency	8 kHz
f_s	Sampling Frequency	8 kHz

At the beginning, a value of β_h=0.4 is adopted for β_{res} of 0.146 and 0.197. On the other hand, a value of β_h=0.25 is adopted for β_{res} of 0.296 and 0.379. Then, for these values of β_h, Figs. 4.12 and 4.14 (b) plot β_d versus $\beta_{res\text{-}max}/\beta_{res\text{-}min}$. From Fig. 4.12, β_d for β_{res2} is determined as 0.83. From Fig. 4.14 (b), β_d for β_{res3} and β_{res4} are determined as -0.48 and -0.84 respectively. To complete the tuning process, the pole-map of $T_{closed}(z)$ are plotted over the corresponding stable range of β_d for each value of β_{res} as follow:

- $0<\beta_d\leq 1$ for β_{res1}=0.146 (<0.188).
- $0<\beta_d<0.83$ for β_{res2}=0.197.
- $0>\beta_d>-0.48$ for β_{res3}=0.296.
- $0>\beta_d>-0.84$ for β_{res4}=0.379.

Then, values of β_d corresponding to farthest closed loop poles inside the unit circle are selected as 0.24, 0.16, -0.12 and -0.18 for β_{res1}, β_{res2}, β_{res3} and β_{res4} respectively. Finally, K_p and K_r are determined from (4.15) and (4.16). Table 4.2 lists the designed control parameters along with the experimental results introduced later.

4.6.2 Experimental Results

Using the experimental set-up described in the previous chapter, experimental investigations have been conducted using the designed parameters listed in Table 4.2. The experimental work has been done at the four resonant frequencies considered in the above numerical example using the corresponding designed control parameters. The control scheme has been implemented using PE-Expert3 platform that consists of C6713-A DSP development board along with high-speed PEV board for analog-to-digital conversion and PWM gate signals generation. To verify the transient characteristics, the rms value of the reference current (I_{ref}) is stepped up from 4.167 Arms to 8.333 Arms (rated value).

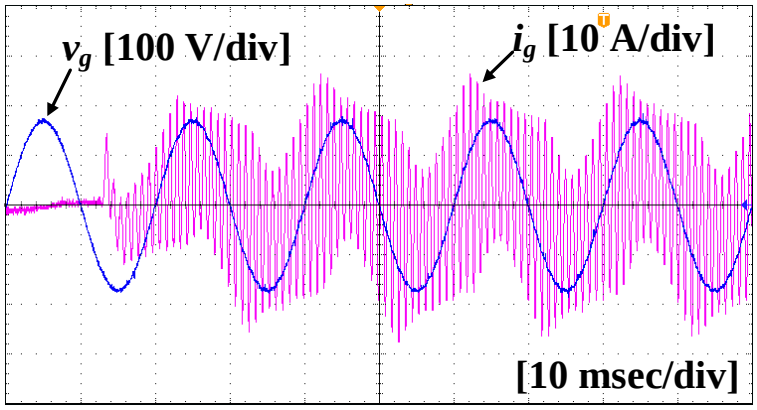

(a)

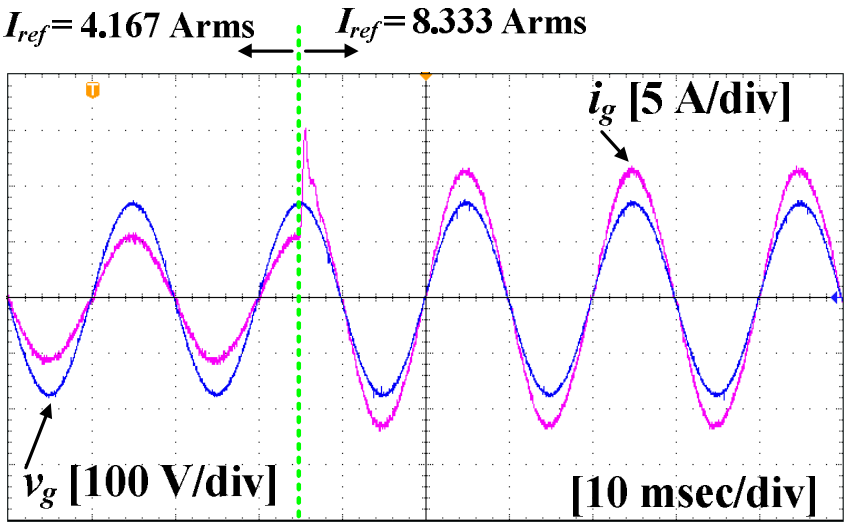

(b)

Fig. 4.16. Experimental measurements of grid voltage (v_g) and current (i_g) for β_{res1}=0.146, (a) without AD, (b) with AD.

For ω_{res1}, which is lower than one-sixth of the sampling frequency, the system cannot be stabilized without active damper (AD). Thus removing the active damping loop causes high oscillatory current as shown in Fig. 4.16(a). On the other hand, Fig. 4.16(b) shows the waveforms when using the active damping loop. These waveforms indicate clearly the stabilization effect of the active damping loop for resonant frequencies less than one-sixth of the sampling frequency.

For ω_{res2}, ω_{res3} and ω_{res4}, the system can be stabilized without AD. However, with increasing the grid side inductance, the system stability can be violated. Moreover, oscillatory resonant currents can be generated in this case.

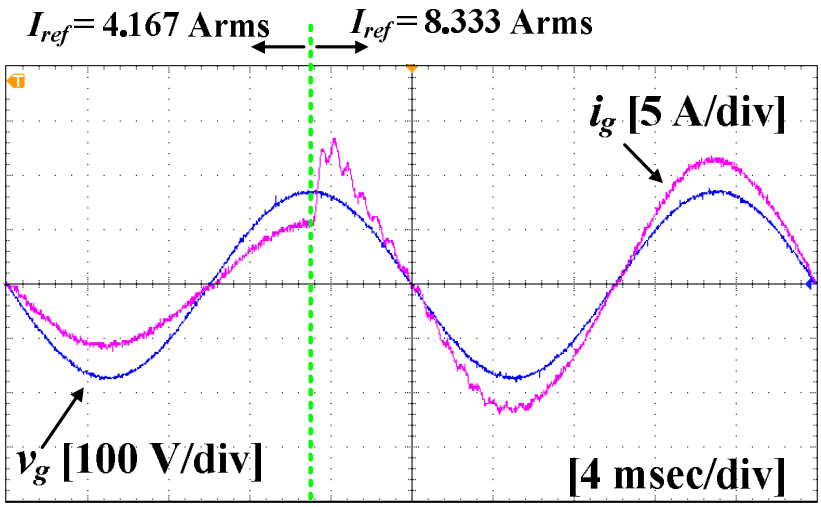

(a)

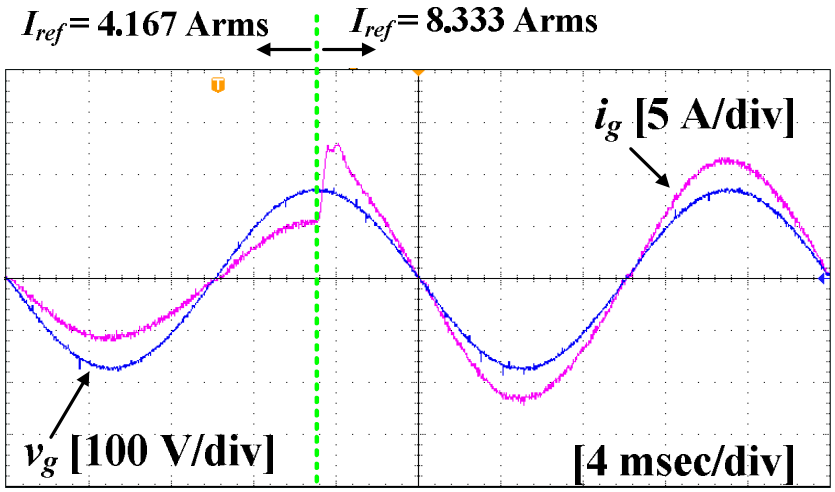

(b)

Fig. 4.17. Experimental measurements of grid voltage (v_g) and current (i_g) for β_{res2}=0.197, (a) without AD, (b) with AD.

For ω_{res2}, Fig. 4.17(a) shows the waveforms without using AD. It can be recognized the oscillatory resonant currents in this case. These oscillatory components can be much worse if the grid voltage contains some harmonic components around the resonant frequency. Fig. 4.17(b) shows the waveforms when using AD. It can be

recognized the mitigation effect introduced by AD in this case. Finally, for ω_{res3} and ω_{res4}, Figs. 4.18(a) and (b) show respectively the waveforms using AD.

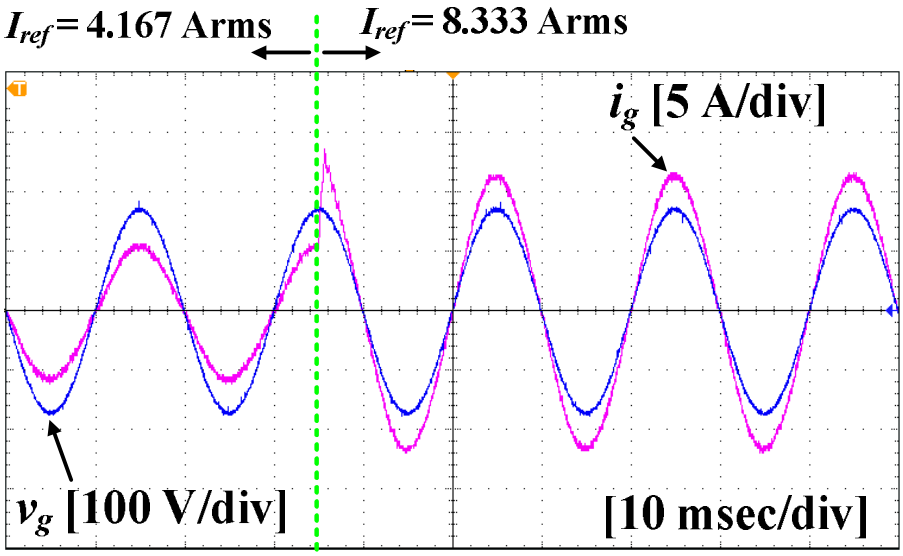

(a)

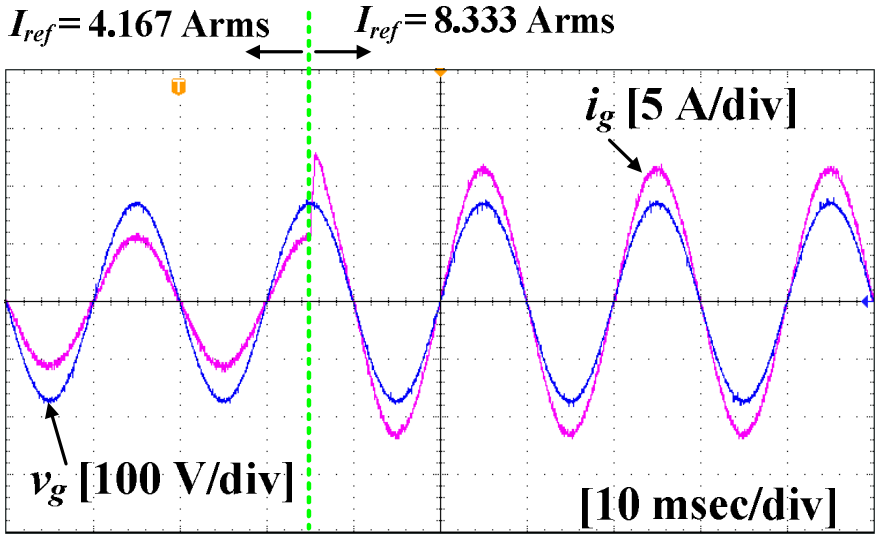

(b)

Fig. 4.18. Experimental measurements of grid voltage (v_g) and current (i_g) with AD at: (a) β_{res3}=0.296, (b) β_{res4}=0.379.

At steady state conditions, Table 4.2 presents the measured fundamental current component (I_{g1}), the power factor (PF), and the steady state error $\left(E_{ss} = \left|\left(I_{ref} - I_{g1}\right)/I_{ref}\right| \times 100\right)$.These results reflect satisfactory steady state and transient

performances along with resonance damping over the entire possible range of resonant frequencies.

Table 4.2

Designed Parameters & Experimental Results

C (μF)	β_{res}	Designed Controller				Experimental Results		
		β_h	r	K_p	K_r	I_{g1}	E_{ss}	PF
22.2	0.146	0.4	0.24	6.84	1678	8	0.04	0.999
12.2	0.197	0.4	0.16	8.41	1854	8.01	0.039	0.999
5.4	0.296	0.25	-0.1	14.01	2427	7.98	0.042	0.999
3.3	0.379	0.25	-0.18	15.56	2600	8.03	0.037	0.999

4.7 Summary

This chapter investigates active damping of *LCL* filter resonance using HPF of the grid current feedback. A new expression for this HPF, in terms of the filter components, has been derived. This expression facilitates a general stability study for the actively damped filter. Through discrete time domain investigation for the actively damped filter, three regions of resonant frequencies have been identified for stable open loop behavior at certain HPF cutoff frequency. These regions cover wide range of resonant frequencies up to 0.39 of the sampling frequency. Moreover, straightforward co-design steps for both the HPF and the fundamental current regulator have been proposed. Numerical example and experimental work have been introduced. The results show that good steady state and dynamic performance along with resonance damping can be obtained over wide range of resonant frequencies using the proposed co-design steps of the control parameters.

Chapter 5:

Conclusion and Future Work

5.1 Conclusion:

Out of this search, some important conclusions can be summarized as follows:

1. Observer-based-active damping method has been investigated. The observer poles are selected to be faster than the plant poles. This in turn, facilitates a separate design for the fundamental current regulator along with the active damping coefficient to meet pre-specified values of cross over frequency and damping behavior. The results show that the observer-based system offer a good damping behavior without the need for additional sensors. Moreover, compared to sensor-based system, it offers lower switching ripples.
2. A novel active damping strategy using two feedback loops of the grid current and filter capacitor voltage has been proposed. Compared to the existing active damping methods, the proposed strategy can offer the following merits.
    a. Compared to the capacitor-current-based method, the cost can be reduced by omitting the high cost current sensor. Moreover, the non-minimum phase behavior can be avoided over a wide range of resonant frequencies.
    b. Compared to the capacitor-voltage-based method, the proposed strategy can behave effectively over a wide range of the resonant frequencies without stability violations.

c. Compared to the grid current based method, a straightforward co-design method for the fundamental current regulator and the active damping loops are proposed.

3. Grid-current-based active damping using high-pass filter (HPF) of the grid current has been investigated. Three regions of resonant frequencies have been identified for stable open loop behavior at certain HPF cutoff frequency. These regions cover wide range of resonant frequencies up to 0.39 of the sampling frequency.
4. Straightforward co-design steps for both the control parameters of grid-current-based active damping method have been proposed. The results show that good steady state and dynamic performance along with resonance damping can be obtained over wide range of resonant frequencies using the proposed co-design steps of the control parameters.

5.2 Future Work:

1. Studying the effect of using different sampling frequencies in the active damping loops of the proposed active damping method.
2. Investigation the interaction between the developed active damping strategies and the other control objectives such as harmonic suppression techniques.
3. Applying grid-inductance estimation techniques with the developed active damping algorithms to increase the system robustness.
4. Investigation the effect of different scenarios which may occur with parallel converters connection.

References

[1] R. Teodorescu, M. Liserre, and P. Rodriguez, *Grid converters for photovoltaic and wind power systems*, Chichester, West Sussex ; Hoboken, N.J: IEEE ; Wiley, 2011.

[2] S. Buso and P. Mattavelli, *Digital control in power electronics*, Morgan & Claypool, 2006.

[3] T. M. Blooming, and D. J. Carnovale, "Application of IEEE Std. 519-1992 harmonic limits," in *Proc. Annu. Pulp and Paper Industry Technical Conf.*, pp. 1-9, 2006.

[4] R. Teodorescu, F. Blaabjerg, U. Borup, and M. Liserre, "A new control structure for grid-connected LCL PV inverters with zero steady-state error and selective harmonic compensation," in *Proc. 19th Annu. IEEE Appl. Power Electron. Conf. Expo., APEC*, 2004, vol. 1, pp. 580–586.

[5] A. Reznik, M. G. Simoes, A. Al-Durra, and S. M. Muyeen, "LCL filter design and performance analysis for grid-interconnected systems," *IEEE Trans. Ind. Appl.*, vol. 50, no. 2, pp. 1225–1232, Mar. 2014.

[6] M. Liserre, F. Blaabjerg, and S. Hansen, "Design and control of an LCL-filter-based three-phase active rectifier," *IEEE Trans. Ind. Appl.*, vol. 41, no. 5, pp. 1281–1291, Sep. 2005.

[7] Y. Tang, P. C. Loh, P. Wang, F. H. Choo, F. Gao, and F. Blaabjerg, "Design, control, and implementation of LCL-filter-based shunt active power filters," in *Proc. 26th Annu. IEEE Appl. Power Electron. Conf. Expo., APEC*, 2011, pp. 98–105.

[8] B.-G. Cho and S.-K. Sul, "LCL filter design for grid-connected voltage-source converters in high power systems," in *Proc. IEEE Energy Conversion Congress and Exposition Conf., ECCE*, 2012, pp. 1548–1555.

[9] M. Routimo and H. Tuusa, "LCL type supply filter for active power filter - comparison of an active and a passive method for resonance damping," in *Proc. IEEE Power Electron. Specialists Conf., PESC*, 2007, pp. 2939–2945.

[10] J. Muhlethaler, M. Schweizer, R. Blattmann, J. W. Kolar, and A. Ecklebe, "Optimal design of LCL harmonic filters for three-phase PFC rectifiers," in *37th Annu. IEEE Ind. Electron. Society Conf., IECON*, 2011, pp. 1503–1510.

[11] K. H. Ahmed, S. J. Finney, and B. W. Williams, "Passive filter design for three-phase inverter interfacing in distributed generation," in *Proc. Compatibility in Power Electron., CPE '07*, 2007, pp. 1–9.

[12] J. Yin, S. Duan, and B. Liu, "Stability analysis of grid-connected inverter with LCL filter adopting a digital single-loop controller with inherent damping characteristic," *IEEE Trans. Ind. Inform.*, vol. 9, no. 2, pp. 1104–1112, May 2013.

[13] S. G. Parker, B. P. McGrath, and D. G. Holmes, "Regions of active damping control for LCL filters," *IEEE Trans. Ind. Appl.*, vol. 50, no. 1, pp. 424–432, Jan. 2014.

[14] Y. Tang, P. C. Loh, P. Wang, F. H. Choo, and F. Gao, "Exploring inherent damping characteristic of LCL-filters for three-phase grid-connected voltage source inverters," *IEEE Trans. Power Electron.*, vol. 27, no. 3, pp. 1433–1443, Mar. 2012.

[15] M. H. Bierhoff and F. W. Fuchs, "Active damping for three-phase PWM rectifiers with high-order line-side filters," *IEEE Trans. Ind. Electron.*, vol. 56, no. 2, pp. 371–379, Feb. 2009.

[16] J. Dannehl, C. Wessels, and F. W. Fuchs, "Limitations of voltage-oriented PI current control of grid-connected PWM rectifiers With LCL filters," *IEEE Trans. Ind. Electron.*, vol. 56, no. 2, pp. 380–388, Feb. 2009.

[17] L. Corradini, D. Maksimović, P. Mattavelli, and R. Zane, *Digital control of high-frequency switched-mode power converters*. Hoboken, New Jersey: IEEE, John Wiley & Sons Inc, 2015.

[18] D. O. Neacsu, *Switching power converters: medium and high power*, 2nd ed. Boca Raton, Fla.: CRC Press, 2013.

[19] J. G. Hwang, P. W. Lehn, and M. Winkelnkemper, "A generalized class of stationary frame-current controllers for grid-connected AC-DC converters," *IEEE Trans. Power Deliv.*, vol. 25, no. 4, pp. 2742–2751, Oct. 2010.

[20] A. G. Yepes, F. D. Freijedo, O. Lopez, and J. Doval-Gandoy, "Analysis and design of resonant current controllers for voltage-source converters by means of nyquist diagrams and sensitivity function," *IEEE Trans. Ind. Electron.*, vol. 58, no. 11, pp. 5231–5250, Nov. 2011.

[21] A. R. Dash, B. C. Babu, K. B. Mohanty, and R. Dubey, "Analysis of PI and PR controllers for distributed power generation system under unbalanced grid

faults," in *Proc. Int. Conf. on Power and Energy Systems (ICPS)*, 2011, pp. 1–6.

[22] Guoqiao Shen, Xuancai Zhu, Jun Zhang, and Dehong Xu, "A new feedback method for PR current control of LCL-filter-based grid-connected inverter," *IEEE Trans. Ind. Electron.*, vol. 57, no. 6, pp. 2033–2041, Jun. 2010.

[23] T. Midtsund, J. A. Suul, and T. Undeland, "Evaluation of current controller performance and stability for voltage source converters connected to a weak grid," in *Proc. 2nd Int. Symposium on Power Electron. for Distributed Generation Systems*, 2010, pp. 382–388.

[24] J. Dannehl, F. W. Fuchs, S. Hansen, and P. B. Thøgersen, "Investigation of Active Damping Approaches for PI-Based Current Control of Grid-Connected Pulse Width Modulation Converters With LCL Filters," *IEEE Trans. Ind. Appl.*, vol. 46, no. 4, pp. 1509–1517, Jul. 2010.

[25] N. Geddada and M. K. Mishra, "LCL filter with active damping using PI and SSI regulators in synchronous rotating reference frame current controller for DSTATCOM," *Int. J. Emerg. Electr. Power Syst.*, vol. 14, no. 4, Jan. 2013.

[26] R. Teodorescu, F. Blaabjerg, M. Liserre, and P. C. Loh, "Proportional-resonant controllers and filters for grid-connected voltage-source converters," *IEE Proc. Electr. Power Appl.*, vol. 153, no. 5, p. 750, 2006.

[27] A. Kuperman, "Proportional-resonant current controllers design based on desired transient performance," *IEEE Trans. Power Electron.*, vol. 30, no. 10, pp. 5341–5345, Oct. 2015.

[28] Chenlei Bao, Xinbo Ruan, Xuehua Wang, Weiwei Li, Donghua Pan, and Kailei Weng, "Step-by-step controller design for LCL-type grid-connected inverter with capacitor-current-feedback active-damping," *IEEE Trans. Power Electron.*, vol. 29, no. 3, pp. 1239–1253, Mar. 2014.

[29] J. Doval-Gandoy, Ó. López, J. Malvar, A. G. Yepes, F. D. Freijedo, and A. Vidal, "Transient response evaluation of stationary-frame resonant current controllers for grid-connected applications," *IET Power Electron.*, vol. 7, no. 7, pp. 1714–1724, Jul. 2014.

[30] M. Lindgren and J. Svensson, "Control of a voltage-source converter connected to the grid through an LCL-filter-application to active filtering," in *Proc. 29th Annu IEEE Power Electron. Specialists Conf., PESC 98 Record*, 1998, vol. 1, pp. 229–235.

[31] K. Nishida, T. Ahmed, and M. Nakaoka, "Cost-effective deadbeat current control for wind-energy inverter application with LCL filter," *IEEE Trans. Ind. Appl.*, vol. 50, no. 2, pp. 1185–1197, Mar. 2014.

[32] A. Papavasiliou, S. A. Papathanassiou, S. N. Manias, and G. Demetriadis, "Current control of a voltage source inverter connected to the grid via LCL filter," in *Proc. IEEE Power Electron. Specialists Conf., PESC*, 2007, pp. 2379–2384.

[33] R. Kadri, J.-P. Gaubert, G. Champenois, and M. Mostefai, "Design of a single-phase grid-connected photovoltaic system based on deadbeat current control with LCL filter," in *Proc. 14th Int. Power Electronics and Motion Control Conference (EPE/PEMC)*, 2010.

[34] E. Wu and P. W. Lehn, "Digital current control of a voltage source converter with active damping of LCL resonance," *IEEE Trans. Power Electron.*, vol. 21, no. 5, pp. 1364–1373, Sep. 2006.

[35] J. He, Y. W. Li, D. Bosnjak, and B. Harris, "Investigation and resonances damping of multiple PV inverters," in *Proc. 27th Annu. IEEE Appl. Power Electron. Conf. Expo., APEC*, 2012, pp. 246–253.

[36] Yang Han, Lin Xu, M. M. Khan, Chen Chen, Gang Yao, and Li-Dan Zhou, "Robust deadbeat control scheme for a hybrid APF with resetting filter and ADALINE-based harmonic estimation algorithm," *IEEE Trans. Ind. Electron.*, vol. 58, no. 9, pp. 3893–3904, Sep. 2011.

[37] C. Fischer, S. Mariethoz, and M. Morari, "A model predictive control approach to reducing low order harmonics in grid inverters with LCL filters," in *Proc. 39th Annu. IEEE Industrial Electronics Society Conf., IECON*, 2013, pp. 3252–3257.

[38] S. Mariethoz, A. G. Beccuti, and M. Morari, "Analysis and optimal current control of a voltage source inverter connected to the grid through an LCL filter," in *Proc. IEEE Power Electron. Specialists Conf., PESC*, 2008, pp. 2132–2138.

[39] G. S. Perantzakis, F. H. Xepapas, and S. N. Manias, "Efficient predictive current control technique for multilevel voltage source inverters," in *Proc. Power Electron. and App. European Conf.*, 2005, P.10.

[40] S. Mariethoz and M. Morari, "Explicit model-predictive control of a PWM inverter with an LCL filter," *IEEE Trans. Ind. Electron.*, vol. 56, no. 2, pp. 389–399, Feb. 2009.

[41] S. Kouro, P. Cortes, R. Vargas, U. Ammann, and J. Rodriguez, "Model predictive control - a simple and powerful method to control power converters," *IEEE Trans. Ind. Electron.*, vol. 56, no. 6, pp. 1826–1838, Jun. 2009.

[42] H. Miranda, R. Teodorescu, P. Rodriguez, and L. Helle, "Model predictive current control for high-power grid-connected converters with output LCL filter," in *Proc. 35th Annu. IEEE Ind. Electron. Society Conf., IECON*, 2009, pp. 633–638.

[43] J. Scoltock, T. Geyer, and U. Madawala, "Model predictive direct current control for a grid-connected converter: LCL-filter versus L-filter," in *Proc. IEEE Int. Conf. on Ind. Technology (ICIT)*, 2013, pp. 576–581.

[44] J. Rodriguez *et al.*, "Predictive current control of a voltage source inverter," *IEEE Trans. Ind. Electron.*, vol. 54, no. 1, pp. 495–503, Feb. 2007.

[45] H.-S. Heo, G.-H. Choe, and H.-S. Mok, "Robust predictive current control of a grid-connected inverter with harmonics compensation," in *Proc. 28th Annu. IEEE Appl. Power Electron. Conf. Expo., APEC*, 2013, pp. 2212–2217.

[46] F. Huerta, E. Bueno, S. Cobreces, F. J. Rodriguez, and C. Giron, "Control of grid-connected voltage source converters with LCL filter using a Linear Quadratic servocontroller with state estimator," in *Proc. IEEE Power Electron. Specialists Conf., PESC*, 2008, pp. 3794–3800.

[47] E. J. Bueno, F. Espinosa, F. J. Rodriguez, J. Urefia, and S. Cobreces, "Current control of voltage source converters connected to the grid through an LCL-filter," in *Proc. 35th Annu. IEEE Power Electron. Specialists Conf., PESC 04*, 2004, pp. 68–73.

[48] M. Xue, Y. Zhang, Y. Kang, Y. Yi, S. Li, and F. Liu, "Full feedforward of grid voltage for discrete state feedback controlled grid-connected inverter with LCL filter," *IEEE Trans. Power Electron.*, vol. 27, no. 10, pp. 4234–4247, Oct. 2012.

[49] E. Twining and D. G. Holmes, "Grid current regulation of a three-phase voltage source inverter with an LCL input filter," *IEEE Trans. Power Electron.*, vol. 18, no. 3, pp. 888–895, May 2003.

[50] F. Huerta, D. Pizarro, S. Cobreces, F. J. Rodriguez, C. Giron, and A. Rodriguez, "LQG servo controller for the current control of LCL Grid-connected voltage-source converters," *IEEE Trans. Ind. Electron*., vol. 59, no. 11, pp. 4272–4284, Nov. 2012.

[51] Fei Liu, Yan Zhou, Shanxu Duan, Jinjun Yin, Bangyin Liu, and Fangrui Liu, "Parameter design of a two-current-loop controller used in a grid-connected inverter system with LCL filter," *IEEE Trans. Ind. Electron.*, vol. 56, no. 11, pp. 4483–4491, Nov. 2009.

[52] J. Dannehl, F. W. Fuchs, and P. B. Thogersen, "PI state space current control of grid-connected PWM converters with LCL filters," *IEEE Trans. Power Electron.*, vol. 25, no. 9, pp. 2320–2330, Sep. 2010.

[53] X. Bao, F. Zhuo, Y. Tian, and P. Tan, "Simplified feedback linearization control of three-phase photovoltaic inverter with an LCL filter," *IEEE Trans. Power Electron*., vol. 28, no. 6, pp. 2739–2752, Jun. 2013.

[54] R. Guzman, L. G. de Vicuna, A. Camacho, J. Matas, M. Castilla, and J. Miret, "Active damping control for a three phase grid-connected inverter using sliding mode control," in *Proc. 39th Annu. Conf. of the IEEE Industrial Electronics Society, IECON*, 2013, pp. 382–387.

[55] X. Hao, X. Yang, T. Liu, L. Huang, and W. Chen, "A sliding-mode controller with multiresonant sliding surface for single-phase grid-connected VSI with an LCL filter," *IEEE Trans. Power Electron.*, vol. 28, no. 5, pp. 2259–2268, May 2013.

[56] F. Fuchs, J. Dannehl, and F. W. Fuchs, "Discrete sliding mode current control of grid-connected three-phase PWM converters with LCL filter," in *IEEE Int. Symposium on Ind. Electron*., 2010, pp. 779–785.

[57] J. Hu, Z. Q. Zhu, H. Nian, L. Shang, and Y. He, "Sliding mode current control of grid-connected voltage source converter," in *Proc. IEEE Energy Conversion Congress and Exposition Conf., ECCE,* 2010, pp. 912–919.

[58] H. Mao, X. Yang, Z. Chen, and Z. Wang, "A hysteresis current controller for single-phase three-level voltage source inverters," *IEEE Trans. Power Electron.*, vol. 27, no. 7, pp. 3330–3339, Jul. 2012.

[59] M. Mohseni and S. M. Islam, "A New vector-based hysteresis current control scheme for three-phase PWM voltage-source inverters," *IEEE Trans. Power Electron.*, vol. 25, no. 9, pp. 2299–2309, Sep. 2010.

[60] A. Tripathi and P. C. Sen, "Comparative analysis of fixed and sinusoidal band hysteresis current controllers for voltage source inverters," *IEEE Trans. Ind. Electron.*, vol. 39, no. 1, pp. 63–73, Feb. 1992.

[61] D. N. Zmood and D. G. Holmes, "Stationary frame current regulation of PWM inverters with zero steady-state error," *IEEE Trans. Power Electron.*, vol. 18, no. 3, pp. 814–822, May 2003.

[62] M. Liserre, R. Teodorescu, and F. Blaabjerg, "Stability of photovoltaic and wind turbine grid-connected inverters for a large set of grid impedance values," *IEEE Trans. Power Electron.*, vol. 21, no. 1, pp. 263–272, Jan. 2006.

[63] N. Mohan, T. M. Undeland, and W. P. Robbins, *Power electronics: converters, applications, and design*, 2nd ed., New York: Wiley, 1995.

[64] G. F. Franklin, J. D. Powell, and M. L. Workman, *Digital control of dynamic systems, 3rd* ed., Menlo Park, Calif.: Addison-Wesley, 2002.

[65] M. Castilla, J. Miret, A. Camacho, J. Matas, and L. G. de Vicuna, "Reduction of current harmonic distortion in three-phase grid-connected photovoltaic inverters via resonant current control," *IEEE Trans. Ind. Electron.*, vol. 60, no. 4, pp. 1464–1472, Apr. 2013.

[66] X. Zhang, J. W. Spencer, and J. M. Guerrero, "Small-signal modeling of digitally controlled grid-connected inverters With LCL filters," *IEEE Trans. Ind. Electron.*, vol. 60, no. 9, pp. 3752–3765, Sep. 2013.

[67] R. Teodorescu, F. Blaabjerg, M. Liserre, and A. Dell'Aquila, "A stable three-phase LCL-filter based active rectifier without damping," in *Conf. Record 38th IAS Annu. Meeting Ind. Appl. Conf.*, 2003, vol. 3, pp. 1552–1557.

[68] A. Kahrobaeian and Y. A.-R. I. Mohamed, "Robust single-loop direct current control of LCL-filtered converter-based DG units in grid-connected and autonomous microgrid modes," *IEEE Trans. Power Electron.*, vol. 29, no. 10, pp. 5605–5619, Oct. 2014.

[69] J. Dannehl, M. Liserre, and F. W. Fuchs, "Filter-based active damping of voltage source converters With LCL filter," *IEEE Trans. Ind. Electron.*, vol. 58, no. 8, pp. 3623–3633, Aug. 2011.

[70] J. Wang, J. D. Yan, L. Jiang, and J. Zou, "Delay-dependent stability of single-loop controlled grid-connected inverters with LCL filters," *IEEE Trans. Power Electron.*, vol. 31, no. 1, pp. 743–757, Jan. 2016.

[71] J. Wang and J. D. Yan, "Using virtual impedance to analyze the stability of LCL-filtered grid-connected inverters," in *Proc. IEEE Ind. Technology (ICIT) Conf.*, 2015, pp. 1220–1225.

[72] Weimin Wu, Min Huang, Yunjie Sun, Xiongfei Wang, and F. Blaabjerg, "A composite passive damping method of the LLCL-filter based grid-tied inverter," in *Proc. 3rd IEEE International Symposium on Power Electronics for Distributed Generation Systems (PEDG)*, 2012, pp. 759–766.

[73] A. K. Balasubramanian and V. John, "Analysis and design of split-capacitor resistive-inductive passive damping for LCL filters in grid-connected inverters," *IET Power Electron.*, vol. 6, no. 9, pp. 1822–1832, Nov. 2013.

[74] R. Peña-Alzola, M. Liserre, F. Blaabjerg, R. Sebastián, J. Dannehl, and F. W. Fuchs, "Analysis of the passive damping losses in LCL-filter-based grid converters," *IEEE Trans. Power Electron.*, vol. 28, no. 6, pp. 2642–2646, Jun. 2013.

[75] W. Wu, Y. He, T. Tang, and F. Blaabjerg, "A New design method for the passive damped LCL and LLCL filter-based single-phase grid-tied inverter," *IEEE Trans. Ind. Electron.*, vol. 60, no. 10, pp. 4339–4350, Oct. 2013.

[76] R. N. Beres, X. Wang, M. Liserre, F. Blaabjerg, and C. L. Bak, "A review of passive power filters for three-phase grid-connected voltage-source converters," *IEEE J. Emerg. Sel. Top. Power Electron.*, vol. 4, no. 1, pp. 54–69, Mar. 2016.

[77] R. Beres, X. Wang, F. Blaabjerg, C. L. Bak, and M. Liserre, "Comparative evaluation of passive damping topologies for parallel grid-connected converters with LCL filters," in *Proc. Int. Power Electron. Conf. (IPEC-Hiroshima 2014 - ECCE ASIA)*, 2014, pp. 3320–3327.

[78] M. Routimo and H. Tuusa, "LCL type supply filter for active power filter - comparison of an active and a passive method for resonance damping," in *Proc. IEEE Power Electron. Specialists Conf., PESC*, 2007, pp. 2939–2945.

[79] M. H. Hedayati, A. A. B., and V. John, "Common-mode and differential-mode active damping for PWM rectifiers," *IEEE Trans. Power Electron.*, vol. 29, no. 6, pp. 3188–3200, Jun. 2014.

[80] M. Huang, X. Wang, P. C. Loh, and F. Blaabjerg, "Active damping of LLCL-filter resonance based on LC-trap voltage and capacitor current feedback," in *Proc. IEEE Appl. Power Electron. Conf. Expo., APEC*, 2015, pp. 2903–2910.

[81] Wenqiang Zhao and Guozhu Chen, "Comparison of active and passive damping methods for application in high power active power filter with LCL-filter," in *Proc. Sustainable Power Generation and Supply Conf., SUPERGEN '09.*, 2009, pp. 1–6.

[82] T. Tang, S. Xie, and J. Xu, "Evaluations of current control in weak grid case for grid-connected LCL-filtered inverter," *IET Power Electron.*, vol. 6, no. 2, pp. 227–234, Feb. 2013.

[83] S. Cobreces, E. Bueno, F. J. Rodriguez, F. Huerta, and P. Rodriguez, "Influence analysis of the effects of an inductive-resistive weak grid over L and LCL filter current hysteresis controllers," in *Proc. European Power Electron. and App. Conf.*, 2007, pp. 1–10.

[84] Dae-Keun Choi, Duk-Hong Kang, and Kyo-Beum Lee, "A novel gain scheduling method for distributed power generation systems with a LCL-filter by estimating grid impedance," in *Proc. IEEE Int. Symposium on Industrial Electron.*, 2010, pp. 3438–3443.

[85] M. Liserre, F. Blaabjerg, and R. Teodorescu, "Grid impedance detection via excitation of LCL-filter resonance," in *Proc. 40th Annu. meeting Ind. App. (IAS) Conf.*, 2005, vol. 2, pp. 910–916.

[86] M. Liserre, R. Teodorescu, and F. Blaabjerg, "Stability of grid-connected PV inverters with large grid impedance variation," in *Proc. 35th Annu. IEEE Power Electron. Specialists Conf., PESC 04*, 2004, pp. 4773–4779.

[87] C. Liu, X. Zhang, L. Tan, and F. Liu, "A novel control strategy of LCL-VSC based on notch concept," in *Proc. 2nd Int. Symposium on Power Electron. for Distributed Generation Systems*, 2010, pp. 343–346.

[88] X. Lu, K. S. L. Huang, and M. L. F. Blaabjerg, "An active damping method based on biquad digital filter for parallel grid-interfacing inverters with LCL filters," in *Proc. 19th Annu. IEEE Appl. Power Electron. Conf. Expo., APEC*, 2014, pp. 392–397.

[89] S. Zhang, S. Jiang, X. Lu, B. Ge, and F. Z. Peng, "Resonance issues and damping techniques for grid-connected inverters with long transmission cable," *IEEE Trans. Power Electron.*, vol. 29, no. 1, pp. 110–120, Jan. 2014.

[90] M. Liserre, A. Dell'Aquila, and F. Blaabjerg, "Genetic algorithm-based design of the active damping for an LCL-filter three-phase active rectifier," *IEEE Trans. Power Electron.*, vol. 19, no. 1, pp. 76–86, Jan. 2004.

[91] R. Pena-Alzola, M. Liserre, F. Blaabjerg, M. Ordonez, and T. Kerekes, "A self-commissioning notch filter for active damping in a three-phase LCL -filter-based grid-tie converter," *IEEE Trans. Power Electron.*, vol. 29, no. 12, pp. 6754–6761, Dec. 2014.

[92] W. Yao, Y. Yang, X. Zhang, and F. Blaabjerg, "Digital notch filter based active damping for LCL filters," in *Proc. Annu. IEEE Appl. Power Electron. Conf. Expo., APEC*, 2015, pp. 2399–2406.

[93] Y. Liu, W. Wu, Y. He, Z. Lin, F. Blaabjerg, and H. S.-H. Chung, "An efficient and robust hybrid damper for LCL - or LLCL -based grid-tied inverter with strong grid-side harmonic voltage effect rejection," *IEEE Trans. Ind. Electron.*, vol. 63, no. 2, pp. 926–936, Feb. 2016.

[94] P. A. Dahono, Y. R. Bahar, Y. Sato, and T. Kataoka, "Damping of transient oscillations on the output LC filter of PWM inverters by using a virtual resistor," in *Proc. 4th IEEE Int. Conf. on Power Electron. and Drive Systems*, 2001, vol. 1, pp. 403–407.

[95] C. Wessels, J. Dannehl, and F. W. Fuchs, "Active damping of LCL-filter resonance based on virtual resistor for PWM rectifiers - stability analysis with different filter parameters," in *Proc. IEEE Power Electronics Specialists Conf., PESC*, 2008, pp. 3532–3538.

[96] D. Pan, X. Ruan, C. Bao, W. Li, and X. Wang, "Capacitor-current-feedback active damping with reduced computation delay for improving robustness of LCL-type grid-connected inverter," *IEEE Trans. Power Electron.*, vol. 29, no. 7, pp. 3414–3427, Jul. 2014.

[97] X. Wang, F. Blaabjerg, and P. C. Loh, "Virtual RC damping of LCL-filtered voltage source converters with extended selective harmonic compensation," *IEEE Trans. Power Electron.*, vol. 30, no. 9, pp. 4726–4737, Sep. 2015.

[98] X. Li, X. Wu, Y. Geng, X. Yuan, C. Xia, and X. Zhang, "Wide damping region for LCL-type grid-connected inverter with an improved capacitor-current-feedback method," *IEEE Trans. Power Electron.*, vol. 30, no. 9, pp. 5247–5259, Sep. 2015.

[99] D. Pan, X. Ruan, C. Bao, W. Li, and X. Wang, "Optimized controller design for LCL -type grid-connected inverter to achieve high robustness against grid-impedance variation," *IEEE Trans. Ind. Electron.*, vol. 62, no. 3, pp. 1537–1547, Mar. 2015.

[100] Xuehua Wang, Chenlei Bao, Xinbo Ruan, Weiwei Li, and Donghua Pan, "Design considerations of digitally controlled LCL-filtered inverter with capacitor- current-feedback active damping," *IEEE J. Emerg. Sel. Top. Power Electron.*, vol. 2, no. 4, pp. 972–984, Dec. 2014.

[101] C. Bao, X. Ruan, X. Wang, W. Li, D. Pan, and K. Weng, "Design of injected grid current regulator and capacitor-current-feedback active-damping for LCL-type grid-connected inverter," in *Proc. IEEE Energy Conversion Congress and Exposition Conf., ECCE,* 2012, pp. 579–586.

[102] X. Wang, X. Ruan, C. Bao, D. Pan, and L. Xu, "Design of the PI regulator and feedback coefficient of capacitor current for grid-connected inverter with an LCL filter in discrete-time domain," in *Proc. IEEE Energy Conversion Congress and Exposition Conf., ECCE,* 2012, pp. 1657–1662.

[103] M. Wagner, T. Barth, C. Ditmanson, R. Alvarez, and S. Bernet, "Discrete-time optimal active damping of LCL resonance in grid connected converters by proportional capacitor current feedback," in *Proc. IEEE Energy Conversion Congress and Exposition Conf., ECCE,* 2013, pp. 721–727.

[104] H. Xiao, X. Qu, S. Xie, and J. Xu, "Synthesis of active damping for grid-connected inverters with an LCL filter," in *Proc. IEEE Energy Conversion Congress and Exposition Conf., ECCE,* 2012, pp. 550–556.

[105] W. Gullvik, L. Norum, and R. Nilsen, "Active damping of resonance oscillations in LCL-filters based on virtual flux and virtual resistor," in *Proc. European Conf. on Power Electronics and Applications*, 2007, pp. 1–10.

[106] V. Miskovic, V. Blasko, T. M. Jahns, A. H. C. Smith, and C. Romenesko, "Observer-based active damping of LCL resonance in grid-connected voltage source converters," *IEEE Trans. Ind. Appl.*, vol. 50, no. 6, pp. 3977–3985, Nov. 2014.

[107] J. Kukkola and M. Hinkkanen, "Observer-based state-space current control for a three-phase grid-connected converter equipped with an LCL filter," *IEEE Trans. Ind. Appl.*, vol. 50, no. 4, pp. 2700–2709, Jul. 2014.

[108] V. Blasko and V. Kaura, "A novel control to actively damp resonance in input LC filter of a three-phase voltage source converter," *IEEE Trans. Ind. Appl.*, vol. 33, no. 2, pp. 542–550, Apr. 1997.

[109] M. Liserre, A. Dell'Aquila, and F. Blaabjerg, "Stability improvements of an LCL-filter based three-phase active rectifier," in *Proc. 33rd Annu. IEEE Power Electron. Specialists Conf., PESC*, 2002, pp. 1195–1201.

[110] M. Malinowski and S. Bernet, "A simple voltage sensorless active damping scheme for three-phase PWM converters with an LCL filter," *IEEE Trans. Ind. Electron.*, vol. 55, no. 4, pp. 1876–1880, Apr. 2008.

[111] M. Malinowski, W. Szczygiel, M. P. Kazmierkowski, and S. Bernet, "Sensorless operation of active damping methods for three-phase PWM converters," in *Proc. IEEE International Symposium on Ind. Electron. (ISIE)*, 2005, pp. 775–780 vol. 2.

[112] R. Pena-Alzola, M. Liserre, F. Blaabjerg, R. Sebastian, J. Dannehl, and F. W. Fuchs, "Systematic design of the lead-lag network method for active damping in LCL-filter based three phase converters," *IEEE Trans. Ind. Inform.*, vol. 10, no. 1, pp. 43–52, Feb. 2014.

[113] J. He, Y. W. Li, D. Bosnjak, and B. Harris, "Investigation and active damping of multiple resonances in a parallel-inverter-based microgrid," *IEEE Trans. Power Electron.*, vol. 28, no. 1, pp. 234–246, Jan. 2013.

[114] C. Yu *et al.*, "A general active damping method based on capacitor voltage detection for grid-connected inverter," in *Proc. IEEE ECCE Asia Downunder (ECCE Asia)*, 2013, pp. 829–835.

[115] Z. Xin, X. Wang, P. C. Loh, and F. Blaabjerg, "Digital realization of capacitor-voltage feedback active damping for LCL-filtered grid converters," in *Proc. IEEE Energy Conversion Congress and Exposition Conf., ECCE*, 2015, pp. 2690–2697.

[116] Z. Xin, X. Wang, P. C. Loh, and F. Blaabjerg, "SOGI-based capacitor voltage feedback active damping in LCL-filtered grid converters," in *Proc. 6th IEEE International Symposium on Power Electron. for Distributed Generation Systems (PEDG)*, 2015, pp. 1–6.

[117] J. Xu, S. Xie, and T. Tang, "Active damping-based control for grid-connected LCL -filtered inverter with injected grid current feedback only," *IEEE Trans. Ind. Electron.*, vol. 61, no. 9, pp. 4746–4758, Sep. 2014.

[118] C. P. Dick, S. Richter, M. Rosekeit, J. Rolink, and R. W. De Doncker, "Active damping of LCL resonance with minimum sensor effort by means of a digital

infinite impulse response filter," in *Proc. European Conference on Power Electronics and Applications*, 2007, pp. 1–8.

[119] M. Hanif, V. Khadkikar, W. Xiao, and J. L. Kirtley, "Two degrees of freedom active damping technique for LCL filter-based grid connected PV systems," *IEEE Trans. Ind. Electron.*, vol. 61, no. 6, pp. 2795–2803, Jun. 2014.

[120] X. Wang, F. Blaabjerg, and P. C. Loh, "Grid-current-feedback active damping for LCL resonance in grid-connected voltage-source converters," *IEEE Trans. Power Electron.*, vol. 31, no. 1, pp. 213–223, Jan. 2016.